



# **Contact Fatigue: Life Prediction and Palliatives**

by

Brett P. Conner

Submitted to the Department of Materials Science and Engineering  
on 20 August 2002, in partial fulfillment of the  
requirements for the degree of  
Doctor of Philosophy

## **Abstract**

Fretting fatigue is defined as damage resulting from small magnitude (0.5-50 microns) displacement between contacting bodies where at least one of the bodies has an applied bulk stress. The applicability and limits of a fracture mechanics based life prediction is explored. Comparisons are made against highly controlled experiments and less controlled but more realistic experiments using a novel dovetail attachment fixture. Surface engineering approaches are examined from a mechanics perspective. Using a new tool, depth sensing indentation, the mechanical properties of an aluminum bronze coating are determined. Fretting fatigue experiments are performed on specimens coated with aluminum bronze and on specimens treated with low plasticity burnishing. Low plasticity burnishing is a new method of introducing beneficial compressive residual stresses without significant cold work at the surface. A mechanics based approach to the selection of palliatives is addressed.

Thesis Supervisor: Subra Suresh

Title: R. P. Simmons Professor and Head, Department of Materials Science and Engineering

# **Contact Fatigue: Life Prediction and Palliatives**

by

**Brett P. Conner**

B.S., University of Missouri-Columbia (1998)  
S.M., Massachusetts Institute of Technology (2000)

Submitted to the Department of Materials Science and Engineering  
in partial fulfillment of the requirements for the degree of

Doctor of Philosophy

at the

**MASSACHUSETTS INSTITUTE OF TECHNOLOGY**

September 2002

© 2002 Massachusetts Institute of Technology. All rights reserved.

The author hereby grants to Massachusetts Institute of Technology permission to  
reproduce and  
to distribute copies of this thesis document in whole or in part.

Signature of Author .....  
Department of Materials Science and Engineering  
20 August 2002

Certified by .....  
Subra Suresh  
R. P. Simmons Professor and Head, Department of Materials Science and Engineering  
Thesis Supervisor

Accepted by .....  
Harry L. Tuller  
Professor of Ceramics and Electronic Materials  
Chair, Departmental Committee on Graduate Students

# **Contact Fatigue: Life Prediction and Palliatives**

by

Brett P. Conner

Submitted to the Department of Materials Science and Engineering  
on 20 August 2002, in partial fulfillment of the  
requirements for the degree of  
Doctor of Philosophy

## **Abstract**

Fretting fatigue is defined as damage resulting from small magnitude (0.5-50 microns) displacement between contacting bodies where at least one of the bodies has an applied bulk stress. The applicability and limits of a fracture mechanics based life prediction is explored. Comparisons are made against highly controlled experiments and less controlled but more realistic experiments using a novel dovetail attachment fixture. Surface engineering approaches are examined from a mechanics perspective. Using a new tool, depth sensing indentation, the mechanical properties of an aluminum bronze coating are determined. Fretting fatigue experiments are performed on specimens coated with aluminum bronze and on specimens treated with low plasticity burnishing. Low plasticity burnishing is a new method of introducing beneficial compressive residual stresses without significant cold work at the surface. A mechanics based approach to the selection of palliatives is addressed.

Thesis Supervisor: Subra Suresh

Title: R. P. Simmons Professor and Head, Department of Materials Science and Engineering

# Contents

<b>1</b>	<b>Introduction</b>	<b>14</b>
1.1	Background . . . . .	14
1.1.1	Historical perspectives on fretting fatigue . . . . .	15
1.1.2	Recent developments . . . . .	16
1.2	Contact fatigue in aerospace materials . . . . .	18
1.3	Contact Mechanics . . . . .	20
1.3.1	Normal Contact . . . . .	20
1.3.2	Contact in the presence of friction . . . . .	26
1.3.3	Contact in the presence of adhesive forces . . . . .	30
1.3.4	Other geometries . . . . .	32
<b>2</b>	<b>Overview of highly controlled fretting fatigue experiments</b>	<b>37</b>
2.1	Introduction . . . . .	37
2.2	Description of the apparatus . . . . .	37
2.2.1	The relationship between the tangential load and the bulk load . . . . .	38
2.3	Description of experiments . . . . .	38
2.3.1	Material . . . . .	40
2.3.2	Experimental matrix . . . . .	40
<b>3</b>	<b>Development of a dovetail fretting fixture</b>	<b>46</b>
3.1	Experimental results . . . . .	47
3.1.1	Fretting fatigue scar measurement . . . . .	50
3.2	Numerical simulation of fretting fatigue in a dovetail fixture . . . . .	52

3.2.1	Obtaining point loads from the finite element model . . . . .	55
3.2.2	Evolution of the shear traction of a cylindrical geometry during the load- ing cycle. . . . .	59
<b>4</b>	<b>Observations of fretting fatigue micro-damage</b>	<b>60</b>
4.1	Background . . . . .	60
4.2	Section preparation . . . . .	62
4.3	Description of fretting cracks and damage . . . . .	62
4.3.1	Sphere-on-flat geometries . . . . .	62
4.3.2	Dovetail fixture . . . . .	62
4.3.3	Flat on flat . . . . .	63
4.3.4	Shot peened specimens . . . . .	64
4.4	Impact of micromechanisms on life-prediction modeling . . . . .	67
4.5	Friction and its evolution . . . . .	71
4.5.1	A derivation of the spherical contact load history . . . . .	71
4.5.2	A review of the cylindrical contact load history . . . . .	74
4.5.3	Incorporating the effects of adhesion . . . . .	76
4.5.4	Experimental results . . . . .	78
4.6	Summary . . . . .	80
<b>5</b>	<b>Fracture mechanics based life prediction</b>	<b>82</b>
5.1	The need for a length scale . . . . .	82
5.2	The crack analogue . . . . .	83
5.2.1	Crack orientation . . . . .	87
5.2.2	Early crack growth . . . . .	88
5.2.3	Later regimes of fretting fatigue crack growth . . . . .	89
5.3	Crack initiation in the absence of a singularity . . . . .	90
5.4	Validation with experimental data . . . . .	91
5.4.1	Controlled sphere-on-flat experiments . . . . .	92
5.4.2	Dovetail fretting fatigue tests . . . . .	94
5.4.3	Controlled flat-on-flat tests . . . . .	95

5.4.4	Cylindrical fretting fatigue of an aluminum alloy . . . . .	96
5.5	Limitations and assumptions of the model . . . . .	98
<b>6</b>	<b>Palliatives</b>	<b>99</b>
6.1	Introduction to surface engineering . . . . .	99
6.2	Coatings . . . . .	101
6.2.1	Experiments . . . . .	101
6.3	Fracture mechanics modeling and coatings . . . . .	104
6.3.1	Depth sensing indentation of contact fatigue resistant soft-metallic coatings	106
6.4	Low plasticity burnishing: compressive residual stress . . . . .	109
6.4.1	Background . . . . .	109
6.4.2	Experiments . . . . .	110
6.4.3	Residual stress and cold work distributions . . . . .	113
6.4.4	Effect on crack initiation . . . . .	115
6.4.5	Effect on crack propagation . . . . .	115
6.4.6	Summary . . . . .	118
<b>7</b>	<b>Conclusions</b>	<b>119</b>
7.1	Summary of work . . . . .	119
7.1.1	Experiments . . . . .	119
7.1.2	Analysis . . . . .	120
7.2	New directions for contact fatigue research . . . . .	121
7.2.1	Contact fatigue . . . . .	121
7.2.2	Palliatives . . . . .	122

# List of Figures

1-1	a.) Fretting wear involves small cyclic displacements as a result of contact alone.	
	b.) Fretting fatigue is fretting in the presence of a bulk fatigue load. Fatigue cracks can develop and will propagate if the bulk load is sufficiently large. . . . .	15
1-2	$h$ is the amount of overlap if two bodies can freely penetrate. After Hills and Nowell 1994. . . . .	21
1-3	Application of a normal load, $P$ , to a cylindrical contact produces a parabolic pressure distribution, $p(x)$ which goes to zero at $a$ and has a maximum at $x = 0$ .	24
1-4	A top-down view of the contact between spheres (or a sphere and a flat). The geometry of the contact patch is a circle of radius $a$ . It should be noted that application of a load tangent to the contact is typically in the $x$ -direction. . . . .	25
1-5	Application of a normal load, $P$ , to the spherical contact results in a parabolic pressure distribution, $p(r)$ , with a pressure of zero at $\pm a$ and a maximum pressure at $x = 0$ . . . . .	26
1-6	A schematic of the shear traction, $q(r)$ , and the pressure traction, $p(r)$ , for a spherical contact. . . . .	27
1-7	If $Q < fP$ , slip will be confined only to the outer regions of contact, while an adhered region, referred to as the stick zone, will develop at the center of contact.	28
1-8	Normalized pressure and shear tractions shown for a cylinder with $Q/fP=0.8$ . . .	28
1-9	Adhesive energy between the two bodies results in an increase in contact radius from $a$ to $a_{\max}$ . . . . .	30



1-10	The solid line represents the contact pressure including adhesion. The first dashed line shows the bounded pressure without adhesion and the second (on the right) shows square root pressure. . . . .	31
1-11	The normalized pressure distribution for a flat punch of length $2a$ with rounded corners resulting in contact length $2b$ . Various values $a/b$ are shown. . . . .	32
1-12	Normalized shear tractions are shown for values of $a/b$ and $Q/fP$ of 0.8 . . . .	34
1-13	The pressure and shear tractions are shown for two extremes of the flat punch with rounded corners: $a/b=0.9$ and $a/b=0.0$ for $Q/fP=0.8$ . . . . .	35
2-1	A photograph of the MIT fretting fatigue fixture. The extensometer can be clearly seen to the left of the specimen. The width of the bar specimen is 4.74 mm. . . . .	39
2-2	A schematic of the MIT fretting fatigue fixture showing the location of load cells, applied loads and supports. . . . .	39
2-3	The first series of experiments varied the maximum bulk stress applied in each test for several contact conditions. The results are compared with plain fatigue data from Bellows et al. [58]. . . . .	41
2-4	Keeping $Q$ fixed at 17 N, $P$ is varied. The maximum bulk stress is 300 MPa. Notice the effect of increasing the pad radius from 12.7 mm to 25.4 mm. . . . .	42
2-5	The tangential load is varied for each test while $P$ is held at 50 N. Again, a decrease in the pad radius results in a decrease in the fretting fatigue life at a given $Q/P$ . . . . .	43
2-6	A fretting fatigue scar for a specimen after 10,000,000 cycles ( $P=24$ N, $Q=17$ N, pad radius of 25.4 mm and max bulk stress of 300 MPa). A crack developed but did not propagate to failure. . . . .	45
2-7	In the sphere-on-flat experiments, cracks would initiate only on the side closest to the actuator. . . . .	45
3-1	A photograph of the dovetail fixture and specimen. . . . .	47
3-2	A schematic of the dovetail fretting fatigue fixture. . . . .	48
3-3	A large crack developed near the maximum edge of contact in Specimen # T2. . .	49

3-4	A section taken from the scar in the previous figure shows that cracks have developed in the slip regions near both edges of maximum contact length. The largest crack is the same crack visible in the previous figure. . . . .	50
3-5	The global mesh for the dovetail finite element model. Notice that the mesh in both the specimen and the fixture becomes refined closer to the interface. . . .	53
3-6	In the case of the short flat contact geometry, nearly 130 elements are located near the contact region. . . . .	53
3-7	The calculated hysteresis loop over two cycles of loading for several values of the coefficient of friction. . . . .	54
3-8	The strain versus load response measured at the strain gauge compared to the calculated response from the model. . . . .	55
3-9	A schematic of the boundary conditions and loads involved in the dovetail model.	56
3-10	A plot of the pressure for a cylindrical contact of a dovetail specimen loaded at $P=1900$ N. Notice the large scatter in pressure values near the maximum contact pressure. . . . .	58
3-11	The evolution of shear tractions from 5% of maximum load to 100% of maximum load for a dovetail specimen contacted by a cylindrical pad. $f=0.8$ . . . . .	59
4-1	A schematic of the flat-on-flat fixture developed at AFRL. . . . .	61
4-2	Two fretting cracks initiated (location shown by arrows) and linked. . . . .	63
4-3	Debris flows into a crack in the slip region of a dovetail specimen. The contact pad was a short flat with taper. . . . .	64
4-4	A crack from a wear crater grows into an asperity. . . . .	65
4-5	SEM image of surface damage showing delamination and the formation of small notches developing into cracks ( $P=50$ N, $Q=27.5$ N, $N=300,000$ cycles, $\sigma_{axial}=270$ MPa, $R=0.1$ , $r=12.7$ mm). . . . .	65
4-6	A small crack ( $0.5\ \mu\text{m}$ ) growing out of a notch. This is one of the notches shown in the above photo. . . . .	66
4-7	Wear debris fill fretting cracks. . . . .	66
4-8	Small fretting fatigue crack filled with wear debris. . . . .	67

4-9	a.) A small crack has developed near the edge of contact. b.) Oxides developed by wear enter the crack as it is opened by contact and bulk tensile stresses. Either one of two effects occur: c.) the crack jumps ahead of the wedge during compressive loading or d.) crack growth is slowed by closure. . . . .	68
4-10	A schematic of the dependence of the fatigue life and the wear volume loss ( $W$ ) on the fretting displacement slip amplitude. The highlighted region is the region where wear debris most impacts fatigue life. . . . .	70
4-11	The coefficient of friction is initially constant in across the contact patch (shown here to be circular). Over $n$ cycles, the coefficient of friction will increase in the slip region as a result of wear. Therefore, the radius of stick will also increase. . . . .	72
4-12	$\bar{f}$ versus $f_n$ for selected values of $Q/P$ . . . . .	74
4-13	The relationship between $\bar{f}$ and $f_n$ is different for spherical and cylindrical contacts. The dashed lines represent the cylindrical contact. . . . .	75
4-14	A plot of $\bar{f}$ (the vertical axis) and $f_n$ (the horizontal axis) for $w=0, 0.1$ and $1$ . As $w$ increases from zero, so does the value of $\bar{f}$ with respect to $f_n$ . . . . .	79
4-15	Experimentally measuring the coefficient of friction in the slip zone over $n$ cycles. . . . .	80
5-1	Aspects of the rigid punch contact problem in a.) can be equivalent to those of the double edge cracked specimen in b.) . . . . .	84
5-2	The normal traction, $p$ , in the punch problem is square root singular in the asymptotic limit as one approaches the edge of contact. . . . .	85
5-3	For a contact without adhesion, the pressure is bounded and zero at the edge of contact $\pm a$ . However, the presence of adhesion would cause the pressure to become singular at the new edge of contact, $\pm a_{\max}$ , for strongly adhered contacts or at the stick zone boundary, $\pm c$ , for weakly adhered contacts. . . . .	85
5-4	A schematic of a kinked crack. The mechanics of a kinked crack will be used to determine crack orientation and early crack growth of fretting fatigue cracks. . . . .	87
5-5	$\Delta k_1$ is plotted versus number of cycles to failure for experiments where $P$ is varied while $Q$ is held fixed at 17 N and the maximum bulk stress is 300 MPa. . . . .	92
5-6	$\Delta k_1$ is plotted versus number of cycles to failure for experiments where $Q$ is varied while $P$ is 50 N. Again, the maximum bulk stress is 300 MPa. . . . .	93

5-7	A plot comparing the experimental life versus the predicted life using the fracture mechanics methodology. Experiments from several geometries and fixtures are shown. . . . .	95
5-8	Multiple fretting fatigue cracks emerge from the contact surface (at the bottom of the micrograph). The dominant crack is oriented at a 48.7 degree angle to the surface and turns normal to the bulk stress by 17.6 microns. . . . .	96
5-9	$\Delta k_1$ versus number of cycles to failure for cylindrical contact (Al 4%wt Cu) and $R=-1$ . . . . .	97
6-1	A low magnification composite SEM image of the fretting scar of a coated specimen after a crack has developed and propagated. . . . .	102
6-2	a.) A 3-D surface profile showing material removal to a depth of 29 microns in a small section of the slip zone from a coated specimen. b.) An uncoated specimen showing significantly less material removed in the slip region. c.) and d.) show 2-D surface profiles taken in a.) and b.) respectively. . . . .	103
6-3	Transitioning the crack analogue to a coated body with coating thickness $h$ via the complex stress intensity factor $K$ . . . . .	105
6-4	A schematic of a P-h curve. . . . .	106
6-5	A micrograph looking down into a indentation into the coating. Note the small dents and particles on the surface. . . . .	108
6-6	A photograph of an LPB treated specimen in the dovetail fixture. Notice the polished appearance of the specimen regions near the contact pad. This is a result of the contact pressure from the rolling sphere. . . . .	110
6-7	The maximum load for failure at $10^6$ cycles ( $R=0.1$ ) for baseline specimens and LPB treated specimens. . . . .	111
6-8	The number of cycles to failure for an 18.3 kN maximum load ( $R=0.1$ ). Significant improvement for the LPB treated specimen. . . . .	112
6-9	X-ray diffraction measurements of the burnishing induced residual stresses under the fretting fatigue scar and away from. . . . .	113
6-10	X-ray diffraction measurements of the burnishing induced % cold work distribution under the fretting fatigue scar and away from. . . . .	114

6-11 A plot showing the stress intensity factor as a function of crack length for a crack at the edge of contact and normal to the surface. 3 different test conditions are considered corresponding to an untreated specimen at baseline loads, a specimen treated with LPB at baseline loads, and specimen treated with LPB with a 50% increase in maximum load resulting in failure at $10^6$ cycles. . . . .	117
--	-----

# List of Tables

2.1	A list of some of the mechanical properties of the Ti-6Al-4V alloy. TS=tensile strength. TF=true fracture stress. RA=reduction in area at fracture. SR=strain rate . . . . .	40
2.2	Contact radii and pressures for Ti-6Al-4V pads pressed into a flat surface at 50 N.	41
3.1	Experimental results from dovetail fretting tests. Loads in kN; sg=strain gauge; vm=video strain mapping. . . . .	51
3.2	Measurements of fretting fatigue scars . . . . .	51
3.3	Elastic properties of materials used in finite element model of the dovetail. . . . .	52
3.4	Loads as determined via FEM. LPB is low plasticity burnishing and will be described in Chapter 6. . . . .	57
3.5	Loads as determined via FEM compared with the upper bound when $f=0$ . . . . .	58
4.1	Experimental results for Ti-6Al-4V on Ti-6Al-4V spherical contact . . . . .	79
5.1	Conditions for experiments reported by Hutson et al. . . . .	91
5.2	Predictions for stresses in the x-direction for failure at $1e7$ cycles. . . . .	91
5.3	Some mechanical properties of the alloys used in the selected fretting fatigue tests	91
5.4	Stress intensity factors and crack orientation angles for the dovetail experiments.	94
5.5	Fatigue life predictions for conditions used in each of the dovetail experiments. ro=runout . . . . .	94
6.1	Experimental results for fretting fatigue of Al-bronze coated specimens . . . . .	102

6.2	Complex K for the experimental conditions listed above. It is assumed that the Poisson's ratio of the substrate and the coating are equal. n/f means no failure. .	105
6.3	Experimental results for fretting fatigue of LPB treated specimens . . . . .	111
6.4	Stress intensity factors and crack orientation angles for the LPB treated dovetail experiments. . . . .	116
6.5	Fatigue life predictions for conditions used in each of the LPB dovetail experiments. ro=runout . . . . .	116

# Chapter 1

## Introduction

### 1.1 Background

Contact fatigue can be defined as damage resulting from cyclic relative motion between two surfaces. As a result, component service life may be reduced and maintenance costs could increase as inspections, repairs and palliatives may be required. The list of engineering systems affected by contact fatigue is long and stretches across the engineering spectrum including aerospace systems, micromechanical devices, railroad tracks, chain links, ball bearings, and biomedical implants [1, 2, 3, 4].

A particularly damaging form of contact fatigue is fretting fatigue. Fretting wear is defined as cyclical small displacements between two bodies in contact. In fretting fatigue, one or both of the bodies also have an applied cyclical bulk stress. The fretting is then accompanied with fatigue damage and if the cyclic bulk load is sufficiently large, fatigue cracks may propagate to failure.

There are competing demands on the engineer who faces contact fatigue. The design engineer desires guidelines to prevent or minimize contact fatigue. The maintenance engineer wants reliable service life predictions with room for safety, yet predictions that are less conservative result in more economical ownership costs. Before these demands can be met, the materials science and mechanics of contact fatigue must be more fully understood.



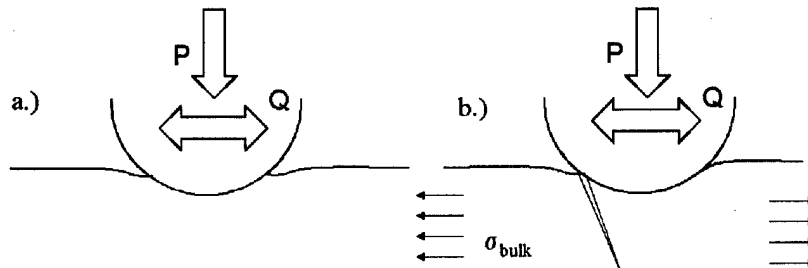


Figure 1-1: a.) Fretting wear involves small cyclic displacements as a result of contact alone. b.) Fretting fatigue is fretting in the presence of a bulk fatigue load. Fatigue cracks can develop and will propagate if the bulk load is sufficiently large.

### 1.1.1 Historical perspectives on fretting fatigue

Much of the effort in contact fatigue research has been focused on fretting fatigue for two primary reasons. First, fretting fatigue is encountered in many engineering systems. Second, all the major variables can be obtained experimentally including a bounded displacement.

One of the earliest articles on fretting fatigue was that of Eden et al. who in 1911 noted that oxides formed in the grips of a tensile fatigue specimen [5]. Early fretting fatigue developments included linking oxide formation to tangential contact loading [6] and discovery that fretting fatigue reduces the fatigue strength [7].

In the 1960's, some of the more common experimental methods were developed. The first was the bridge pad apparatus which gives a constant stress distribution equal to the normal load divided by the contact area. This was soon followed by the development of a fretting fatigue fixture that held a cylindrical pad. The primary advantage of this geometry is that analytical solutions exist for the stresses under a cylindrical pad [8]. These will be discussed in detail later.

The field of contact mechanics provided the necessary tools to determine stresses and displacements under fretting contacts. Hertz solved the boundary value problem to obtain the

contact pressure underneath cylindrical and spherical indenters [9]. Cattaneo [10], and later Mindlin [11], found the tangential tractions underneath spheres in partial-slip conditions; a useful development for the study of fretting fatigue. The tractions underneath a partial-slip cylindrical contact can be found in detail in [12].

The application of fracture mechanics in fretting fatigue was first considered by Endo and Goto [13] then Edwards [14]. Accounting for the stress gradients resulting from contact requires application of a weight function such as in [15]. Another approach is that of Hills and Nowell who suggest the use of a distribution of hypothetical dislocations to model the stress field and boundary conditions of the fretting fatigue crack [16]. One can also use fracture mechanics to determine total life by assuming that all of the life is propagation [17]. In this method, an effective initial flaw size (non-physical) is assumed based on a large body of experimental data.

Beyond stresses and displacements, other damage mechanisms were considered by researchers. The effect of adhesion on fretting fatigue was first approached by Godfrey [18], and later by Bethune and Waterhouse [19]. Since friction can increase temperatures, several researchers considered experimental measurements or theoretical predictions to determine the magnitude of temperature increase as a result of fretting and what, if any, material damage may result [20, 21, 22].

### **1.1.2 Recent developments**

While the study of the effects of contact fatigue can be traced back to the failure analysis of railroad tracks in the late 1800's, remarkable headway has occurred in the last ten to twenty years.

One of the major recent efforts in fretting fatigue centered around the progression of wear damage and its impact on fretting fatigue life. Most of this research was performed by research teams in France. Fretting maps were developed from a large quantity of experiments showing regimes of no slip, partial-slip or stick-slip, mixed slip and gross slip plotted in an analytical space bounded by the applied normal load and the displacement [23]. In general, the fatigue life decreased significantly during partial-slip conditions as opposed to gross-slip conditions. However, many experiments begin with gross-slip that eventually becomes stick-slip after several hundreds or thousands of cycles as a result of wear damage. This evolution of the coefficient

of friction was qualitatively demonstrated through plotting the tangential load/displacement hysteresis loops over the entire life of the experiment. Hills, Nowell and Sackfield analytically determined the evolution of the coefficient of friction for a Hertzian contact [24].

At Oxford, extensive effort was placed into developing an experimental apparatus to measure and control all fretting fatigue variables [25]. Upon obtaining these variables, one could use the experimental results for validation of fretting fatigue models. It was determined that the common bridge pad fretting fatigue apparatus did not permit partial slip conditions since a stick region was not permissible under a flat surface [26]. Simple non-conforming Hertzian contacts and partially conforming contacts such as flat punches with rounded corners permitted experiments with partial slip contact conditions. Such an approach required careful development of fretting fatigue experimental fixtures particularly to quantify the tangential loading and the displacement. Key features included interchangeable pads and specimens, load cells to quantify tangential loads, and extensometers to measure displacements.

Ruiz, also at Oxford, developed a fretting fatigue damage parameter based on work-energy principles [27]. He realized that the work performed in fretting is the area of the local shear times the local displacement (both shear and displacement vary over the interface) or  $\tau\delta$ . This parameter reasonably predicted the location of fretting fatigue cracks in dovetails but not so for other geometries. As a result, Ruiz and Chen empirically added the maximum normal stress,  $\sigma\tau\delta$ , and showed reasonable nucleation location for the sphere-on-flat geometry [28]. Thus, a unique fretting fatigue parameter has been developed but without a fully physical basis.

In the area of contact fatigue modelling, several recent advances should be noted. One was Ciavarella's development of a generalized Cattaneo-Mindlin analytical solution of contact pressure distributions[29]. This enabled researchers and engineers to determine the surface tractions for almost any contact geometry. In particular, the rounded punch contact problem was examined in detail because of its relevance to the dovetail attachment fatigue [30, 31].

Fretting fatigue at lap joints in aging aircraft prompted research into rivet geometries [32]. Temperature gradients were measured experimentally to validate numerical contact modelling, but the temperature increases in aluminum alloys proved to be on the order of 1 K [33]. Eventually, some of this work was folded into research sponsored by the U. S. Air Force on fretting fatigue in gas turbine engines (to be discussed in the next section). This led to numerical

integration of closed-form singular integral contact equations [34]. This methodology rapidly generated solutions for the contact pressure, shear tractions and resultant stresses.

At MIT, a fretting fatigue apparatus was developed that was very similar to the one developed at Oxford [35, 36]. This enabled a wide range of loading conditions and spherical pad radii to be examined using pads and specimens made of Al 7075 [36] and Ti-6Al-4V [37]. The normal load, tangential load, bulk stresses and pad radii are known for each test, so the results are readily available for model validation.

The MIT research group also developed several novel approaches to life prediction. Departing from the stress-at-a-point approaches found in the literature [38, 39], Giannakopoulos, Lindley and Suresh proposed a method where aspects of contact mechanics can be described with fracture mechanics via analogy if appropriate [40]. This method opened new doors to crack nucleation predictions (“go-or-no-go”) and total life prediction. This methodology was extended to strong and weakly adhered contacts [41] as well as nearly-singular flat contacts [42]. Chambon compared experimental results and total life predictions from these models [43] while Kirkpatrick developed a theoretical approach to determining the depth necessary to peen without losing residual stresses as a result of yielding from the contact stresses [44]. Further details of the MIT experimental fixture and experiments is given below. This thesis builds on this foundation laid by these researchers at MIT.

## 1.2 Contact fatigue in aerospace materials

One of the primary motivations for this research is the role of contact fatigue in applications of aerospace materials. The demands placed on an aircraft structure are extensive. Mechanical and thermal loads can be extreme while density must be relatively light to reduce overall structure weight. An aircraft is subject to cyclic loading through wing loading, atmospheric turbulence, and cabin pressurization. The propulsion and hydraulic systems also experience cyclic loading. In the early to mid 1990’s, much research was focused on the problem of contact fatigue in rivet joints of aging aircraft. Common materials used in lap joints are the aviation aluminum alloys (2xxx or 7xxx series alloys) [32, 45]. During the mid 1990’s, the U. S. Air Force became concerned about dovetail joints in gas turbine engines. As a

result of these problems, the U. S. Air Force funded a National Turbine High Cycle Fatigue Program. This program was an effort by government agencies, industry and universities to research the mechanics, life-prediction methods and palliatives for high cycle fatigue including contact fatigue. Estimates by the U. S. Air Force show that one in six of all in-service high cycle fatigue related engine mishaps were the result of fretting and galling [46]. As a result, inspections and regular maintenance procedures are performed in order to prevent catastrophic in-flight failures. An estimated \$20 million is spent annually on these preventative measures [46]. Increased turbine maintenance also results in higher operating costs and lower mission availability. The seriousness of the contact fatigue problem is captured in this statement from a failure investigation.

"While a fighter was taxiing for takeoff, a sudden "bang" was heard, the aero-engine vibrated violently and the rotational velocity declined. The fire warning light came on. The pilot immediately stopped the process of takeoff and quickly left the fighter. Then the fighter caught fire. After field investigation, it was concluded that the accident resulted from the fracture failures of rotor blade and disk in the first stage compressor." [47]

The common material used in the manufacturing of compressor blades and disks is Ti-6Al-4V or a variant of that alloy. Thus, this material will be the primary focus of the experiments in this thesis.

Contact fatigue plagues commercial aviation just as it does military aircraft. In 2001, an Emirates Air 777 was forced to abort takeoff because of a fretting fatigue failure that liberated a fan blade that destroyed the engine. This incident prompted Rolls Royce to examine their contact fatigue palliatives to find one that could offer more protection [48]. Obviously, the concern over safety increases by several orders of magnitude for a commercial aircraft, and there is still the economic cost of excessive maintenance and inspections.

It should be noted that space systems are also affected by contact fatigue [49]. Contact damage (not necessarily fatigue) has effected several prominent orbital missions including a gear failure on Sputnik, the fatal parachute failure of cosmonaut V. M. Kormarov, a docking failure on Salyut/Soyuz-10 mission [50], a stuck antenna on the Galileo space probe, and stick-slip

fatigue on the space shuttle's orbital quick check values for the orbital maneuvering engines [51]. Ground testing revealed potential contact damage problems on the beta gimbal joints for the International Space Station [51]. The space environment produces unique problems such as vacuum and extreme temperature fluctuations for Earth orbiting spacecraft. The absence of an oxygen atmosphere would prevent the formation of oxides from wear thus influencing third body debris effects and the evolution of friction. The issue of space environmental effects will not be addressed in this thesis but should be noted.

### 1.3 Contact Mechanics

Contacting objects can be cyclically loaded both normally and tangentially. If the tangential load,  $Q$ , exceeds the product of the normal load,  $P$ , and the coefficient of friction,  $f$ , sliding will occur over the entire region of contact. If one of the objects can freely rotate about an axis, then friction can cause rolling. Often, if the objects are designed to fit closely together such as in a rivet joint or a dovetail attachment, relative motion will result in very small displacements on the scale of microns. This is called fretting. Damage resulting from fretting in the presence of a cyclic bulk load applied to one or both of the contacting objects is called fretting fatigue. The applied bulk load required to initiate and propagate a crack to failure will often be significantly less than that required for fatigue failure in the absence of fretting.

In cases, where  $Q$  is less than  $fP$ , slip will be confined to the outer edges of the contact region and the central region will entirely stick. This condition is partial slip and contrasts with the gross displacements of global sliding. Fretting fatigue is often partial slip or a mixture of partial slip and gross sliding [23].

#### 1.3.1 Normal Contact

##### Cylindrical bodies

The normal contact of two elastic bodies shall now be addressed. Assuming that both bodies are well supported (i.e. we can neglect rigid body motion), applying a force,  $P$ , normal to the interface will result in elastic deformation resulting in enlargement of the contact region to a half-width or radius,  $a$ . From Hertz, the boundary conditions require that the normal traction

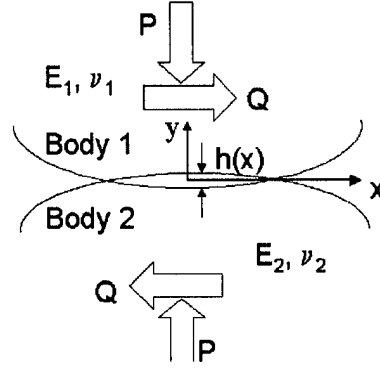


Figure 1-2:  $h$  is the amount of overlap if two bodies can freely penetrate. After Hills and Nowell 1994.

or pressure be zero outside  $a$  and non-zero inside  $a$ . The dimensions of the contact region are determined by the geometry and the elastic material properties of both bodies. Consider two simple cases known as the Hertz problems: spherical and cylindrical contact. Prior to loading, the contact of spheres (also the contact of two orthogonal cylinders) results in a point contact geometry. Likewise, the geometry of contacting cylinders is a line. Hence, spherical contact is often referred to as a point contact and cylindrical contact as a line contact. First, the governing equations of elastic cylindrical contact will be derived, followed by those for spherical contacts.  $h$  is the amount that two bodies would overlap if they could freely interpenetrate each other, Figure 1-2. The relationship between  $h$  and the normal and shear tractions resulting from contact is a singular integral equation.

$$\frac{1}{A} \frac{\partial h}{\partial x} = \frac{1}{\pi} \int \frac{p(\xi) d\xi}{x - \xi} - \beta q(x) \quad (1.1)$$

where  $\xi$  is a coordinate at the interface in the same direction as  $x$ . The elastic properties of both surfaces are contained in constants  $A$  and  $\beta$ [52]

$$A = 2 \left\{ \frac{1 - \nu_1^2}{E_1} + \frac{1 - \nu_2^2}{E_2} \right\} \quad (1.2)$$

$$\beta = \frac{1}{A} \left\{ \frac{(1 - 2\nu_1)(1 + \nu_1)}{E_1} - \frac{(1 - 2\nu_2)(1 + \nu_2)}{E_2} \right\} \quad (1.3)$$

the subscripts 1 and 2 denote the properties of objects 1 and 2.

We will assume elastically similar contact, therefore  $\beta$  equals zero. As a result, there are no shear tractions during normal loading. This would not hold if the materials are dissimilar. As a result of this assumption

$$\frac{1}{A} \frac{\partial h}{\partial x} = \frac{1}{\pi} \int \frac{p(\xi) d\xi}{x - \xi} \quad |x| \leq a \quad (1.4)$$

and with inversion this becomes

$$p(x) = -\frac{w(x)}{A\pi} \int_{-a}^a \frac{h'(\xi) d\xi}{w(\xi)(\xi - x)} + Cw(x) \quad (1.5)$$

where  $w$  is a weight function that depends on the behavior of  $p(x)$  at the end points  $x=a$  or  $x=-a$ . The normal overlap in freely penetrating bodies is

$$h(x) = \Delta - \frac{1}{2}kx^2 \quad (1.6)$$

where  $\Delta$  is the approach of two distant points and  $k$  is the curvature

$$k = \left( \frac{1}{R_1} + \frac{1}{R_2} \right) \quad (1.7)$$

Rather than use the profile  $h(x)$ , instead the slope is considered.

$$\frac{dh}{dx} = -kx \quad (1.8)$$

Since the contact pressure is zero at the edge of contact,  $C = 0$  and thus  $w$  becomes  $\sqrt{a^2 - x^2}$ . Now we can integrate and find an elliptical contact pressure distribution.

$$p(x) = -\frac{\sqrt{a^2 - x^2}}{A\pi} \int_{-a}^a \frac{k\xi d\xi}{\sqrt{a^2 - \xi^2}(\xi - x)} = -\frac{k}{A} \sqrt{a^2 - x^2} \quad (1.9)$$

Recognizing that there is equilibrium between the contact pressure and the applied load leads us to  $a$



$$P = \int_{-a}^a p(\xi) d\xi = \frac{\pi k a^2}{2A} \quad (1.10)$$

This can be rewritten as

$$a = \sqrt{\frac{2PA}{\pi k}} \quad (1.11)$$

Note that  $P$  is in units of load per unit thickness (N/m). Thus, the pressure distribution can be written as

$$p(x) = p_o \sqrt{1 - (x/a)^2} \quad (1.12)$$

There is a maximum at the center of the contact ( $x=0$ ).  $p_o$  is the maximum contact pressure and is defined by

$$p_o = \frac{2P}{\pi a} \quad (1.13)$$

Hertzian contact produces parabolic normal tractions as shown in Figure 1-3.

$$p(x) = p_o \sqrt{1 - \left(\frac{x}{a}\right)^2} \quad (1.14)$$

Upon determination of the surface tractions, the stress and displacements field can be determined. Often these can be obtain via the Muskhelishvili potential[53] . Solutions to the Muskhelishvili potential for cylindrical contacts can be found in [12].

### Spherical contacts

A simple, yet very relevant, three dimensional axisymmetric contact is the spherical contact. The same assumptions of elastic similarity as the cylindrical contact are used here. The assumption that the contact radius is small compared to the contact bodies allows that each bodies can be replaced by a half-space. Thus, the total deformation,  $h(r)$ , can be represented as follows.

$$h(r) = \Delta - \frac{1}{2}kr^2 \quad (1.15)$$

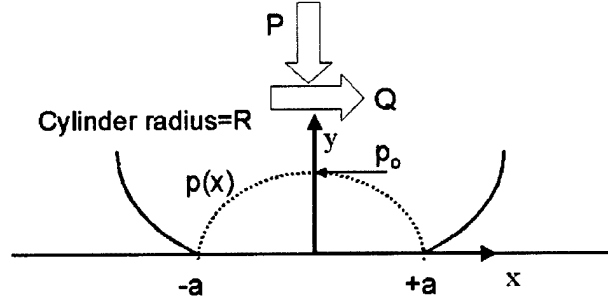


Figure 1-3: Application of a normal load,  $P$ , to a cylindrical contact produces a parabolic pressure distribution,  $p(x)$  which goes to zero at  $a$  and has a maximum at  $x = 0$ .

where  $\Delta$  is the approach of distant points and  $k$  is the curvature. Using a kernel from Collins [54] without detail, this is transformed into

$$h^*(r) = -(\Delta - kr^2) \quad (1.16)$$

The pressure is found by inversion of the following Abel type equation

$$h^*(r) = -A \left\{ \int_r^a \frac{sp(s)ds}{\sqrt{s^2 - r^2}} \right\} \quad (1.17)$$

then integration of the equation to give

$$p(r) = \frac{2}{\pi A} \left\{ \frac{\Delta}{\sqrt{a^2 - r^2}} + k \left[ -\frac{r^2}{\sqrt{a^2 - r^2}} + \sqrt{a^2 - r^2} \right] \right\} \quad (1.18)$$

This is the general solution for the contact pressure. Notice the solution includes a square root singular tensile term. This exists only if adhesion is present. This term will become relevant in discussions later. For now, it is assumed that adhesion is not present and the condition that the pressure drops to zero at the edge of contact gives  $\Delta = ka^2$ .

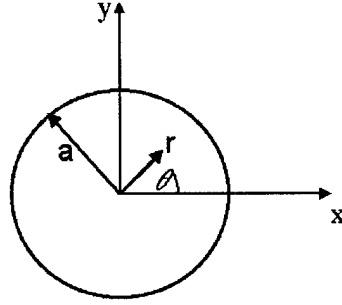


Figure 1-4: A top-down view of the contact between spheres (or a sphere and a flat). The geometry of the contact patch is a circle of radius  $a$ . It should be noted that application of a load tangent to the contact is typically in the  $x$ -direction.

$$p(r) = \frac{4k}{\pi A} \sqrt{a^2 - r^2} \quad (1.19)$$

Requiring equilibrium between the contact pressure and the applied load gives

$$P = \int_0^a p(r) 2\pi r dr \quad (1.20)$$

Note that  $P$  is in units of load only (N). Leading us to the solution of the contact radius (schematically shown in Figure 1-4)

$$a = \sqrt[3]{\frac{3PA}{8k}} \quad (1.21)$$

With the solution for  $a$ , the normal traction can be rewritten as

$$p(x) = p_o \sqrt{1 - \left(\frac{r}{a}\right)^2} \quad (1.22)$$

where the maximum contact pressure is

$$p_o = \frac{3P}{2\pi a^2} \quad (1.23)$$

A schematic of the pressure distribution for a spherical contact is given in 1-5.

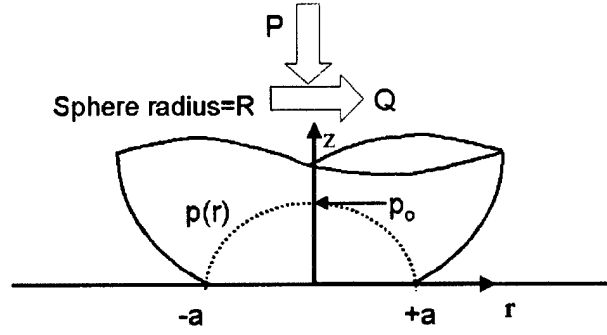


Figure 1-5: Application of a normal load,  $P$ , to the spherical contact results in a parabolic pressure distribution,  $p(r)$ , with a pressure of zero at  $\pm a$  and a maximum pressure at  $x = 0$ .

### 1.3.2 Contact in the presence of friction

#### Sliding contact

Once  $P$  is applied, a tangential force  $Q$  can be introduced and sliding will occur if  $Q \geq fP$ . The shear traction,  $q$ , is a linear function of  $p$  (or a parabolic function of position).

$$q(x) = fp(x) \quad (1.24)$$

$$q(r) = fp(r) \quad (1.25)$$

#### Partial slip contact

If  $Q \leq fP$ , sliding will not be permitted. However, the shear traction will become unbounded at the edge of contact. Since an unbounded traction is not permitted, a counter-traction is added (the Cattaneo-Mindlin solution [10, 11]) and a region of slip will separate the edge of contact from a central region of stick. This phenomenon is shown schematically in Figure 1-7. The radius or half-width of the stick zone is  $c$  and the slip region is bounded by  $a$  and  $c$ . For

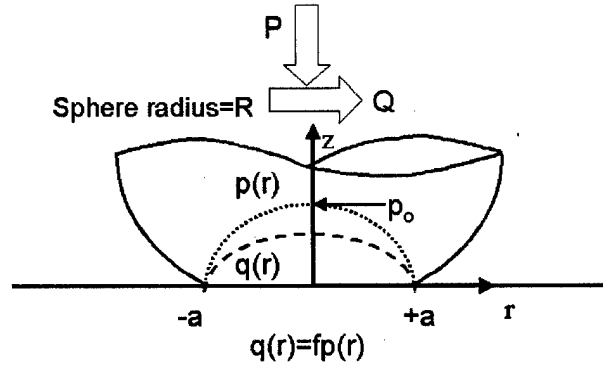


Figure 1-6: A schematic of the shear traction,  $q(r)$ , and the pressure traction,  $p(r)$ , for a spherical contact.

the case of the cylindrical contact, the shear traction  $fp(x)$  must be balanced in the stick region by traction  $q^*(x)$ . The shear tractions become as follows

$$q(x) = fp(x); \quad a \leq x \leq c \quad (1.26)$$

$$q(x) = fp(x) - q^*(x) = fp(x) - \left(\frac{c}{a}\right) f \sqrt{1 - \left(\frac{x}{a}\right)^2}; \quad c \leq x \leq -c \quad (1.27)$$

$$q(x) = fp(x); \quad -c \leq x \leq -a \quad (1.28)$$

For the spherical case, replace  $x$  with  $r$ . Force equilibrium gives us the stick zone dimensions.

$$\frac{c}{a} = \sqrt[3]{1 - \frac{Q}{fP}}; \text{ for spherical contacts} \quad (1.29)$$

$$\frac{c}{a} = \sqrt{1 - \frac{Q}{fP}}; \text{ for cylindrical contacts} \quad (1.30)$$

Figure 1-8 shows the normalized pressure and shear tractions for the case of  $Q/fP=0.8$ . It will be noted here that the conditions for a stick region cannot be satisfied under a flat

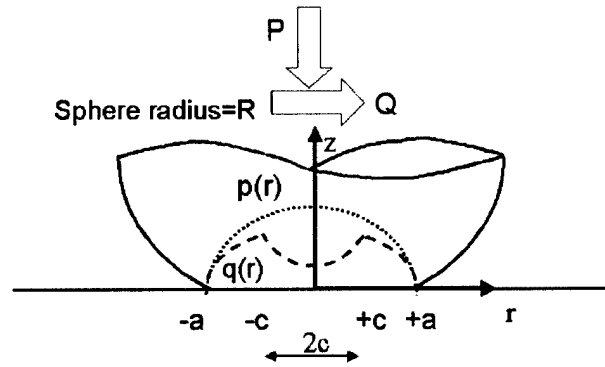


Figure 1-7: If  $Q < fP$ , slip will be confined only to the outer regions of contact, while an adhered region, referred to as the stick zone, will develop at the center of contact.

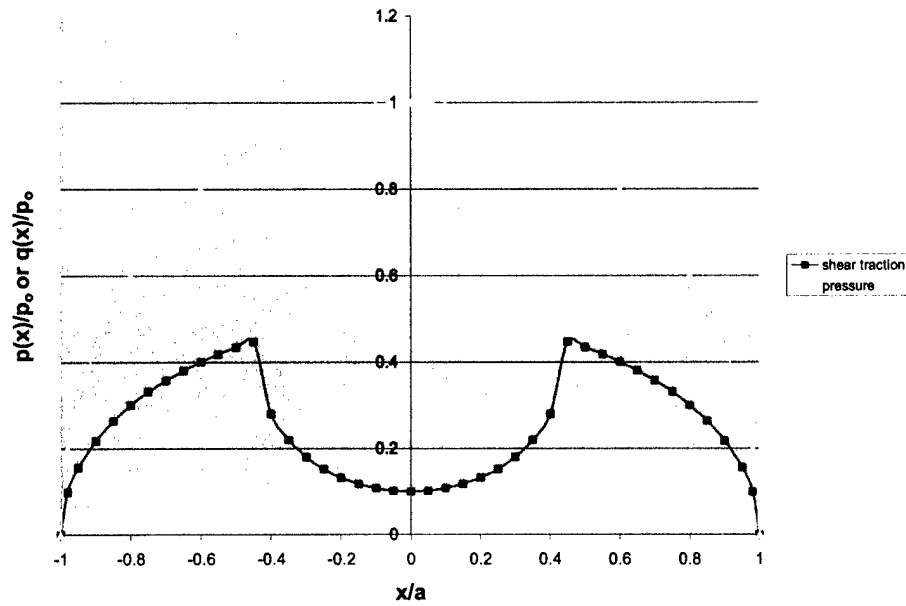


Figure 1-8: Normalized pressure and shear tractions shown for a cylinder with  $Q/fP = 0.8$ .

contact [26]. If a flat punch has a rounded corner, the stick region will extend beyond the flat portion of the punch into the contact region under the rounded corner. In the absence of a rounded corner, partial-slip contact cannot occur and the flat punch will slide.

It should be noted that the coefficient of friction may evolve over the course of a contact fatigue experiment. In the case of partial-slip, wear in the slip region will result in a modified surface. Often the coefficient of friction will increase in this region. The experimentalist would be interested in determining the evolution of the coefficient of friction. It must be recognized that the coefficient of friction is different in each region of the contact. In the stick region, the coefficient of friction,  $\lambda$ , is indeterminate. Here the shear traction is determined by

$$q(x) = \lambda p(x) \quad (1.31)$$

After  $n$  cycles, the coefficient of friction in the slip region can increase from  $f_o$  to  $f_n$ . The coefficient of friction will then vary from the stick zone to the slip zone by the unknown function  $f(x)$ .

$$q(x) = f(x) p(x) \quad (1.32)$$

In the slip region, the coefficient of friction is constant as a function of position (albeit dependent on time).

$$q(x) = f_n p(x) \quad (1.33)$$

If the coefficient of friction does increase after  $n$  cycles, the size of the stick zone may increase resulting in a new stick zone size,  $c_n$ .

$$\frac{c_n}{a} = \sqrt[3]{1 - \frac{Q}{fP}}; \text{ for spherical contacts} \quad (1.34)$$

$$\frac{c_n}{a} = \sqrt{1 - \frac{Q}{fP}}; \text{ for cylindrical contacts} \quad (1.35)$$

The following method can be used to determine the coefficient of friction [55] and this will

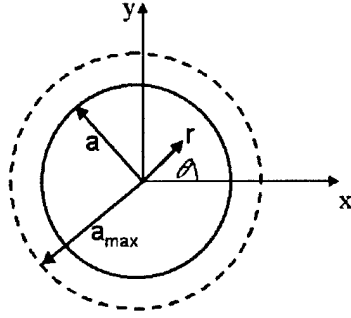


Figure 1-9: Adhesive energy between the two bodies results in an increase in contact radius from  $a$  to  $a_{\max}$ .

be discussed in detail in Section 3.6.

### 1.3.3 Contact in the presence of adhesive forces

Thus far, the elastic contact described has not considered the presence of adhesive forces. Bonding between surfaces can have a significant impact on the size of the contact region and the magnitude of the surface tractions. Two surfaces with surface energies  $\gamma_1$  and  $\gamma_2$  can adhere to form a new interface  $\gamma_{12}$ . The work of adhesion is defined as

$$w = (\gamma_1 + \gamma_2 - \gamma_{12}) \geq 0 \quad (1.36)$$

For most metals,  $w=1$  N/m. In the case of the spherical contact, the new contact radius is

$$a_{\max} = \left[ \frac{3A}{8k} \left( P + \frac{3\pi w}{k} + \sqrt{\frac{6\pi w P}{k} + \left( \frac{3\pi w}{k} \right)^2} \right) \right]^{1/3} \quad (1.37)$$

As a result of the adhesion, the contact radius will increase as shown in Figure 1-9.

For the cylinder contact, the relationship between the adhesive contact radius and the normal load is



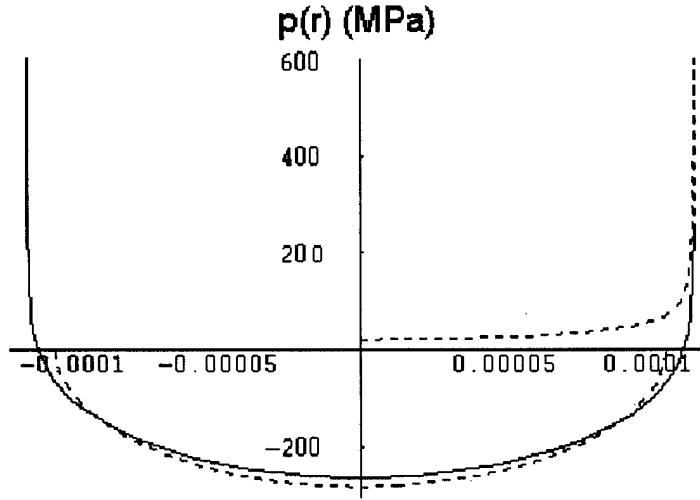


Figure 1-10: The solid line represents the contact pressure including adhesion. The first dashed line shows the bounded pressure without adhesion and the second (on the right) shows square root pressure.

$$P = \frac{\pi}{A} \left\{ \frac{ka_{\max}^2}{2} - 2 \left[ \frac{Aa_{\max}w}{k} \right]^{1/3} \right\} \quad (1.38)$$

If the adhesion is weak enough to allow for slip near the edge of contact, the region of stick for spherical contacts is redefined as

$$\frac{c}{a_{\max}} = \sqrt[3]{1 - \frac{Q}{fP}} \quad (1.39)$$

while for cylindrical contacts, this becomes

$$\frac{c}{a_{\max}} = \sqrt{1 - \frac{Q}{fP}} \quad (1.40)$$

Figure 1-10 gives the pressure distribution for a specific spherical contact both with and without adhesion and compares the adhesion case to a square root singular function. In the asymptotic limit (as  $r \rightarrow a_{\max}$ ), the pressure can be represented by the square root singular function.

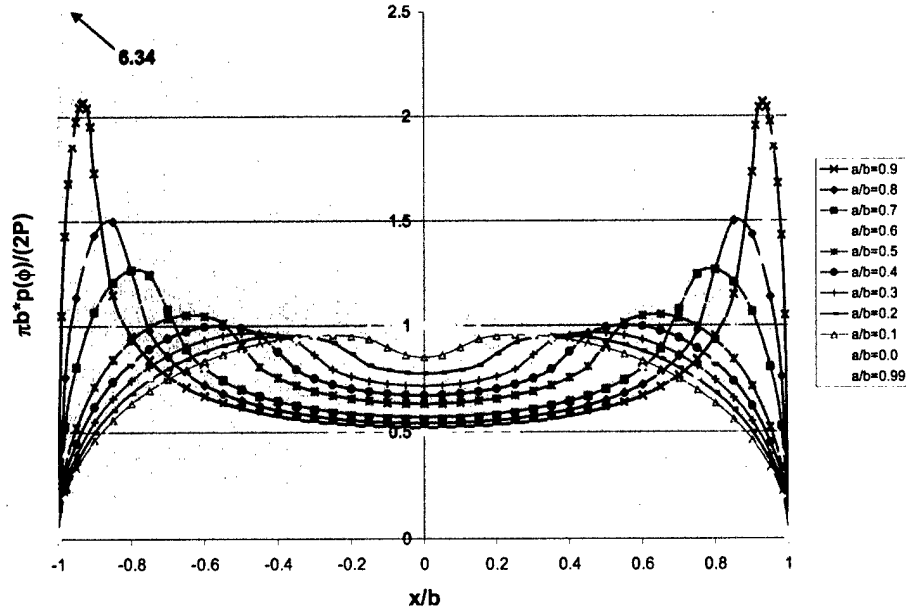


Figure 1-11: The normalized pressure distribution for a flat punch of length  $2a$  with rounded corners resulting in contact length  $2b$ . Various values  $a/b$  are shown.

### 1.3.4 Other geometries

Consider a punch that has a flat region of length  $2a$  with a rounded corner of radius  $D/2$ . Under a normal load, the contact length becomes  $2b$ . The contact pressure of such a punch in contact with a semi-infinite substrate was given by Ciavarella [30]

$$\frac{\pi b}{2P} p(\phi) = \frac{1}{\pi - 2\phi_o - \sin(2\phi_o)} [(\pi - 2\phi_o) \cos \phi + \ln(G(\phi))]; |x| \leq b \quad (1.41)$$

$$G(\phi) = \left| \frac{\sin(\phi + \phi_o)}{\sin(\phi - \phi_o)} \right|^{\sin \phi} \times \left| \tan \frac{\phi + \phi_o}{2} \tan \frac{\phi - \phi_o}{2} \right|^{\sin \phi_o} \quad (1.42)$$

where

$$\sin \phi = x/b; \sin \phi_o = a/b \quad (1.43)$$

The pressure distributions for values of  $a/b$  are shown in Figure 1-11. The relationship between  $b$  and  $P$  is given by

$$\frac{PD}{a^2 E^*} = \frac{\pi - 2\phi_o}{2 \sin^2 \phi_o} - \cot \phi_o \quad (1.44)$$

In conditions of partial slip, a stick zone cannot be sustained within the flat region of the punch [26]. In other words, the magnitude of  $c$  must be greater than that of  $a$ . The relationship between  $Q$  and  $c$  becomes[31]

$$\frac{Q}{fP} = 1 - \left(\frac{c}{b}\right)^2 \frac{\pi - 2\theta_o - \sin(2\theta_o)}{\pi - 2\phi_o - \sin(2\phi_o)} \quad (1.45)$$

where

$$\sin \theta_o = a/c; \sin \phi_o = a/b \quad (1.46)$$

The shear tractions are defined as

$$q(x) = fp(x); \quad b \leq |x| \leq c \quad (1.47)$$

$$q(x) = f[p(x) - q^*(x)]; \quad a \leq |x| \leq c \quad (1.48)$$

where  $q^*(x)$  is the same as  $p(x)$  above replacing  $\phi$  and  $\phi_o$  with  $\theta$  and  $\theta_o$ . The normalized shear tractions for various  $a/b$  are shown in Figure 1-12.

The contact pressure and the shear tractions become singular as  $b$  equals  $a$ , while they approach the Cattaneo-Mindlin solution as  $a$  goes to zero. Figure 1-13 shows compares  $a/b=0.9$  to the Cattaneo-Mindlin solution at  $a/b=0.0$ .

In engineering practice, a plethora of contact geometries exist. For the most complex geometries and loadings, there is often no choice but to use numerical models such as finite element analysis to obtain contact stresses and relative displacements. Finite element meshes must be very dense in the region of contact because of the steep strain and displacement gradients. Optimal meshes, balancing computational efficiency and solution accuracy, must be carefully designed. If sharp corners are present, one may choose to use crack-tip finite elements

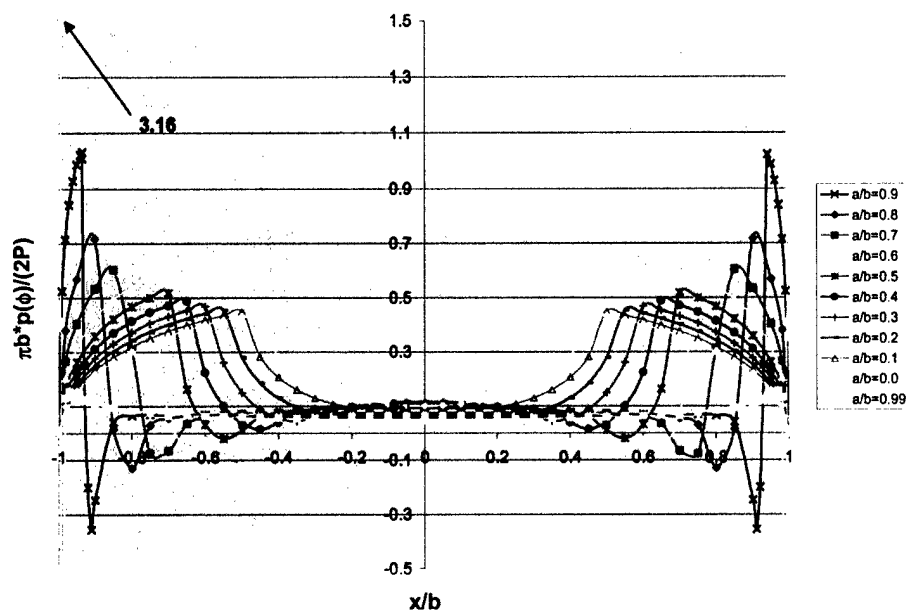


Figure 1-12: Normalized shear tractions are shown for values of  $a/b$  and  $Q/fP$  of 0.8

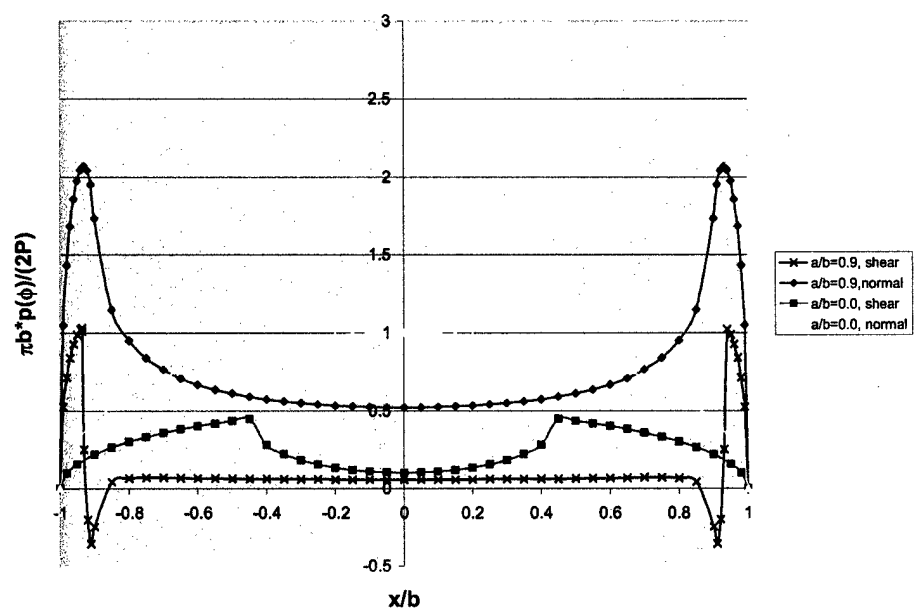


Figure 1-13: The pressure and shear tractions are shown for two extremes of the flat punch with rounded corners:  $a/b=0.9$  and  $a/b=0.0$  for  $Q/fP=0.8$ .

near the corners [16].

## Chapter 2

# Overview of highly controlled fretting fatigue experiments

### 2.1 Introduction

As researchers determined critical variables to fretting fatigue damage, fretting fatigue fixtures had to be designed to control and instrument these variables. These variables would include the normal load,  $P$ ; the tangential load,  $Q$ ; the bulk load,  $F$ ; and the displacement. A fretting fatigue fixture developed at MIT enables the researcher to control and measure every major fretting fatigue variable, see Figure 2-1.

### 2.2 Description of the apparatus

Loads are controlled in several ways. A servo-hydraulic testing machine provides the bulk load to the specimen. The normal load is applied through the compression of springs against a shaft held by linear bearings. Interchangeable contact pads are fixed to the end of the shaft opposite from the springs. The shaft is held in place by a linear bearing. The bearing and a fluid lubricant reduce friction, allow for maximum transfer of force from the springs to the contact pad. A load cell between the spring and the shaft measures the normal force,  $P$ . A frictional force,  $Q$ , that is tangent to the contact interface develops with application of the bulk load,  $F$ . Load cells underneath the mounts containing the linear bearings measure  $Q$ .

An extensometer was developed to measure global displacement. The extensometer is attached behind one of the fretting pads. It has two sharp prongs. One is affixed to the shaft directly behind the pad. The other is glued to the specimen surface at nearly 25 mm away from the center of contact. A schematic of the fixture, the extensometer and the load cells is shown in Figure 2-2.

The signals from each load cells are sent to a data card on a nearly PC. The voltages are converted into loads or displacements by a LabView program. The LabView program displays the inputs from the load cells in real time and records data at predetermined intervals.

### 2.2.1 The relationship between the tangential load and the bulk load

The bearing mount rests upon a stiff plate supported by flexible sheets at each end. Moveable blocks attach the sheet to the rigid supporting structure affixed to the servo-hydraulic machine. The location of the blocks determine the amount of compliance in the tangential load train,  $C_q$ . The compliance of the bulk load train,  $C_f$ , can be changed by inserting one end of the specimen into either a stiff or compliant fixture. The tangential load is related to the application of the bulk load by the following relationship

$$Q = - \left( \frac{C_f}{C_q} \right) F \quad (2.1)$$

This relationship serves as a guide for experiment setup (e.g. one must apply a specific  $F$  to produce a  $Q$ ) and must be determined experimentally. It should be noted that the tangential and bulk loads are in-phase.

## 2.3 Description of experiments

The specimens are bar specimens with a square cross sectional area. The pads are spherical and screw into the rods. Tests can be run up to a pre-determined number of cycles or to failure. Upon failure, tension on the specimen would result in a rapid increase in displacement of the actuator. If the pre-programmed displacement limits are exceeded, the test will stop. Small variations in the loading waveform require that the displacement limits be set on the order of 0.5 mm. As a result, the contact region is often scratched and damaged upon failure,



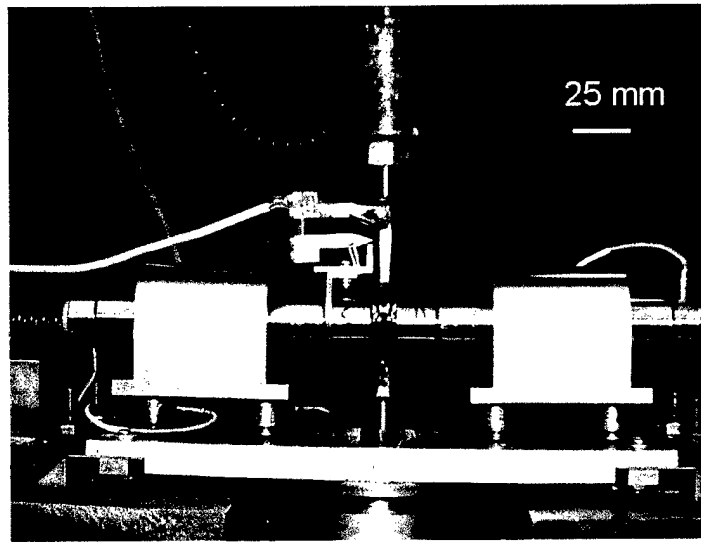


Figure 2-1: A photograph of the MIT fretting fatigue fixture. The extensometer can be clearly seen to the left of the specimen. The width of the bar specimen is 4.74 mm.

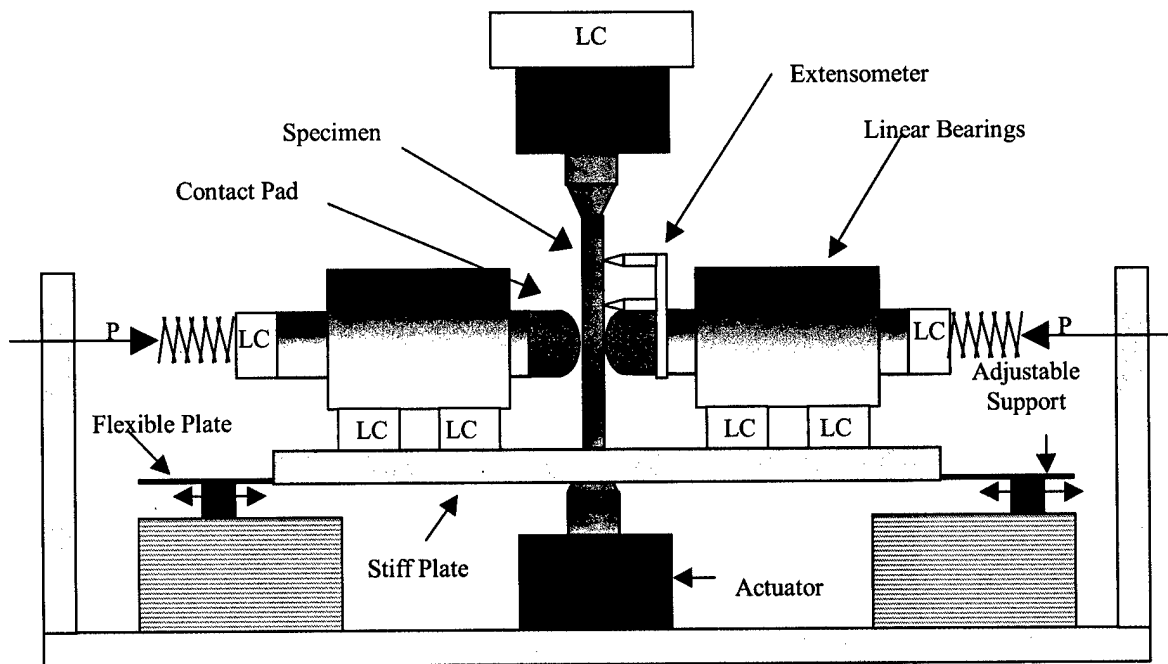


Figure 2-2: A schematic of the MIT fretting fatigue fixture showing the location of load cells, applied loads and supports.

<b>E (GPa)</b>	<b><math>\nu</math></b>	<b><math>\sigma_y</math> (MPa)</b>	<b><math>\sigma_{TS}</math> (MPa)</b>	<b><math>\sigma_{TF}</math> (MPa)</b>	<b>Tens el. (%)</b>	<b>RA (%)</b>	<b>SR (s<sup>-1</sup>)</b>
116	0.3	930	965	1310	19	45	$8 \times 10^{-4}$

Table 2.1: A list of some of the mechanical properties of the Ti-6Al-4V alloy. TS=tensile strength. TF=true fracture stress. RA=reduction in area at fracture. SR=strain rate

so information is limited. Interrupting tests can determine the dimensions of a fretting scar and location of cracks (if they have initiated) compared to the contact radius and slip region.

### 2.3.1 Material

Ti-6Al-4V was the material selected for the controlled fretting fatigue experiments as well as the dovetail fretting fatigue experiments described in the next chapter [37, 56]. Most of the tests were performed on two heat treatments: mill annealed (MA) and solution treated over-aged (STOA). The MA and STOA materials had very similar fretting fatigue behavior and mechanical properties. Some of the mechanical properties of the STOA material are shown in Table 2.1 [57]. Fatigue behavior at various R can be found in [58].

### 2.3.2 Experimental matrix

A matrix of experiments was established to consider the effect of changing individual loads while maintaining all others constant. The load ratio (defined as  $R = L_{\min}/L_{\max}$ ) was -1 in all of the fretting fatigue experiments performed with this apparatus. The first category of experiments involved changing the maximum bulk load while keeping contact loads constant. This is very similar to fretting fatigue tests found in the early literature and demonstrate the effect of fretting fatigue on the fatigue strength. The second set of experiments involved changing the normal load for each test while keeping  $Q$  constant at 17 N and the maximum bulk load constant at 300 MPa. By increasing the normal, the contact area and the contact pressure also increase. Finally, the tangential load was modified in each test as the  $P$  constant at 50 N and the maximum bulk load constant at 300 MPa. As  $Q$  is increased, the size of the slip region increases until it covers the entire contact surface and global sliding occurs. Below a certain  $Q$ , the impact of fretting fatigue on fatigue life is minimized, but  $Q$  greater than  $fP$  results in sliding. For each category of tests, one other variable was considered: changing the pad radius from 12.7 mm to 25.4 mm. Table 2.2 shows the effect of changing pad radius on

Pad radius (mm)	Load (N)	a (μm)	p <sub>o</sub> (MPa)	w (N/m)	a <sub>max</sub> (μm)
12.7	50	194	637	1	237
25.4	50	244	401	1	298

Table 2.2: Contact radii and pressures for Ti-6Al-4V pads pressed into a flat surface at 50 N.

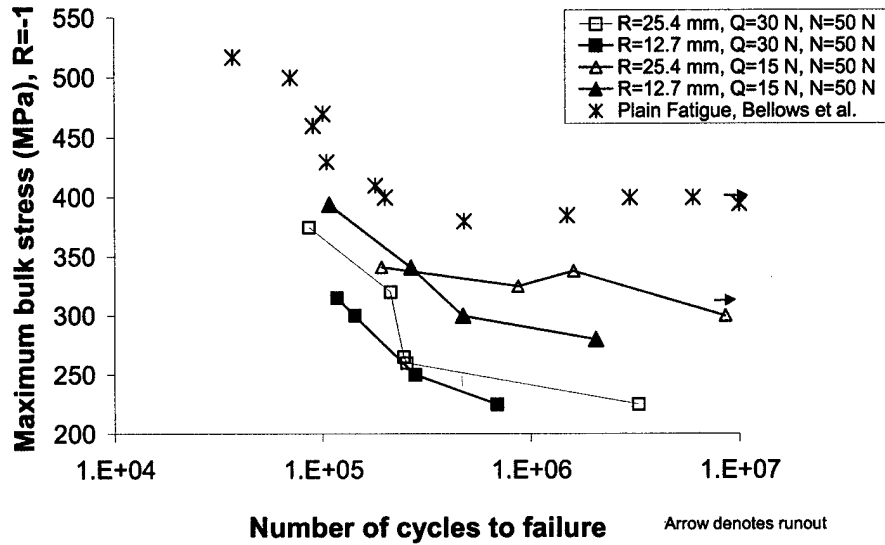


Figure 2-3: The first series of experiments varied the maximum bulk stress applied in each test for several contact conditions. The results are compared with plain fatigue data from Bellows et al. [58].

contact radius and pressure.

Experimental results are plotted in Figures 2-3 to 2-5. The following statements could be made:

1.) Compared with plain fatigue, fretting fatigue reduces the maximum bulk stress required for failure at a given life. This is known as the "knockdown" effect [59] and a knockdown factor can be computed:

$$\sigma_{f,ff} = kf \times \sigma_{f,pf} \quad (2.2)$$

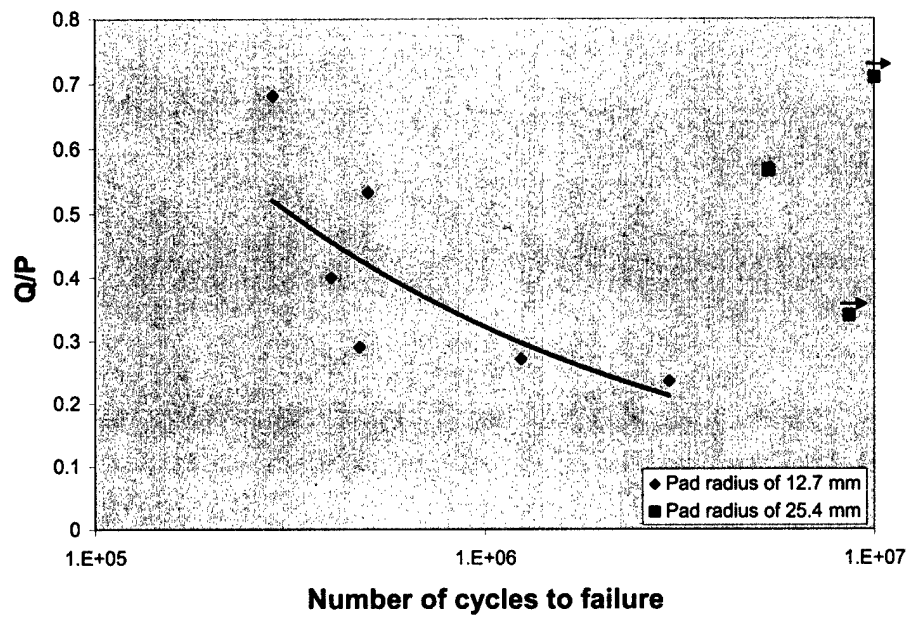


Figure 2-4: Keeping  $Q$  fixed at 17 N,  $P$  is varied. The maximum bulk stress is 300 MPa. Notice the effect of increasing the pad radius from 12.7 mm to 25.4 mm.

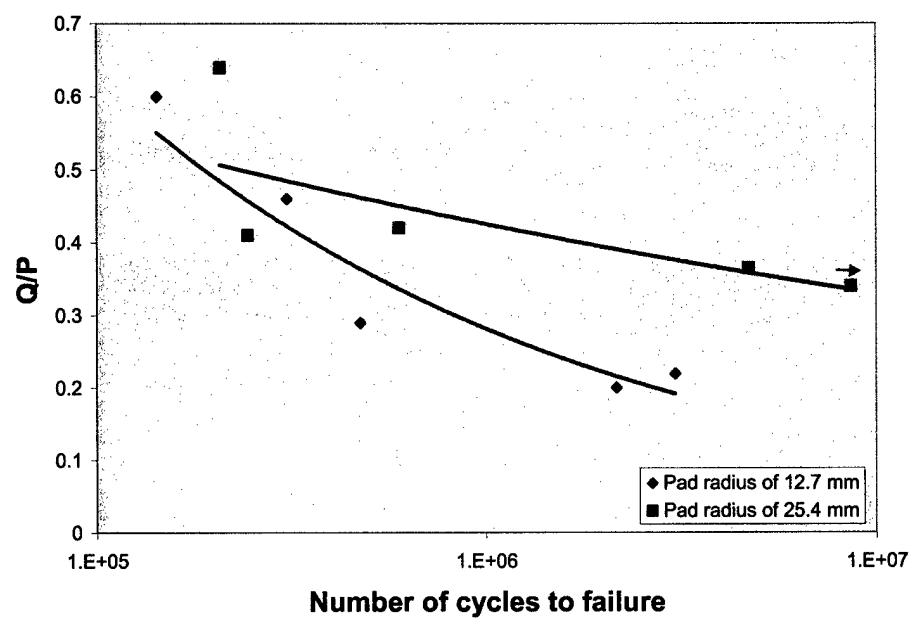


Figure 2-5: The tangential load is varied for each test while  $P$  is held at 50 N. Again, a decrease in the pad radius results in a decrease in the fretting fatigue life at a given  $Q/P$ .

$$kf = \frac{\sigma_{f,ff}}{\sigma_{f,pf}} \quad (2.3)$$

The controlled fretting fatigue experiments shown in Figure 2-3 demonstrates that  $kf$  is reduced when  $Q$  is increased and  $P$  is held constant for a given pad radius.  $kf$  is also reduced when the pad radius is reduced and contact loads remain constant. It should be noted that fretting fatigue life is also reduced when the maximum bulk stress is increased and all other conditions are held constant.

2.) If the normal load is held constant, the fretting fatigue life decreases as  $Q$  is increased. The fretting fatigue life will decrease even further if the pad radius is reduced.

3.) If the tangential load is held constant, increasing  $P$  will increase fretting fatigue life. However, reduction in the pad radius will still decrease fretting fatigue life.

### Scar description and crack initiation location

Wear is produced as a result of slip in the region between the stick zone and the edge of contact. Oxides are produced as fresh material is exposed. For a Ti-6Al-4V on Ti-6Al-4V contact, this oxide is dark and produces a ring about the stick zone called the fretting scar, shown in Figure 2-6.

When cracks did initiate, they did so only at the region near the edge of contact closest to the actuator ( $x = -a, y = 0$ ). This is because the bulk stress is tensile and the contact stresses are tensile at the same time, see Figure 2-7. "Near" the edge of contact is defined as at the edge of contact, in the slip zone, or just outside of the edge of contact. The crack in 2-6 is just outside of the contact zone.

Further analysis of these results will be presented in Chapter 5 when a fracture mechanics based life prediction method is applied.

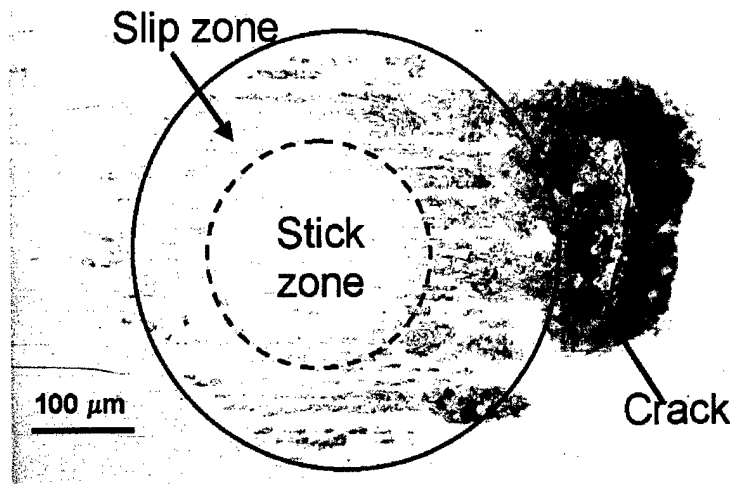


Figure 2-6: A fretting fatigue scar for a specimen after 10,000,000 cycles ( $P=24$  N,  $Q=17$  N, pad radius of 25.4 mm and max bulk stress of 300 MPa). A crack developed but did not propagate to failure.

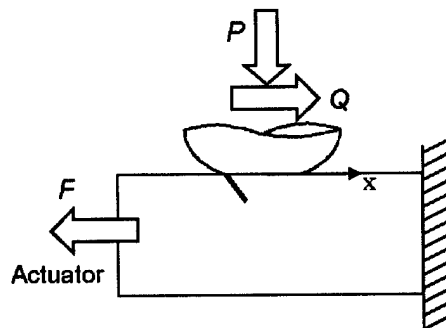


Figure 2-7: In the sphere-on-flat experiments, cracks would initiate only on the side closest to the actuator.

## Chapter 3

# Development of a dovetail fretting fixture

A typical fretting fatigue apparatus applies a constant normal load through springs or bolts. Fretting is possible when both the normal and tangential loads are cyclic. There are two methods to perform this in an experimental fixture. The first is to use the typical fretting fatigue fixture but add an actuator in the contact load train to apply the cyclic normal load. The second is to develop a dovetail fixture. Both types of fretting fixtures have been developed.

Ruiz developed a dovetail fretting fatigue fixture and validated his fretting fatigue parameter with experiments [27, 28, 60]. Two or six dovetail shaped specimens are held in dovetail slots on opposite sides of a sheet. One actuator pulls on the dovetails while another places the sheet in tension. This simulates the inertial loading in a gas turbine engine. Recently, the Oxford group added the capability of a bending moment on the dovetail specimen to simulate blade bending as a result of airflow. The contact between the blade and the sheet is fully conformal on the Ruiz fixture unlike basic contact geometries often found in the literature. The advantage of the Ruiz fixture is that it is very similar to the real blade-disk dovetail joints in gas turbine engines.

To bridge the gap between real contact geometries and more fundamental geometries, a new dovetail fixture was developed at the U. S. Air Force Research Laboratory (AFRL), see Figures 3-1 and 3-2. Rather than use a fully conformal contact geometry as in the Ruiz fixture, the



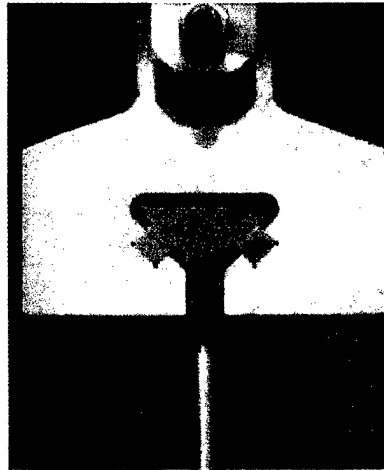


Figure 3-1: A photograph of the dovetail fixture and specimen.

AFRL fixture holds removable contact pads that can be made of any geometry or material. The fixture itself is made of 4140 steel with a Young's modulus of 205 GPa and Poisson's ratio of 0.27. It is held by a bolt at the top. The specimens and pads are placed into the fixture from the side. The specimen is loaded in tension only since compression would cause the specimen to impact the dovetail slot. The specimen is gripped by friction either by collet grips or friction grips and loaded by a hydraulic actuator.

Early finite element modeling showed a region of compressive strain of large magnitude on the face of the fixture located across from the high stress concentration of the dovetail slot, see Figure 3-2. A strain gauge was placed at this location to validate finite element modeling. This is discussed further below.

### 3.1 Experimental results

All experiments used Ti-6Al-4V specimens and pads. Three contact geometries were chosen. The first is a 1.016 mm flat pad with an  $11^\circ$  taper and a blend radius of approximately 1 mm. Next is a 6.35 mm flat pad with rounded corners of radius 3.175 mm. Finally, a cylindrical pad was chosen to provide a Hertzian pressure distribution. It has a radius of 50.8mm. These geometries will be referred to as the "short flat", "long flat" and "cylindrical" pads.

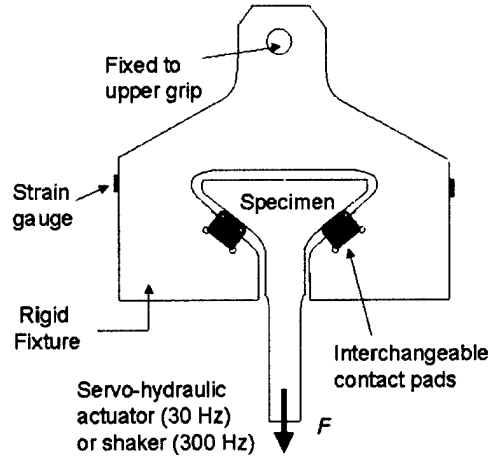


Figure 3-2: A schematic of the dovetail fretting fatigue fixture.

The specimens were tested with a step testing methodology. This method was first derived to develop rapidly a high cycle fatigue ( $10^7$  cycles) Haigh diagram experimentally [61]. It was later validated for fretting fatigue testing [62]. The method is as follows. A load is applied to the specimen at a given load ratio but at a maximum load below that which is expected to cause failure. If failure does not occur after a specified number of cycles,  $N_o$ , the maximum load is increased by a predetermined step increment, but the same load ratio is maintained. The load is stepped up until failure occurs at a given step,  $n$ . The load at failure,  $F_f$ , and the number of cycles to failure at step  $n$ ,  $N_{f,n}$  is recorded. Since a predetermined step increment was used at each step, the load at the step prior to failure,  $F_{pr}$ , is also known. The load required to cause failure at  $N_o$  cycles,  $F_i$ , can now be determined using the following equation:

$$F_i = F_{pr} + \frac{N_{f,n}}{N_o} (F_f - F_{pr}) \quad (3.1)$$

In all of the tests that were designed to lead to failure,  $N_o$  was  $10^6$  cycles. A summary of all of the dovetail fretting fatigue tests is given in Table 3.1. The first series of tests were performed at a frequency of 30 Hz and load ratio of 0.1. All three of the pad geometries were used. It was demonstrated that the long flat pad could sustain the largest maximum load, an

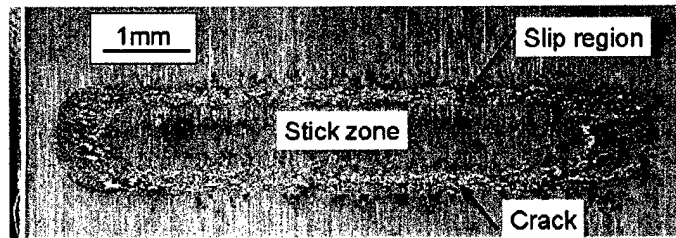


Figure 3-3: A large crack developed near the maximum edge of contact in Specimen # T2.

average of 20.1 kN, to failure after  $10^6$  cycles. This geometry was followed by the cylindrical pad with an average maximum load of 19 kN while the short flat geometry could only sustain a mean maximum load of 18.3 kN. When the load ratio was increased to 0.5, the short flat pad sustained a maximum load of 21 kN.

The dominant crack (i.e. the one that will propagate to failure) is located near the maximum edge of contact on the side of the specimen closest to the actuator. This is shown in the SEM image of the fretting scar in Figure 3-3. A section of that scar reveals that cracks initiated in the slip regions near both sides of the maximum contact length, see Figure 3-4. The dominant crack will always be near the edge closest to the actuator since the maximum bulk stress and the maximum contact stresses occur during the same portion of the loading cycle.

Using the mean maximum loads above, strain gauge measurements were made during the fretting fatigue experiments. Measurements were taken as early as 3 cycles after the test start and as late as 100,000 cycles. The test frequency was reduced since the data acquisition software could not take data at frequencies faster than 10 Hz.

A CCD camera was focused on the near contact region. Using a software algorithm developed at AFRL, displacements near the region of contact were measured [63]. During filming, the test frequency was dropped to 0.001 Hz. To film at higher frequencies would require a synchronized strobe light. The CCD images recorded gross relative contact displacements. For the short flat geometry with a maximum load of 18.3 kN at  $R=0.1$ , the global relative displacement during the second cycle of loading was 18 microns. In the case of the cylindrical

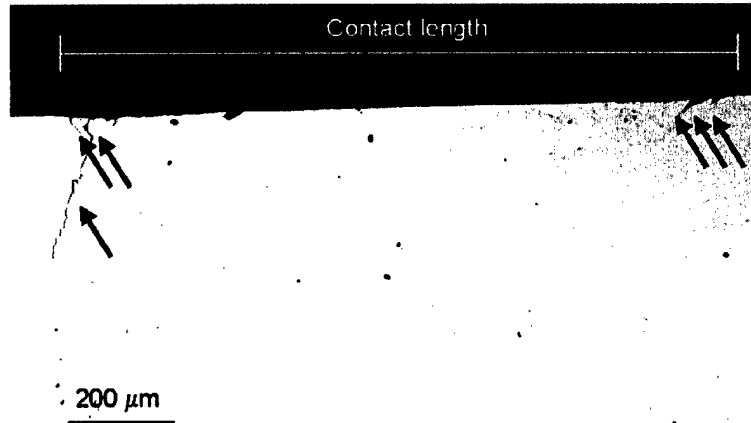


Figure 3-4: A section taken from the scar in the previous figure shows that cracks have developed in the slip regions near both edges of maximum contact length. The largest crack is the same crack visible in the previous figure.

with a maximum load of 19.0 kN at  $R=0.1$ , the global displacement during the second cycle of loading was 23 microns.

### 3.1.1 Fretting fatigue scar measurement

Several of the fretting fatigue scars were measured from micrographs taken after fretting fatigue tests. The measurements of the contact length,  $2a$  or  $2b$ , and the length of the stick zone,  $2c$ , (recall definitions of  $a$ ,  $b$ , and  $c$  from Chapter 1) are listed in Table 3.2. The presence of stick zones underneath the flat portion of the contact is in direct disagreement with theory from [26]. There are two possible reasons for the presence of the stick zones. The first is that corners may become rounded as a result of wear during the fretting fatigue test. The second is that the flat region of the contact pad may not truly be flat but cylindrical with a very large radius of curvature as a result of machining and tumbling.

Specimen #	Pad	R	f (Hz)	$F_f$	$F_{pr}$	$F_i$	n	$N_{f,n}$	Result
T2	short flat	0.1	30	18	16	16.7	5	351,094	failure
01-590	short flat	0.1	30	19	18.5	18.6	3	239,291	failure
01-595	short flat	0.1	30	18.5	18	18.5	2	926,097	failure
01-593	short flat	0.1	30	18	n/a	18	0	892,301	failure
01-479	short flat	0.1	30	18.3	n/a	18.3	0	1,400,000	failure
01-587	short flat	0.5	30	21	20.5	20.9	5	842,712	failure
01-474	short flat	0.5	30	22	21.5	21.9	5	710,452	failure
01-598	long flat	0.1	30	20.5	20	20.1	6	213,988	failure
01-599	long flat	0.1	30	20	19.5	19.5	3	14,575	failure
01-601	long flat	0.1	30	21	20.5	20.6	5	227,441	failure
01-478	cylindrical	0.1	30	20	18	19.5	3	770,828	failure
01-596	cylindrical	0.1	30	19.5	19	19.4	4	888,192	failure
01-597	cylindrical	0.1	30	19	18.5	18.7	2	305,585	failure
01-594	cylindrical	0.1	30	19	18.5	18.8	2	557,008	failure
01-465	short flat	0.1	10	18.3	n/a	n/a	0	33,324	interrupted, sg
01-466	long flat	0.1	10	20.1	n/a	n/a	0	100,000	interrupted, sg
01-467	cylindrical	0.1	10	19	n/a	n/a	0	100,000	interrupted, sg
01-468	short flat	0.1	10	20.1	n/a	n/a	0	100,000	interrupted, sg
01-473	cylindrical	0.1	30/0.001	19	n/a	n/a	0	500	interrupted, vm
01-472	short flat	0.1	30/0.001	18.3	n/a	n/a	0	500	interrupted, vm
01-477	short flat	0.5	30/0.001	18.3	n/a	n/a	0	500	interrupted, vm

Table 3.1: Experimental results from dovetail fretting tests. Loads in kN; sg=strain gauge; vm=video strain mapping.

Specimen	Geometry	Flat length (mm)	2a or 2b (mm)	2c (mm)
T2	short flat	1.016	1.21	0.73
01-590	short flat	1.016	1.22	0.69
01-479	short flat	1.016	1.36	0.96
01-594	cylindrical	0	2.36	1.58
01-598	long flat	6.35	4.64	2.32

Table 3.2: Measurements of fretting fatigue scars

Head	E (GPa)	$\nu$
Ti-6Al-4V	116	0.3
4140 Steel	125	0.3

Table 3.3: Elastic properties of materials used in finite element model of the dovetail.

### 3.2 Numerical simulation of fretting fatigue in a dovetail fixture

A 2-D global finite element model of the dovetail fretting apparatus was developed. Using symmetry boundary conditions at the fixture centerline, only the right side of the fixture is modeled. The mesh of the fixture itself is coarse compared to the mesh in the contact region. Convergence plots were used to determine the necessary element size to obtain accuracy of the vertical elastic strain in the region of the strain gauge.

The contact pads were integrated into the fixture (rather than placed in slots) so the model would be well supported. However, the contact pads were partitioned apart from the remainder of the fixture, so that the mechanical properties of the Ti-6Al-4V could be applied to the pads while the mechanical properties of 4140 steel were applied to the fixture, see Table 3.3.

The fixture was rigidly supported at the bolt hole and was found to produce the equivalent strains as placing a fixed, frictionless rigid cylinder into the bolt hole. A pressure was applied to the base of the specimen equivalent to the applied load divided by half the specimen cross-sectional area (the factor of one-half due to symmetry).

4 node plane strain elements (ABAQUS CPE4R) were chosen. The deformation was taken to be fully elastic. The global mesh is shown in Figure 3-5. Near the contact, the length of an element side was approximately 8 microns. For the loads in the cylinder dovetail experiment, there are nearly 270 elements in the contact region. For the short flat experiment, there are nearly 130 elements in the contact region as shown in Figure 3-6. Smaller elements would have been computationally too costly for this scale of model. The surface of the pad and the opposing specimen surface were chosen to be a contact pair.

A Lagrangian multiplier method was selected to enforce stick-slip constraints at the surface. The Lagrangian method prevents relative motion between two surfaces until the shear traction exceeds a critical value [64]. This adds more degrees of freedom to the model; therefore, it is more computationally expensive than say a penalty friction method which allows sticking nodes

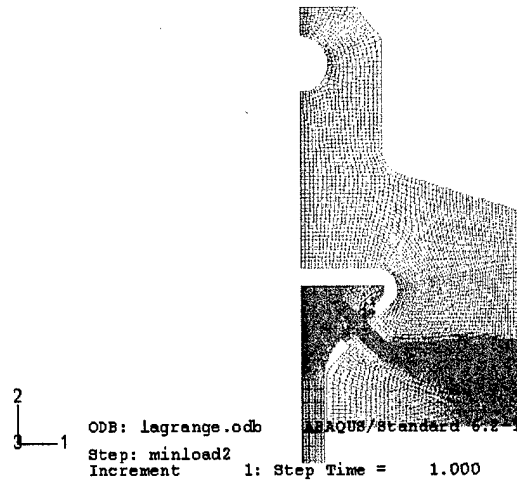


Figure 3-5: The global mesh for the dovetail finite element model. Notice that the mesh in both the specimen and the fixture becomes refined closer to the interface.

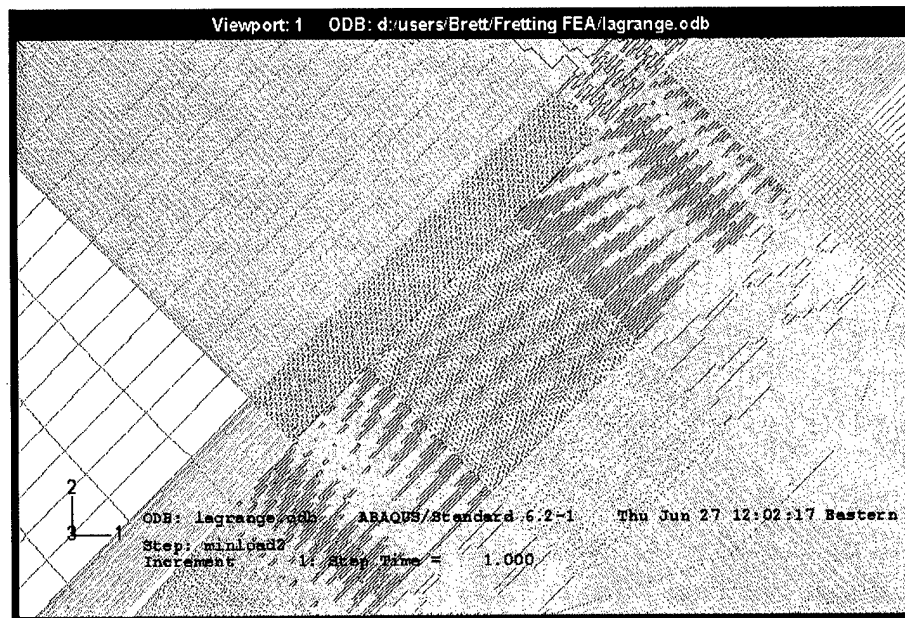


Figure 3-6: In the case of the short flat contact geometry, nearly 130 elements are located near the contact region.

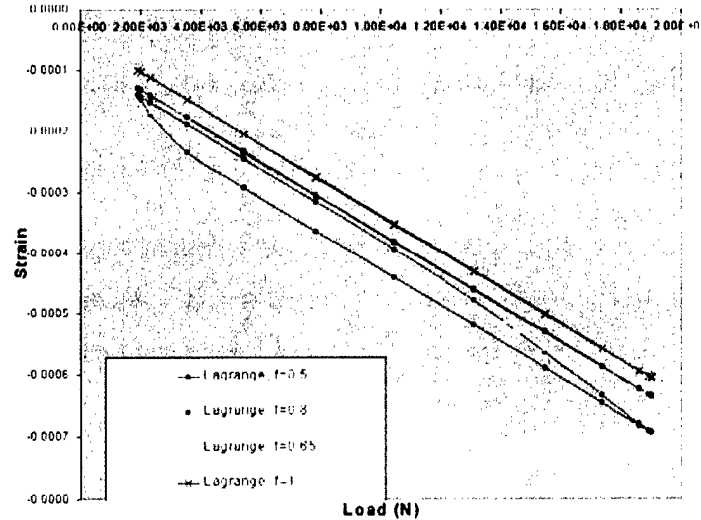


Figure 3-7: The calculated hysteresis loop over two cycles of loading for several values of the coefficient of friction.

to slip to increase efficiency. However, partial-slip conditions would not be accurately modeled with a penalty method, so the cost must be accepted. A coefficient of friction of 0.5 was chosen for all models except that of the coated dovetail which had  $f=0.2$ . More will be said on the coated dovetail in the chapter on palliatives.

To obtain a stable hysteresis loop, two cycles of loading are performed. Each half cycle was broken into 15 steps. The steps were the minimum load, 5% of the cycle's half-period, 10%, 20%, 30%, 40%, 50%, 60%, 70%, 80%, 90%, 95%, 97.5% and maximum load. The reduction of step size near maximum load was necessary for the model to converge.

The evolution of friction during the first two cycles was examined by plotting the calculated strain versus the applied bulk load to the dovetail specimen. As shown in Figure 3-7, the shape of the curve is strongly influenced by the coefficient of friction. The hysteresis loop becomes closed as the coefficient of friction increases. The response in the model is not as stiff as the actual response measured by the strain gauges, see Figure 3-8. This may be the result of the two dimensional nature of the model or an error in the material properties.



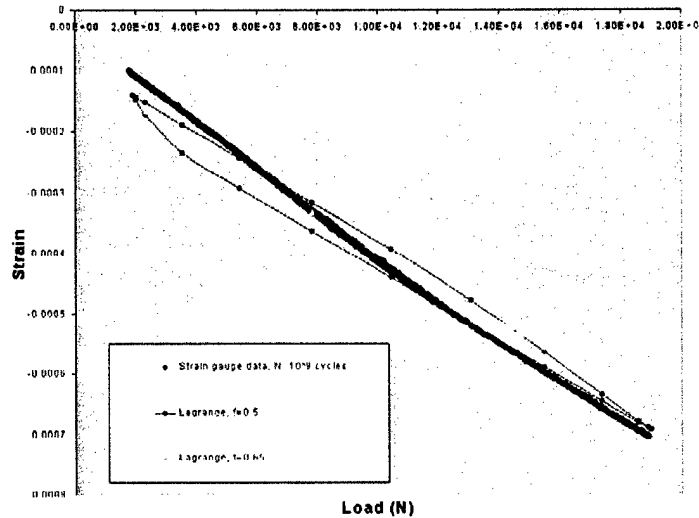


Figure 3-8: The strain versus load response measured at the strain gauge compared to the calculated response from the model.

### 3.2.1 Obtaining point loads from the finite element model

As presented earlier, determining contact point loads is impossible without outside information (numerical modeling or devices such as the strain gauge) since the loads are statically indeterminate. An infinite number of magnitudes of  $P$  and  $Q$  could be found for a given  $F$ . One approach numerically, would be to use a cylindrical contact geometry for the desired  $F$  (even if the actual contact geometry is not cylindrical). The cylindrical contact will produce a parabolic pressure distribution with known relationships for  $a$  and  $P$ . Since the pressure goes to zero at the edge of contact, one can determine  $a$ , then  $P$  can be found.

An understanding of the applied forces will help. Consider the dovetail shown in Figure 3-9. Three points are shown. A force  $F$  is applied in the  $x_2$  direction to the bottom cylindrical portion of the specimen at point  $A$ . The two points along the flanks of dovetail represent the centroid of the contact. These are named points  $L$  and  $R$  for left and right. The following assumptions are made. First, that the contact problem can be modeled using static equilibrium (i.e.  $\sum F_i = 0, \sum M_i = 0$ ). There are no body forces in this model. Second, the contact loads

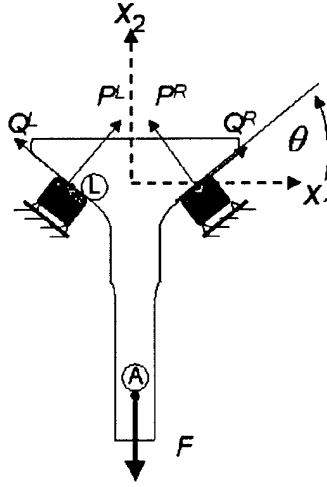


Figure 3-9: A schematic of the boundary conditions and loads involved in the dovetail model.

are located at the centroid of the contact throughout the entire loading cycle. In other words, there is no “tipping” or off-center loading. As a result of applying  $F$ , there are loads normal and tangential to the contact surface,  $Q$  and  $P$ , at  $L$  and  $R$  (with subscripts denoting which side the force is applied to).  $F$ ,  $Q^L$ ,  $Q^R$ ,  $P^L$  and  $P^R$  are vector forces and related via the force balance equation

$$\vec{F} = \vec{Q}_2^L + \vec{Q}_2^R + \vec{P}_2^L + \vec{P}_2^R \quad (3.2)$$

The subscript 2 denotes the components of the vectors  $Q$ ,  $P$  in the  $x_2$  direction. Take  $\theta$  to be the angle between the contact face and the  $x_1$  axis. By symmetry,  $\vec{Q}_2^L = \vec{Q}_2^R$  and  $\vec{P}_2^L = \vec{P}_2^R$ , so

$$F = 2Q^R \cos\left(\frac{\pi}{2} - \theta\right) + 2P^R \cos(\theta) \quad (3.3)$$

A quick check can verify this equation. If  $\theta = \frac{\pi}{2}$ , then there should be no normal force and the dovetail would slide out of the slot. If  $\theta = 0$ ,  $F$  would produce only a normal load on the contact (this dovetail would have an unusual appearance). The equation bears out both

Description	R	$F_{\max}$ (kN)	P (kN/m)	% error	Q (kN/m)	$N_f$ (cycles)
Cylinder	0.1	19	1258	$\pm 2.1$	505	$1 \times 10^6$
Short flat	0.1	18.3	1130	$\pm 6.2$	568	$1 \times 10^6$
Long flat	0.1	20.1	1195	$\pm 2.9$	670	$1 \times 10^6$
Short flat	0.5	21.4	1285	$\pm 7.6$	654	$1 \times 10^6$
Short flat, LPB	0.1	18.3	1130	$\pm 6.2$	568	runout
Short flat, LPB	0.1	27.3	1485	$\pm 8.8$	1048	$1 \times 10^6$

Table 3.4: Loads as determined via FEM. LPB is low plasticity burnishing and will be described in Chapter 6.

of these limiting cases.

Still,  $Q^R$  and  $P^R$  can take any range of values which satisfy this relationship.  $Q$  is a frictional force. If there was no friction,  $Q$  would be zero. This condition is the upper bound of  $P$ . The lower bound comes from the restriction that  $Q \leq fP$ . The exact result comes about as a result that the load is not applied at a point (or a line of unit thickness) but rather over the region of contact. The finite element model discretizes the region of contact and gives a reasonably accurate approximation for  $P$ . If  $p_o$  can be determined from the model, then  $P$  can be found since

$$a = \sqrt[3]{\frac{3PA}{8k}} \quad (3.4)$$

Figure 3-10 is a plot of the pressure for an applied load of 1.9 kN on the dovetail and a cylindrical contact pad. The pressure should go to zero at the edge of contact, thus  $a$  can be measured from a plot of the pressure.  $P$  could also be determined from the maximum contact pressure, but notice the large scatter in  $p$  near  $p_o$ . Thus, measuring  $a$  is preferable to measuring  $p_o$  when finding  $P$ . Errors occur as numerical approximations cause nonzero pressures at the edge of contact or zero pressures at nodes close to but interior to the actual edge of contact.  $a$  can also be obtained from the location where the opening or gap function is nonzero. The same types of numerical errors are present in that analysis.

The upper bound for the normal load occurs when  $f = 0$  and therefore  $Q = 0$ . As shown in 3.5, the calculated normal load is much smaller than the upper bound. The lower bound can be set to be sliding or  $Q = fP$ . In most cases, the calculated normal load is near or slightly above (a numerical error) the value of sliding.

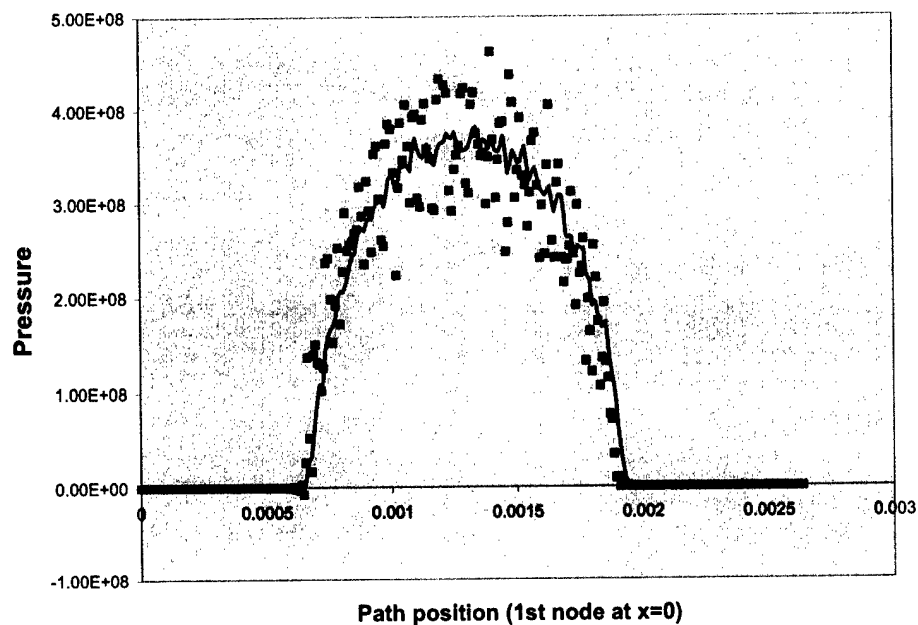


Figure 3-10: A plot of the pressure for a cylindrical contact of a dovetail specimen loaded at  $P=1900$  N. Notice the large scatter in pressure values near the maximum contact pressure.

Description	P (kN/m)	Upper bound
Cylinder	1258	1763
Short flat	1130	1698
Long flat	1195	1865
Short flat, R=0.5	1285	1986
Short flat, LPB	1130	1698
Short flat, LPB	1485	2533

Table 3.5: Loads as determined via FEM compared with the upper bound when  $f=0$ .

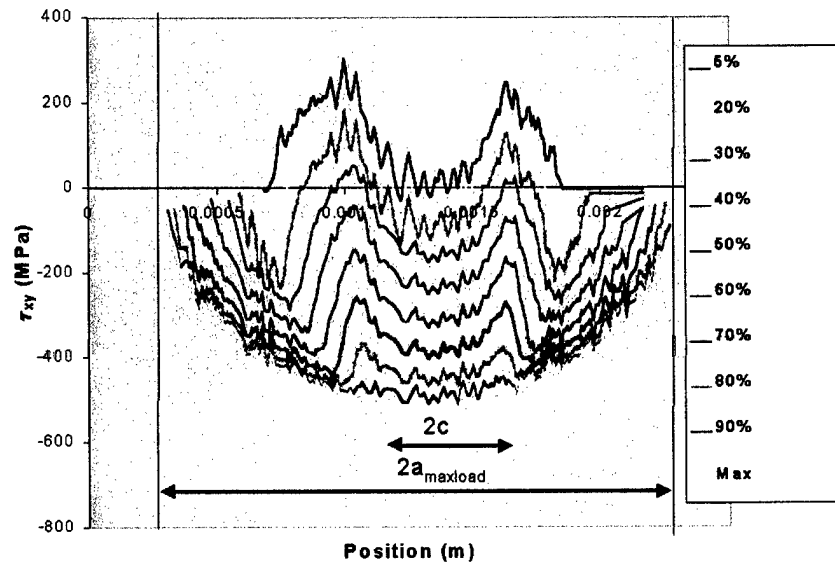


Figure 3-11: The evolution of shear tractions from 5% of maximum load to 100% of maximum load for a dovetail specimen contacted by a cylindrical pad.  $f=0.8$ .

### 3.2.2 Evolution of the shear traction of a cylindrical geometry during the loading cycle.

The finite element model also yields the shear tractions during loading. Consider the case of a dovetail specimen in contact with cylindrical pads and  $f = 0.8$ . A cyclical load is applied to the specimen with load ratio of 0.1 and a maximum load of 19 kN. Increasing the load from minimum to maximum load results in an evolution of the shear traction as shown in Figure 3-11. The contact length, and as a result the area of the shear traction, increases as the normal load increases. The stick zone,  $2c$ , remains nearly the same size throughout the loading cycle until 80% of the maximum load.  $2c$  then rapidly shrinks until sliding occurs until the maximum load is reached.

## Chapter 4

# Observations of fretting fatigue micro-damage

### 4.1 Background

A fundamental understanding of fretting fatigue cannot be obtained without the observation of fretting fatigue damage at small scales. These observations can help to clarify the role of wear damage and contact stresses to the development of fatigue cracks. Some researchers have made notable effort to determine the relationship between wear damage and fretting fatigue life. This is primarily accomplished through the measurement of displacement and the development of wear mapping [23, 65]. Considerable experimental work is required on given contact geometries to develop such maps. On the other hand, stresses and strains are more universal. Thus, there has been a recent focus on more quantitative contact fatigue experiments and analysis that emphasizes stress and strain effects [25, 37, 38, 62]. If advances can be made in this arena, fretting fatigue life-prediction can be extended to various contact geometries. It has been determined that life-prediction based on the location of maximum stress or shear at the surface generally fails to predict life accurately and is not universal outside given contact conditions [66].

There is a need for a more comprehensive view of fretting damage across a variety of loading conditions that examines the surface damage mechanisms from a mechanical viewpoint. These mechanisms contribute to the uncertainty in contact fatigue life-prediction. A literature search

reveals only a few examples of substantial research into fretting fatigue damage. Antoniou and Radtke [67] examined the mechanisms of fretting fatigue damage in Ti-6Al-4V and Ti-17 but only with a bridge pad apparatus. Neu et al. demonstrated a link between crystal-plasticity and surface damage [68] while Pape et al. noticed tribologically transformed regions under a stainless-steel fretting contact [69]. Sauger et al. used several methods to identify tribologically transformed structures in various materials including Ti-6Al-4V and developed a strain-based model of phase transformation [70]. However, the strain-based model of phase transformation failed to predict the correct solute concentrations that result in tribological phase transformation of Ti-6Al-4V.

The knowledge of the interaction of wear and stresses also impacts maintenance of components and surface engineering. The design engineer must determine whether wear reduction or stress reduction is desired. Wear in tight fitting joints could lead to unacceptable part tolerances. However, some wear may be preferred if fatigue cracks are removed by the wear. Damage mechanisms affect the choice of palliative. A hard coating could prevent wear, but it may also delaminate if large strains are applied to the substrate as is so often the case in fretting fatigue versus fretting wear.

## **4.2 Section preparation**

Specimens were cut by a low speed diamond saw through the fretting scar and parallel to the bulk loading axis. Then the sections were ground using SiC paper of grit numbers 600, 1200, 2400 and 4000 grit paper. Finally, the section was polishing with alumina and diamond paste down to surface roughness near 0.05 microns. Polishing was followed by cleaning and the sections were placed in a desiccant prior to examination in the SEM.

## **4.3 Description of fretting cracks and damage**

### **4.3.1 Sphere-on-flat geometries**

A description of the sphere-on-flat experiments using the MIT apparatus is given in Chapter 2. For the sphere-on-flat geometry, observations [37] reveal that fretting cracks initiated on the

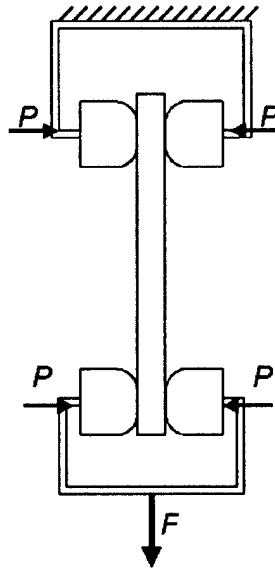


Figure 4-1: A schematic of the flat-on-flat fixture developed at AFRL.

centerline of the contact region ( $y=0$ ) near the edge of contact closest to the actuator ( $x=-a$ ). Cracks tend to initiate in this location since the edge of contact closest to the actuator is the trailing edge of contact (hence the maximum contact stresses [71]) at the same time maximum tension is applied to the specimen. Micrographs show that several cracks develop within  $\pm 25 \mu\text{m}$  of the edge of contact. In other words, cracks will develop in the region of slip or just outside the region of slip.

#### 4.3.2 Dovetail fixture

Chapter 3 describes the dovetail fretting fatigue fixture and experiments performed using that fixture. In order to examine the fretting fatigue scars on the dovetail specimens, a 3 point bend apparatus was developed that could be placed in an SEM. By placing the scar in tension, cracks are revealed through the wear debris as the crack mouths open. Cracks are found on the side of the dovetail scar closest to the actuator (just as in sphere-on-flat contacts) and in the slip region. The location of the edge of contact varies since the normal load is cyclic. Besides the dominant cracks, multiple cracks with widths on the order of  $20 \mu\text{m}$  are found in



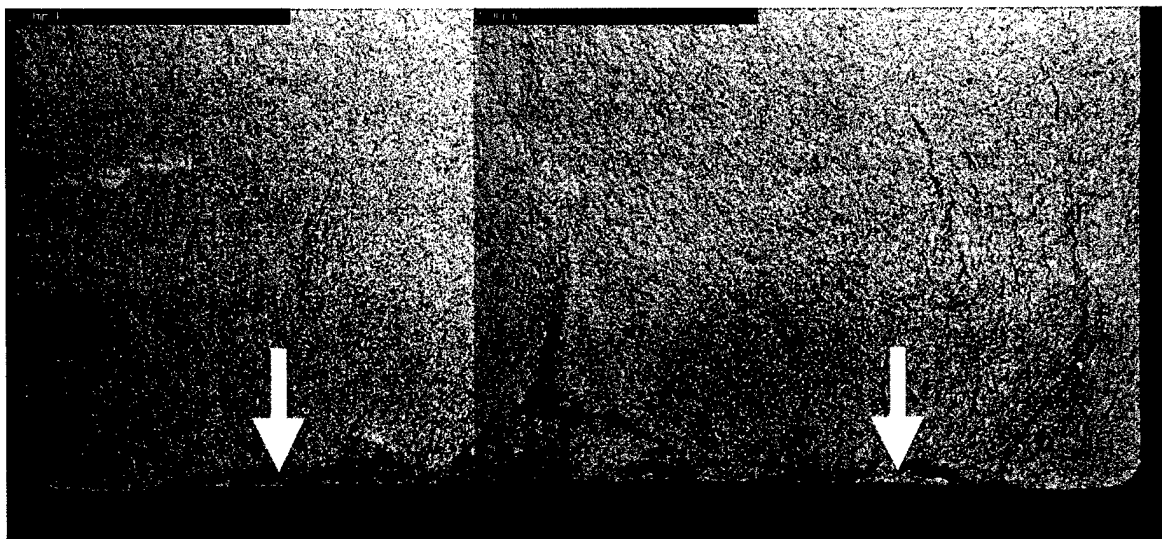


Figure 4-2: Two fretting cracks initiated (location shown by arrows) and linked.

the slip region. This phenomenon of nearly simultaneous multiple crack initiations is common throughout the contact geometries and fixtures as will be shown below.

Figure 4-2 is a dovetail specimen where cracks initiated at two locations almost equidistant from the center of the specimen width. Semi-quantitative elemental analysis near the sites of initiation reveal a presence of oxygen much stronger than the oxide on the fracture surface away from the region of initiation. Combined with the morphology of the fracture surface near the region of initiation, it is apparent the dark regions near the contact surface are oxides that formed via the wear process and have entered the crack to a depth of 100  $\mu\text{m}$ .

#### 4.3.3 Flat on flat

Specimens were examined from a fixture that clamped a thin flat specimen with flat pads shown schematically in Figure 4-1. These pads were typically flat with rounded edges. The clamping bolts were instrumented to measure the normal force. The ends of the specimen were free, and one set of pads was fixed. The set of pads on the opposite end of the specimen was loaded uniaxially. Thus, the axial load is provided through the clamped pads, and the bulk stress is the load divided by the cross-sectional area of the specimen. The tangential load is simply the

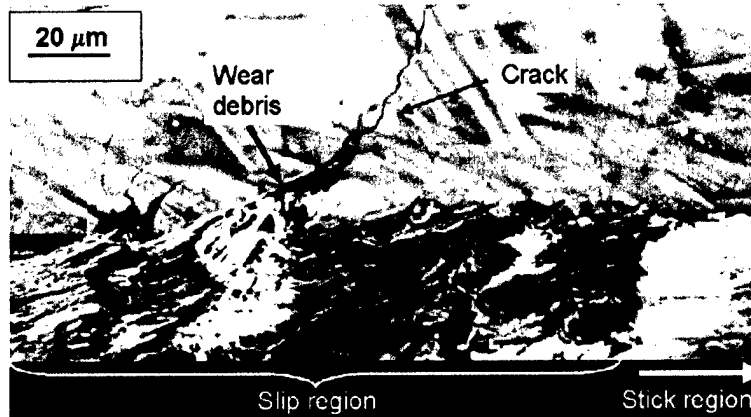


Figure 4-3: Debris flows into a crack in the slip region of a dovetail specimen. The contact pad was a short flat with taper.

applied load divided by two. This specimen has the advantage that failure typically occurs at one set of pads first. Thus, the contact under the opposite set of pads can be examined.

While the overall stresses from the contact fatigue are elastic or elastic after shakedown [72], there is some plastic deformation near the surface as the stresses in asperity tips exceed yield. As shown in Figure 4-4 taken from a specimen contacted by a rounded flat pad, asperities harden and then are removed leaving behind small craters. Cracks may develop in these craters. Shallow cracks will remove asperities and increase the size of wear craters. Inclined cracks may propagate into the material.

#### 4.3.4 Shot peened specimens

Figures 4-5 to 4-8 are micrographs taken from specimens that were shot-peened so crack propagation was suppressed. Figure 4-5 shows significant plastic deformation due to wear in the slip region. One 20  $\mu\text{m}$  crack and three small notches are clearly visible. These notches served as initiation sites for fatigue cracks. At higher magnification (Figure 4-6), a small crack can be seen growing out of one of the notches. Typically, one dominant crack grows although it may be formed by the linkage of smaller cracks. The damage in Figure 4-5 looks very similar to what would be expected by crystal plasticity modeling of fretting in Ti-6Al-4V [68].

Figure 4-7 clearly shows cracks that are filled with wear debris. The smallest crack is about

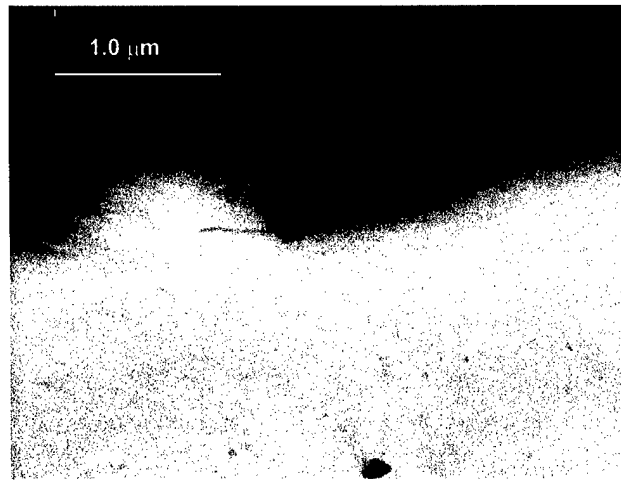


Figure 4-4: A crack from a wear crater grows into an asperity.

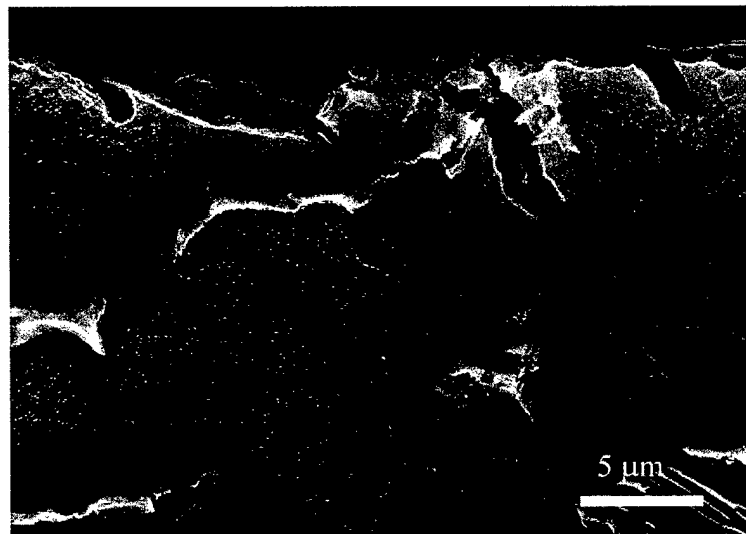


Figure 4-5: SEM image of surface damage showing delamination and the formation of small notches developing into cracks ( $P=50$  N,  $Q=27.5$  N,  $N=300,000$  cycles,  $\sigma_{axial}=270$  MPa,  $R=0.1$ ,  $r=12.7$  mm).

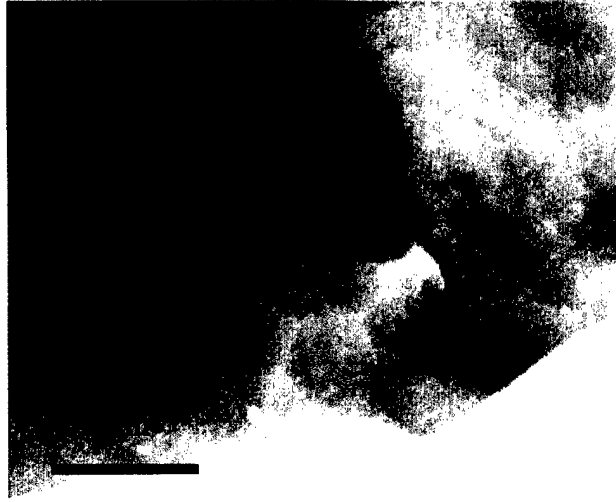


Figure 4-6: A small crack ( $0.5 \mu\text{m}$ ) growing out of a notch. This is one of the notches shown in the above photo.

$3 \mu\text{m}$  long (Figure 4-8). Even at such a small length the crack is filled with debris that would obviously impact the growth behavior of the crack.

There is general agreement that fretting fatigue crack growth consists of 4 regimes. The first is crack nucleation. This includes accumulation of damage leading to crack initiation and incipient crack growth. The second is propagation by the combination of the contact and bulk stresses. This regime lasts until the total stress asymptotically approaches the stress-state of the bulk material. The third then is crack propagation solely by the bulk stresses. The fourth regime is that of fast fracture and can be neglected in terms of the overall fatigue life [39]. The observations above agree with this approach to fretting fatigue crack growth. In the shot-peened specimens, the second regime was suppressed by the presence of compressive residual stresses.

#### 4.4 Impact of micromechanisms on life-prediction modeling

It has been observed in experiments using specific contact geometries that multiple cracks initiate nearly simultaneously [73]. However, only one or two cracks will become dominant and propagate to failure. Our observations indicate that this phenomenon is true regardless

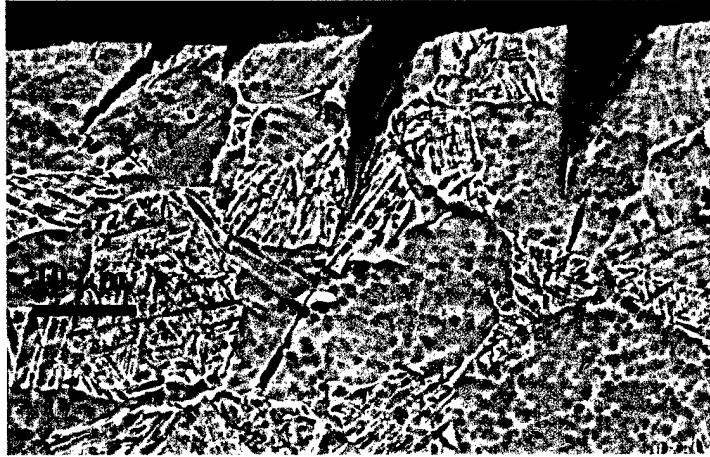


Figure 4-7: Wear debris fill fretting cracks.

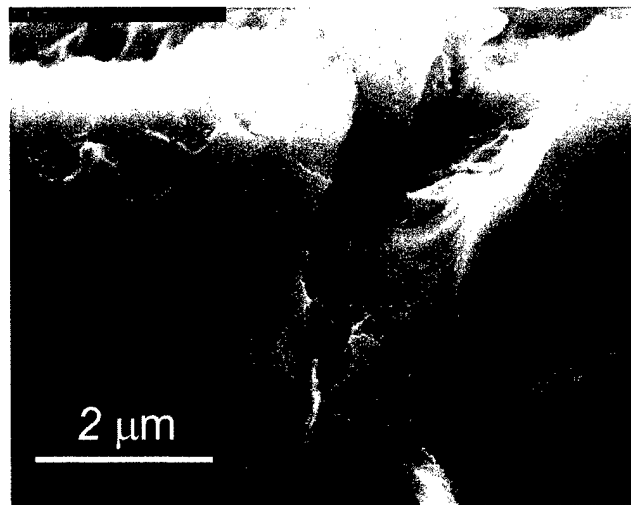


Figure 4-8: Small fretting fatigue crack filled with wear debris.

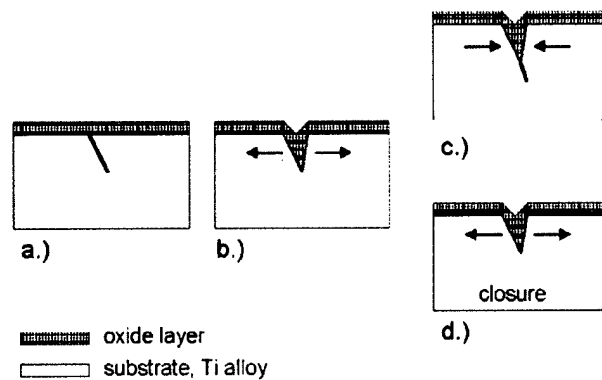


Figure 4-9: a.) A small crack has developed near the edge of contact. b.) Oxides developed by wear enter the crack as it is opened by contact and bulk tensile stresses. Either one of two effects occur: c.) the crack jumps ahead of the wedge during compressive loading or d.) crack growth is slowed by closure.

of contact geometry or loading condition. It has been postulated that the near simultaneous initiation of cracks would result in crack shielding. Thus, fracture mechanics based modeling of cracks growing out of this region may need to adjust  $\Delta K$  to an effective  $\Delta K$  to account for shielding effects.

The micro-mechanism of wear debris can be expected to impact fracture-mechanics based life-prediction models. Once a crack initiates and is opened by the tensile portion of the fretting fatigue loading, wear debris at the surface may enter into the crack, see Figure 4-9 a and b. This will produce one of two effects on crack growth. Recalling that stresses at the leading edge of contact are compressive, the first effect is that crack growth may accelerate upon compression of the crack if the oxide is more stiff than the matrix material, see Figure 4-9 c. This effect is reduced as crack length increases since  $R$  will increase as depth increases. The other effect is that the oxides may close the crack and divert energy from the crack tip, see Figure 4-9 d.

From early research in steels, it has been shown that as the displacement or the ratio of  $Q_{\max}/(fP)$  increases from zero, the number of cycles to failure reaches a minimum then increases [23, 74]. The wear damage due to contact is a function of the displacement. It has

been postulated that increased wear damage may remove small cracks. The fatigue life and wear removal rates are shown qualitatively as functions of the displacement in Figure 4-10. However, the increase in wear also results in an increase in the production of wear particles that can enter cracks and retard propagation. The ratio of crack removal and crack filling would change as a function of the displacement with the former becoming more dominant in the region of global sliding. However, at a given point in the partial-slip regime, the rate of change in the fatigue life as a function of displacement is reduced until the minimum in fatigue life is reached. This is due to the filling of cracks by wear particles as the wear rate is insufficient to remove small cracks. Otherwise we would expect both a constant rate of change in the fatigue life (in partial-slip) as a function of displacement as well as a sharp transition in fatigue life and mechanisms upon sliding. Therefore, the effective stress-intensity factor from above should now also include the effects of the wear particle by becoming a function of displacement.

$$\Delta K_{eff} \rightarrow \Delta K_{eff}(l, \delta \text{ or } Q/fP) \quad (4.1)$$

where  $l$  is the crack length and  $d$  is the displacement. No attempt is made in this paper to derive this relationship.

Crack arrest also impacts life-prediction modeling. There are several reasons why fretting fatigue cracks nucleate and then arrest. These include the combined effects of shielding, wear filling of cracks, crystal orientation of near surface grains and the combination of contact and bulk stresses below the contact interface. Merely determining crack initiation based on local stresses may be overly conservative. Such methods may predict crack initiation but fail to incorporate the effects of micromechanisms that would prevent further nucleation. Likewise, short-crack fracture mechanics methods may be also overly conservative because of crack closure due to wear debris in cracks as small as 3  $\mu\text{m}$ . Both initiation-based and fracture mechanics based life-prediction methods may be conservative because of the effects of the stress-state and micro-mechanisms. Stress/strain-at-a-point methods would fail to capture any of these effects. Introduction of a length-scale such as a volume-averaging effect or fracture mechanics-based method would help capture the gradient in contact stresses, but not the micromechanical effects, induced by crack-filling for example. The initiation of multiple cracks can affect the application of fracture mechanics. For an example, see [75, 76]. Crystal plasticity modeling

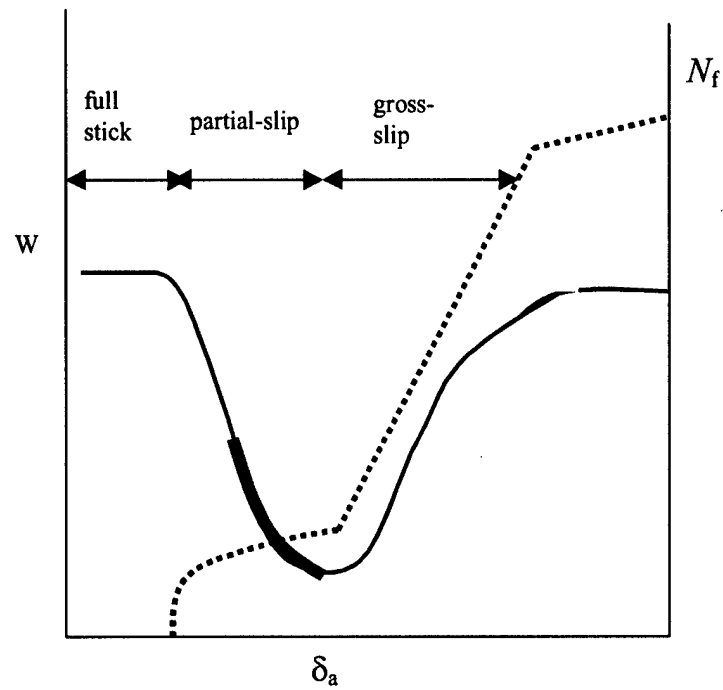


Figure 4-10: A schematic of the dependence of the fatigue life and the wear volume loss ( $W$ ) on the fretting displacement slip amplitude. The highlighted region is the region where wear debris most impacts fatigue life.



may reveal more information on near-surface plasticity and wear. To incorporate explicitly all of these micromechanisms would be extremely difficult for engineering design. One should determine the most important micromechanisms for a given contact geometry and loading, and incorporate those in life-prediction methods.

## 4.5 Friction and its evolution

### 4.5.1 A derivation of the spherical contact load history

If fretting starts at a constant frequency and load (i.e. neither load or frequency is ramped), then the coefficient of friction will be uniform and equal to  $f_o$  throughout the contact area. Wear damage in the slip regions will increase the coefficient of friction to  $f_n$  after  $n$  cycles. Because of the increase in friction, the stick zone will grow in size from  $c_o$  to  $c_n$ .

This new stick zone is described by the relationship

$$\frac{c_n}{a} = \sqrt[3]{1 - \frac{Q}{fP}} \quad (4.2)$$

After several hundred (or perhaps thousands) of cycles, the coefficient of friction will become steady-state.

The coefficient of friction in the region of stick ( $0 < x < c_o$ ) is statically indeterminate. The shear traction,  $q$ , and the normal traction,  $p$ , are related by

$$q(r) = \lambda p(r) \quad (4.3)$$

In the region  $c_o < x < c_n$ , the coefficient of friction may vary as a function of position as well as time. Hills and Nowell suggested the following relationship for  $q$  and  $p$  [16].

$$q(r) = f(r)p(r) \quad (4.4)$$

The value of  $f(x)$  is unknown in this region.

Finally, in the region  $c_n < x < a$ , the coefficient of friction is again constant but takes the modified value,  $f_n$ .

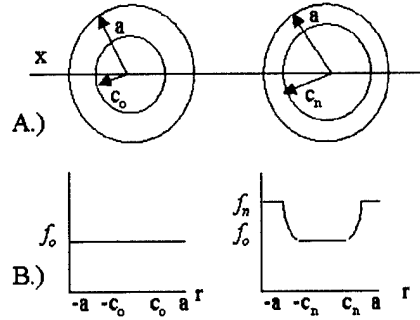


Figure 4-11: The coefficient of friction is initially constant in across the contact patch (shown here to be circular). Over  $n$  cycles, the coefficient of friction will increase in the slip region as a result of wear. Therefore, the radius of stick will also increase.

$$q(r) = f_n p(r) \quad (4.5)$$

Even though friction may vary from point to point, there is a macroscopic coefficient of friction,  $\bar{f}$ . This can be described by the following ratio.

$$\bar{f} = \frac{Q}{P} = \frac{\int q dA}{\int p dA} \quad (4.6)$$

$dA$  is the differential in area. If fretting starts at a constant frequency and load (i.e. neither load or frequency is ramped), then the coefficient of friction will be uniform and equal to  $f_o$  throughout the contact area. Wear damage in the slip regions will increase the coefficient of friction to  $f_n$  after  $n$  cycles.

By solving 4.6, the variation of the coefficient of friction in the slip zone over  $n$  cycles can be determined experimentally. Hills and Nowell describe this as “stopping the fretting [after  $n$  cycles] and then slowly increasing the tangential force until sliding occurs.” The closed-form analytical solution for the evolution of friction for the contact of cylinders problem is given by Hills, Nowell and Sackfield [24]. However, the solution of the problem for the contact of spheres has not been completed, yet this is relevant to our experimental work.

In 4.6, it must be noted that  $dA = r dr d\theta$ , thus

$$\int p(x) dA = p_o \int_0^{2\pi} \int_0^a \sqrt{1 - \left(\frac{r}{a}\right)^2} r dr d\theta = \frac{2\pi a^2}{3} p_o \quad (4.7)$$

and therefore

$$\frac{2\pi a^2 \bar{f}}{3} = 2\pi \left\{ \int_0^{c_o} f_o \sqrt{1 - \left(\frac{r}{a}\right)^2} r dr + \int_{c_o}^{c_n} f(r) \sqrt{1 - \left(\frac{r}{a}\right)^2} r dr + \int_{c_o}^{c_n} f_n \sqrt{1 - \left(\frac{r}{a}\right)^2} r dr \right\} \quad (4.8)$$

which if differentiated with respect to the number of cycles is (assuming, as is the case with Hills et al that  $f(x)$  is not dependent on  $n$ )

$$\frac{2\pi a^2}{3} \frac{\partial \bar{f}}{\partial n} = \frac{\partial f_n}{\partial n} \left\{ \frac{2\pi a^2}{3} \left( 1 - \left(\frac{c_n}{a}\right)^2 \right)^{3/2} \right\} \quad (4.9)$$

and from 4.2 is

$$\frac{\partial \bar{f}}{\partial n} = \frac{\partial f_n}{\partial n} \left\{ \left( 1 - \left( 1 - \frac{Q}{f_n P} \right)^{2/3} \right)^{3/2} \right\} \quad (4.10)$$

therefore

$$\bar{f} - f_o = \int_{f_o}^{f_n} \left( 1 - \left( 1 - \frac{Q}{f_n P} \right)^{2/3} \right)^{3/2} df_n \quad (4.11)$$

This integration can be accomplished numerically taking with  $f_n = Q/P$  if fretting starts after an initial period of sliding.

This equation demonstrates that in the absence of adhesive forces, the relationship between the macroscopic coefficient of friction and the variation of friction in the slip zone is not a function of the pad radius or the material properties. It is only a function of the ratio of the normal and tangential loads. Thus, this can be used for a variety of experimental conditions. A plot of this relationship is shown Figure 4-12.

It should be noted that the cylindrical contact solution can be derived analytically as done by Hills, Nowell and Sackfield [24] resulting in

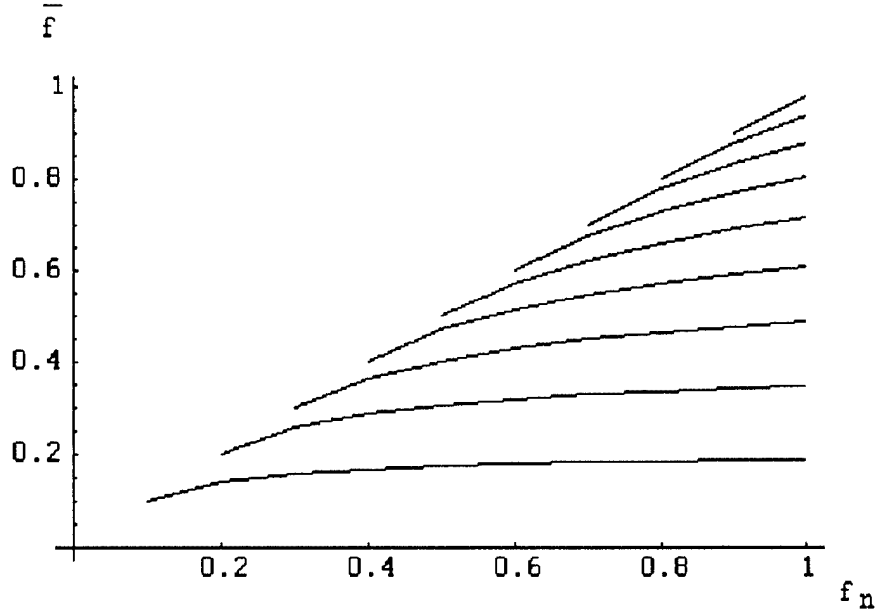


Figure 4-12:  $\bar{f}$  versus  $f_n$  for selected values of  $Q/P$

$$\bar{f} = f_n - \frac{2Q}{\pi P} \left( -2 \sin \alpha + 2 \ln \left[ \tan \left( \frac{\alpha}{2} + \frac{\pi}{4} \right) \right] + \frac{P f_n \alpha}{Q} - \tan \alpha \right) \quad (4.12)$$

where  $\alpha$  is defined as:

$$\cos \alpha = \frac{Q}{f_n P} \quad (4.13)$$

If we plot  $\bar{f}$  versus  $f_n$  for given  $Q/P$ , there is distinctly different behavior between the point contact and the line contact as shown in Figure 4-13. The behavior of the line contact is well known from Hills, Nowell and Sackfield.

#### 4.5.2 A review of the cylindrical contact load history

The evolution of the load history for cylindrical contacts was first examined by Hills, Nowell and Sackfield. To review, the pressure distribution for a normal load applied to a cylindrical contact is:

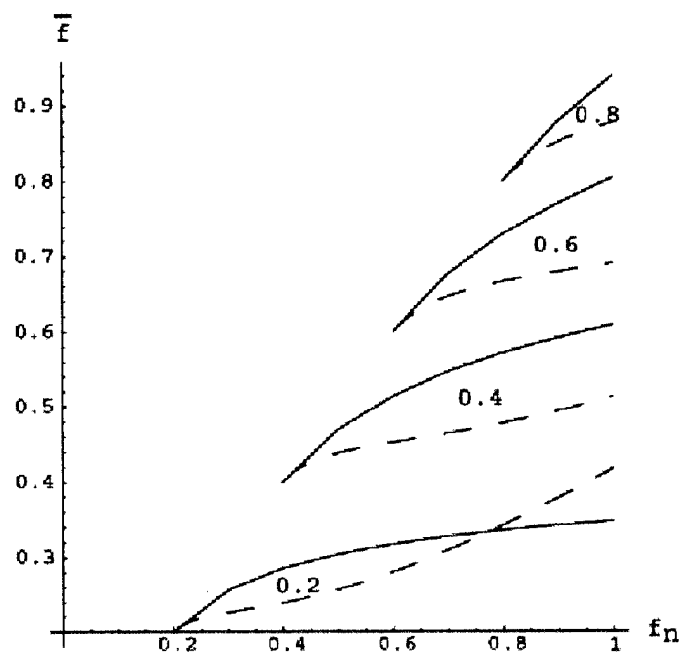


Figure 4-13: The relationship between  $\bar{f}$  and  $f_n$  is different for spherical and cylindrical contacts. The dashed lines represent the cylindrical contact.

$$p(x) = -p_o \sqrt{1 + \left(\frac{x}{a}\right)^2} \quad (4.14)$$

The modified stick zone size is

$$\frac{c_n}{a} = \sqrt{1 - \frac{Q}{fP}} \quad (4.15)$$

If fretting is stopped and the tangential force is increased until sliding, the measured coefficient of friction will be given by

$$\frac{\pi a^2 \bar{f}}{4} = \int_0^{c_o} f_o \sqrt{1 - \left(\frac{x}{a}\right)^2} dx + \int_{c_o}^{c_n} f(x) \sqrt{1 - \left(\frac{x}{a}\right)^2} dx + \int_{c_n}^{c_o} f_n \sqrt{1 - \left(\frac{x}{a}\right)^2} dx \quad (4.16)$$

This equation may now be differentiated with respect to the number of cycles.

$$\frac{\pi a^2}{4} \frac{\partial \bar{f}}{\partial n} = \frac{\partial f_n}{\partial n} \left\{ \frac{\pi}{4} - \frac{c_n}{2} \sqrt{1 - \left(\frac{c_n}{a}\right)^2} - \frac{1}{2} \arcsin \left(\frac{c_n}{a}\right) \right\} \quad (4.17)$$

which gives us

$$\bar{f} = f_n - \frac{2}{\pi} \int_{f_o}^{f_n} \left( \frac{Q}{f_n P} \sqrt{\frac{f_n P}{Q} - 1} + \arcsin \sqrt{1 - \frac{Q}{f_n P}} \right) df_n \quad (4.18)$$

It should be noted that algebraic errors exist in 4.17 and 4.18 in both Hills, Nowell and Sackfield [24] and Hills and Nowell [77]. Despite the errors, the final solution shown above in 4.12 and 4.13 is correct.

### 4.5.3 Incorporating the effects of adhesion

Giannakopoulos, et al proposed that interfacial adhesion could impact the initiation of fretting cracks. Adhesion will change the contact dimensions. For example, the contact radius will increase from  $a$  to  $a_{\max}$ .

$$a_{\max} = \left[ \frac{3D(1-\nu)^2}{4E} \left( P + \frac{3\pi Dw}{2} + \sqrt{3\pi DwP + \left( \frac{3\pi Dw}{2} \right)^2} \right) \right]^{1/3} \quad (4.19)$$

where  $D$  is the diameter of the sphere and  $w$  is the work of adhesion and for most metals is approximately 1 N/m.

Recall from Chapter 1, the normal traction becomes unbounded and is now

$$p(r) = -p_o \sqrt{1 + \left( \frac{r}{a_{\max}} \right)^2} + \frac{p_o^*}{\sqrt{1 + \left( \frac{r}{a_{\max}} \right)^2}} \quad (4.20)$$

where  $p_o^*$  is defined as

$$p_o^* = \frac{wE}{(1-\nu^2)\pi a_{\max}} \quad (4.21)$$

Thus the radius of the stick region after  $n$  cycles of fretting becomes

$$\frac{c_n}{a_{\max}} = \sqrt[3]{1 - \frac{Q}{f_n P}} \quad (4.22)$$

recalling that the initial stick radius is

$$\frac{c_o}{a_{\max}} = \sqrt[3]{1 - \frac{Q}{f_o P}} \quad (4.23)$$

Thus, the inputs in the above equations must be modified so that  $a$  is replaced by  $a_{\max}$ .

$$\bar{f} \int p dA = 2\pi \left\{ f_o \int_0^{c_o} \sqrt{1 - \left( \frac{r}{a_{\max}} \right)^2} r dr + \int_{c_o}^{c_n} f(r) \sqrt{1 - \left( \frac{r}{a_{\max}} \right)^2} r dr + D' \right\} \quad (4.24)$$

where  $D'$  is

$$D' = \int_{c_n}^{a_{\max}} f_n \left\{ \sqrt{1 - \left( \frac{r}{a_{\max}} \right)^2} - \frac{1}{\sqrt{1 - \left( \frac{r}{a_{\max}} \right)^2}} \right\} r dr \quad (4.25)$$

and the pressure changes to:

$$\int p(x) dA = p_o \int_0^{2\pi} \int_0^{a_{\max}} \sqrt{1 - \left(\frac{r}{a_{\max}}\right)^2} r dr d\theta - p_o^* \int_0^{2\pi} \int_0^{a_{\max}} \frac{1}{\sqrt{1 - \left(\frac{r}{a_{\max}}\right)^2}} r dr d\theta = \frac{2\pi a_{\max}^2}{3} (p_o - 3p_o^*) \quad (4.26)$$

Again, differentiate with respect to the number of cycles

$$\frac{2\pi a_{\max}^2}{3} (p_o - 3p_o^*) \frac{\partial \bar{f}}{\partial n} = \frac{\partial f_n}{\partial n} \left[ 2\pi \int_{c_n}^{a_{\max}} \left\{ \sqrt{1 - \left(\frac{r}{a_{\max}}\right)^2} - \frac{1}{\sqrt{1 - \left(\frac{r}{a_{\max}}\right)^2}} \right\} r dr \right] \quad (4.27)$$

Thus

$$\frac{2\pi a_{\max}^2}{3} (p_o - 3p_o^*) \bar{f} = \int_{f_o}^{f_n} \left[ 2\pi \int_{c_n}^{a_{\max}} \left\{ \sqrt{1 - \left(\frac{r}{a_{\max}}\right)^2} - \frac{1}{\sqrt{1 - \left(\frac{r}{a_{\max}}\right)^2}} \right\} r dr \right] df_n \quad (4.28)$$

These integrals can be solved numerically.

The relationship between  $\bar{f}$  and  $f_n$  is dependent on the contact loads **and** the contact geometry or pressure. Figure 4-14 shows the variations in and several values of  $w$  for a spherical contact with a pad radius of 25.4 mm and elastic properties of  $E=116$  GPa and  $\nu=0.3$ . The equation is very sensitive to the value of  $w$ . As  $w$  increases, the minimum possible value of the coefficient of friction in the slip zone increases. As the value of  $w$  approaches 1, the relationship becomes linear. These observations agree with the physics of the process. The separate effects of adhesion and surface roughness (which is changed by wear) are included in the coefficient of friction. Just as  $f_n$  will likely increase as  $n$  increases, so must  $f_n$  increase as  $w$  increases.

#### 4.5.4 Experimental results

Fretting fatigue experiments were performed using Ti-6Al-4V specimens and hemispherical pads. The results are described in Table 4.1. The fretting apparatus used is described with detail in Chapter 1. A sinusoidal bulk load is applied to the specimen resulting in a tangential



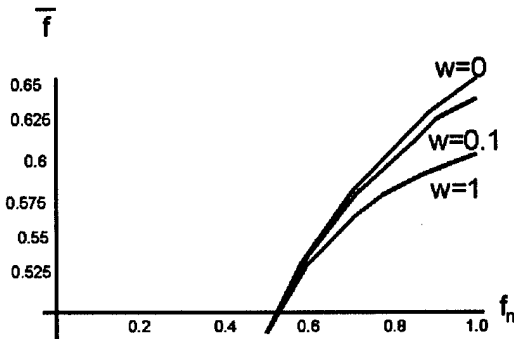


Figure 4-14: A plot of  $\bar{f}$  (the vertical axis) and  $f_n$  (the horizontal axis) for  $w=0, 0.1$  and  $1$ . As  $w$  increases from zero, so does the value of  $\bar{f}$  with respect to  $f_n$ .

	$Q/P$	$n$	$\delta_{\max}(\mu m)$	$\bar{f}$	$f_n (w=0)$	$f_n (w=1)$
2	0.44	1000	0.025	0.4875	0.49	0.55
3	0.4	500	0.027	0.4375	0.44	0.475
4	0.475	350	0.030	0.6	0.63	0.735
5	0.356	100	0.027	0.4375	0.45	0.5

Table 4.1: Experimental results for Ti-6Al-4V on Ti-6Al-4V spherical contact

load in-phase with the bulk load. Load cells enable measurement of the tangential and normal loads while a compliant tangential load train allows for adjustment of the tangential load for a given bulk load.

The experiments were performed at a frequency of 2 Hz and a load ratio of -1. The ratio of  $Q/P$  was near 0.4 for all of the tests. After the desired number of cycles, the test was stopped. Monotonic tensile bulk loading was then applied which resulted in increasing  $Q$ .  $Q$  was monitored through the point of sliding and the value of  $Q/P$  just prior to sliding was recorded. The macroscopic value of friction was equal to  $Q/P$ . The details are given in Table 3.1.

The scatter from the experimental results is large and shows the difficulty of conducting these experiments. Nonetheless, the method is shown to work and can be extended to the vital issue of the fretting of coatings.

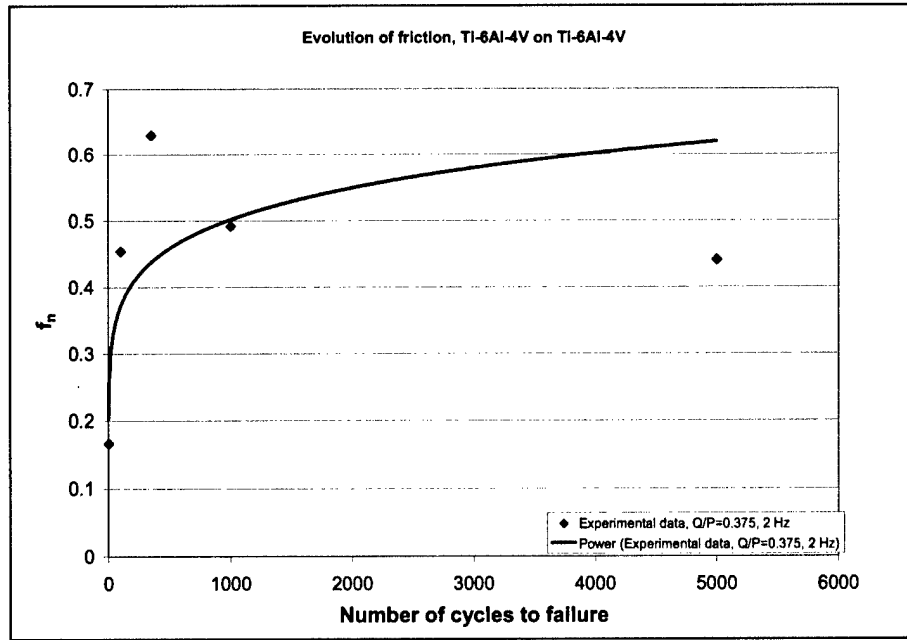


Figure 4-15: Experimentally measuring the coefficient of friction in the slip zone over  $n$  cycles.

## 4.6 Summary

An examination of specimens & pads from 3 different fretting fixtures and 4 different contact geometries revealed several damage mechanisms that are of note. Fretting fatigue produces wear debris that enters cracks as small as  $3 \mu\text{m}$  in length and causes crack closure in very small cracks in Ti-6Al-4V. While wear debris does interact with cracks, the depth of wear or appearance of wear is a poor indicator of contact fatigue life.

The overall contact mechanics in fretting fatigue are elastic, although there is localized plasticity. This results in wear damage at the surface and near-surface ratcheting. Micro-notches form in the wear region with lengths as small as  $1 \mu\text{m}$  and root radii as small as  $0.5 \mu\text{m}$ . These become crack initiation sites and contribute to further wear damage through the development of small cracks that propagate until surface material is removed.

In all of the fretting geometries observed, multiple cracks initiate nearly simultaneously. This encourages crack shielding. It is also true that early crack growth is affected by the crystallographic properties of the near surface grains. As a result of these mechanisms, most

fretting fatigue cracks that do initiate do not propagate but arrest. Only one or two will dominate in propagation

Wear in the regions of slip results in surface modification that changes the coefficient of friction over the first number of cycles of fretting fatigue. Hills, Nowell and Sackfield [24] developed a methodology for determining the coefficient of friction in the slip region for cylindrical contacts. This has now been extended to spherical contacts and to adhesive contacts.

## Chapter 5

# Fracture mechanics based life prediction

Fretting fatigue life can be divided into two segments. The first is crack initiation or nucleation. Physically, this is the period of time required for defects to coalesce into a crack. It is difficult to separate the exact moment that the crack transitions out of initiation and into the second phase of fretting fatigue life known as crack propagation. Because of this ambiguity, it is appropriate to refer to the initiation phase as “nucleation” and specify an initial crack length via the fatigue threshold ( $\Delta K_{th}$ ) or the smallest detectable crack size by current non-destructive evaluation methods.

### 5.1 The need for a length scale

It has been demonstrated that a crack initiation parameter based on stress at a given point is not sufficient [66]. Since stress at a point cannot predict fretting fatigue life, the introduction of a length scale may assist. The significant length scales in contact fatigue are as follows:

- Contact dimensions (radii, geometry,  $a$ ,  $c$ )
- Global,  $g$ , or local displacement,  $\delta$
- Strength of singularity ( $\sigma=f(r)$ )
- Stress gradients ( $d\sigma/dr$ )
- Specimen thickness

- Microstructural length scales such as the grain size
- Rolling contact: diameter of roller or characteristic rolling length

A crack initiation parameter could be developed using any of these length scales. Those length scales not already associated with one of the above dimensions could be combined with one as in the fretting-specific Ruiz parameter ( $\tau\delta$  or  $\sigma\tau\delta$ ) [28].

## 5.2 The crack analogue

Giannakopoulos, Lindley and Suresh [40] recognized an analogy between aspects of contact mechanics and fracture mechanics. Noting that the normal tractions near the edges of a sharp-cornered punch are square root singular [78, 79]

$$\sigma_{zz} \propto \frac{1}{\sqrt{r}} \quad (5.1)$$

a stress-intensity factor could be determined via an analogy with a double-sided edge cracked geometry [80] vis-a-vis a coordinate transformation.

$$\theta \rightarrow \pi - \theta = \phi; \quad 0 \leq \theta \leq \pi \quad (5.2)$$

The normal traction  $p$  has a corresponding  $K_I$  while the shear traction  $q$  has a corresponding  $K_{II}$ . Consider the rigid, frictionless sharp cornered punch of length  $2a$  with a normal load  $P$  and a tangential load  $Q$ . The stress-intensity factors are:

$$K_I = -\frac{P}{\sqrt{\pi a}} \quad (5.3)$$

$$K_{II} = \frac{Q}{\sqrt{\pi a}} \quad (5.4)$$

In the case of the sharp cornered punch, the stress-intensity factor for a fully reversed tangential load  $Q$  is

$$\Delta K_{II} = \frac{2Q}{\sqrt{\pi a}} \quad (5.5)$$

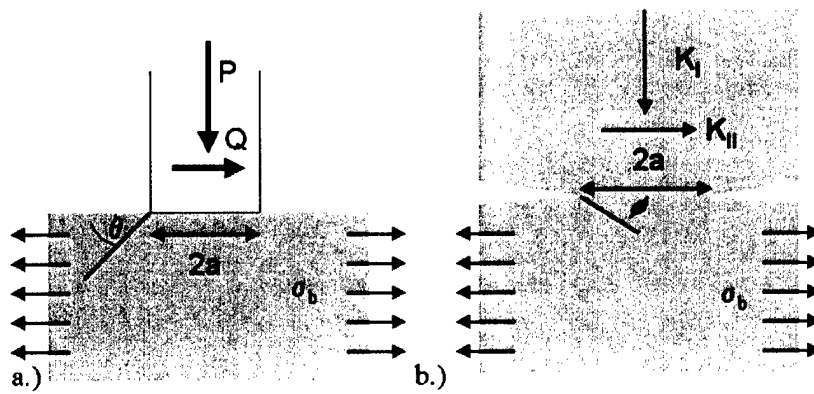


Figure 5-1: Aspects of the rigid punch contact problem in a.) can be equivalent to those of the double edge cracked specimen in b.)

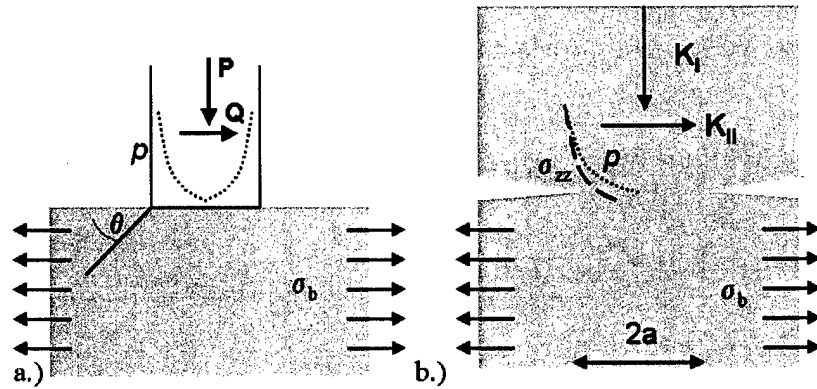


Figure 5-2: The normal traction,  $p$ , in the punch problem is square root singular in the asymptotic limit as one approaches the edge of contact.

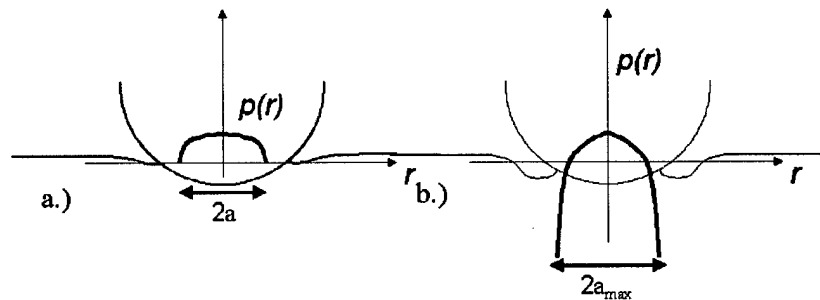


Figure 5-3: For a contact without adhesion, the pressure is bounded and zero at the edge of contact  $\pm a$ . However, the presence of adhesion would cause the pressure to become singular at the new edge of contact,  $\pm a_{\max}$ , for strongly adhered contacts or at the stick zone boundary,  $\pm c$ , for weakly adhered contacts.

Likewise, for cylindrical or spherical punch geometries, an analogy can be made between partial-slip contact mechanics and the contact of weakly adhered surfaces [41]. Stresses near the adhered boundary (analogous to the stick zone in fretting) are square root singular. Tangential point or line loads must be balanced in this stick region. Thus,

$$Q_{\max}^{in} = Q - f \frac{P}{a_{\max}^3} (a_{\max}^2 - c^2)^{3/2}; \text{ spherical contacts} \quad (5.6)$$

and

$$Q_{\max}^{in} = Q - \frac{fP}{\pi} \left\{ \frac{\pi}{2} + \arctan \frac{c\sqrt{a_{\max}^2 - c^2}}{c^2 - a_{\max}^2} - \frac{c}{a_{\max}} \left( 1 - \frac{c^2}{a_{\max}^2} \right) \right\}; \text{ cylindrical contacts} \quad (5.7)$$

where  $a_{\max}$  is an enlarged contact half-width resulting from adhesive forces. For most metals, the adhesive forces are very weak (even for similar metals) particularly in air.

This model produces the following stress-intensity factors

$$\Delta K_{II} = 2 \times \min \left( \frac{Q}{c\sqrt{\pi c}}, \sqrt{\frac{G_d E}{1 - v^2}} \right); \text{ spherical contacts} \quad (5.8)$$

and

$$\Delta K_{II} = 2 \times \min \left( \frac{Q}{\sqrt{\pi c}}, \sqrt{\frac{G_d^{II} E}{1 - v^2}} \right); \text{ cylindrical contacts} \quad (5.9)$$

where  $G_d^{II}$  is the critical shear (hence mode II) debonding energy.  $G_d$  is obtained via the following empirical relationship for a spherical indenter on a metallic surface with friction  $f$  [81]:

$$G_d = 14.3651 \sqrt{0.3 + f^2} \quad (5.10)$$

There is a critical debonding energy corresponding to each mode of loading (normal, shear and torsion), but it is assumed to be equal to or nearly equal to that given by Equation 5.10.



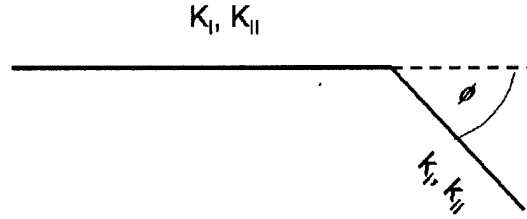


Figure 5-4: A schematic of a kinked crack. The mechanics of a kinked crack will be used to determine crack orientation and early crack growth of fretting fatigue cracks.

### 5.2.1 Crack orientation

If the surface tractions can be related to a stress-intensity factor, crack orientation can be determined from the mechanics of kinked cracks. Consider a crack with a  $K_I$  and  $K_{II}$  that has kinked and the length of the kink is much smaller than the original crack length. The orientation of the kink will be at an angle  $\phi$  with respect to the surface and will have a local  $k_1$  and  $k_2$ . The local stress intensity factors are as follows [82]:

$$k_1 = a_{11}(\phi) K_I + a_{12}(\phi) K_{II} \quad (5.11)$$

$$k_2 = a_{21}(\phi) K_I + a_{22}(\phi) K_{II} \quad (5.12)$$

where  $a_{ij}$  are functions of  $\phi$

$$a_{11}(\phi) = \frac{1}{4} \left( 3 \cos \frac{\phi}{2} + \cos \frac{3\phi}{2} \right) \quad (5.13)$$

$$a_{12}(\phi) = -\frac{3}{4} \left( \sin \frac{\phi}{2} + \sin \frac{3\phi}{2} \right) \quad (5.14)$$

$$a_{21}(\phi) = \frac{1}{4} \left( \sin \frac{\phi}{2} + \sin \frac{3\phi}{2} \right) \quad (5.15)$$

$$a_{22}(\phi) = \frac{1}{4} \left( \cos \frac{\phi}{2} + 3 \cos \frac{3\phi}{2} \right) \quad (5.16)$$

The orientation angle,  $\phi_{\text{in}}$ , is determined by invoking the condition that  $k_2 = 0$ , which infers that cracks do not propagate (or, by analogy, nucleate as a result of the contact fatigue) by shear.

The bulk stress is analogous to the  $T$ -stress in linear elastic fracture mechanics since it is non-zero as the edge of contact is approached. Cotterell and Rice showed that the  $T$ -stress can increase or decrease the angle of the kinked crack [82]. It is then likely that the presence of a bulk stress will change the crack orientation.

### 5.2.2 Early crack growth

$K_{\text{I}}$  is in general is negative and can be monotonic. Thus,  $k_1$  oscillates as a result of  $K_{\text{II}}$ , with a positive  $K_{\text{II}}$  capable of opening the crack. The effective opening stress intensity factor is

$$\Delta k_1 = \pm \frac{3}{4} K_{\text{II}|_{\text{max}}} \left( \sin \frac{\phi_{\text{in}}}{2} + \sin \frac{3\phi_{\text{in}}}{2} \right) \quad (5.17)$$

Physically, the crack will gradually turn normal to the applied cyclic bulk stress. However, this will be modeled as the growth of a crack oriented at angle  $\phi_{\text{in}}$  until a critical length  $l_c$  is reached. At  $l_c$ , the model assumes that crack turns normal to the bulk stress. Giannakopoulos et al. suggest the following method to determine  $l_c$ .

$$\Delta K_{\text{th}} = \frac{\Delta \sigma_{\text{app}} \sqrt{\pi l_c}}{4} \times F(\phi_{\text{in}}) \quad (5.18)$$

$$l_c = \left( \frac{4 \Delta K_{\text{th}}}{\Delta \sigma_{\text{app}} \sqrt{\pi}} \right)^2 \cdot \{F(\phi_{\text{in}})\}^{-2} \quad (5.19)$$

where  $F(\phi_{\text{in}})$  is the stress intensity factor calibration for the doubly kinked crack [83].

$$F(\phi_{\text{in}}) = F_1(\phi_{\text{in}}) \left( 3 \cos \frac{(\pi - 2\phi_{\text{in}})}{4} + \cos \frac{3(\pi - 2\phi_{\text{in}})}{4} \right) + 3F_2(\phi_{\text{in}}) \left( \sin \frac{(\pi - 2\phi_{\text{in}})}{2} + \sin \frac{3(\pi - 2\phi_{\text{in}})}{2} \right) \quad (5.20)$$

Isida provides tables of  $F_1$  and  $F_2$  from which

$$F_1(\phi) \approx 1.058 \sin \phi - 0.065 \sin(3\phi) \quad (5.21)$$

$$F_2(\phi) \approx 0.374 \sin(2\phi) + 0.023 \sin(4\phi) \quad (5.22)$$

However, the crack can turn normal to the surface prior to reaching than the length predicted via Isida. It could happen as soon as the threshold for an edge crack oriented normal to the surface is exceeded. In other words,

$$l_c \sin \phi_{in} = \left( \frac{\Delta K_{th}}{1.12 \Delta \sigma_{app} \sqrt{\pi}} \right)^2$$

Cases where this is applicable are shown below.

Early crack growth can be described via the Paris Law [84].

$$\frac{dl}{dN} = C_1 (\Delta k_1)^{m_1} \quad (5.23)$$

Note that the Paris Law constants have subscript 1. These constants may have different values for early crack growth than for later regimes of fretting fatigue crack growth. Integrating 5.23 equation gives

$$N_1 = \int_0^{l_c} \frac{dl}{C_1 (\Delta k_1)^{m_1}} \approx \frac{l_c}{C_1 (\Delta k_1)^{m_1}}$$

if and only if the approximation is made that the stress-intensity factor does not deviate from  $\Delta k_1$  during kinked crack growth.

### 5.2.3 Later regimes of fretting fatigue crack growth

If the crack is still able to propagate after the early stages of crack growth, then it will grow solely by the bulk stress. The new Paris Law is

$$\frac{dl}{dN} = C_2 (\Delta k_1)^{m_2} \quad (5.24)$$

The subscript 2 denotes Paris Law constants relevant to this regime of crack growth. This can be integrated to give

$$N_2 = \int_{l_c \sin \phi_{in}}^{l_f} \frac{dl}{C_2 \left(1.12\Delta\sigma_{app}\sqrt{\pi l}\right)^{m_2}} \quad (5.25)$$

$$= \frac{1}{C_2 \left(1.12\Delta\sigma_{app}\sqrt{\pi l}\right)^2} \ln \frac{l_f}{l_c \sin \phi_{in}}; \quad m_2 = 2 \quad (5.26)$$

$$= \frac{\left(\frac{2}{m_2-2}\right)}{C_2 \left(1.12\Delta\sigma_{app}\sqrt{\pi l}\right)^{m_2}} \left\{ (l_c \sin \phi_{in})^{(2-m_2)/2} - l_f^{(2-m_2)/2} \right\}; \quad m_2 \neq 2 \quad (5.27)$$

The total fretting fatigue life is then

$$N_T = N_1 + N_2 \quad (5.28)$$

### 5.3 Crack initiation in the absence of a singularity

Some geometries and contact conditions produce stresses without singular behavior. Recall from 1.3.4 the flat punch of length  $2a$  with a rounded corner of radius  $D/2$  with a contact length of  $2b$  upon loading by  $P$ . It should be noted that, for very small  $b-a$ , the stresses become very much like a those of a blunt crack. In that case the asymptotic stress fields are analogous to those described by Creager and Paris [85] where the notch root radius is  $b-a$ . A crack methodology could then be employed in the manner of Barsom and McNicol [86]. This methodology relates the stress field at the tip of a blunt crack to the stress intensity factor of a sharp crack of equal length. In the case of the rounded punch, this becomes[42]:

$$\sigma_{xx}^Q = 3.414 \frac{K_{II}}{\sqrt{\pi(b-a)}} \quad (5.29)$$

where  $K_{II}$  is the same as that of a sharp cornered punch. This stress is only accurate for small  $b-a$ , and must be added to the bulk stress and any other stress in the  $x$  direction. This would include an additional term from the pressure if the specimen is thin [42]. The stress at a given

	a (mm)	t (mm)	D (mm)	P (kN/m)	Q (kN/m)	b (mm)	$\sigma_{b, \max}$ (MPa)	R
H1	9.53	2	6.35	2600	350	9.65	350	0.5
H2	3.18	2	6.35	2600	260	3.35	260	0.5
H3	9.53	4	6.35	2100	550	9.63	275	0.5
H4	3.18	1	6.35	3500	138	3.39	275	0.5

Table 5.1: Conditions for experiments reported by Hutson et al.

	$K_{II}$ (MPa $\sqrt{m}$ )	$\sigma_{xx}^Q$ (MPa)	t/b	$\sigma_{xx}^P$ (MPa)	$\sigma_{xx}$ (MPa)
H1	2.01	346	0.21	391	735
H2	2.53	365	0.6	176	801
H3	3.16	584	0.42	429	902
H4	1.33	174	0.29	180	623

Table 5.2: Predictions for stresses in the x-direction for failure at  $1e7$  cycles.

fatigue life then becomes

$$\sigma_{xx} = \sigma_{xx}^Q + \sigma_{xx}^P + \sigma_{b, \max} \quad (5.30)$$

Table 5.2 gives model results using conditions listed in Table 5.1 from experiments by Hutson et al. with failure at  $10^7$  cycles [66]. For this fatigue life, the model shows an average value of 767 MPa at maximum load,  $R=0.5$ .

## 5.4 Validation with experimental data

Several sets of experimental data were selected from the literature. Most involved the same titanium alloy, Ti-6Al-4V, but several different contact geometries and loading conditions. Two sets of experimental results involved an aluminum alloy and both involved cylindrical geometries. Table 5.3 lists selected mechanical properties of the alloys examined.

Material	E (GPa)	$\nu$
Ti-6Al-4V	116	0.34
Al-4 wt% Cu	74	0.3

Table 5.3: Some mechanical properties of the alloys used in the selected fretting fatigue tests

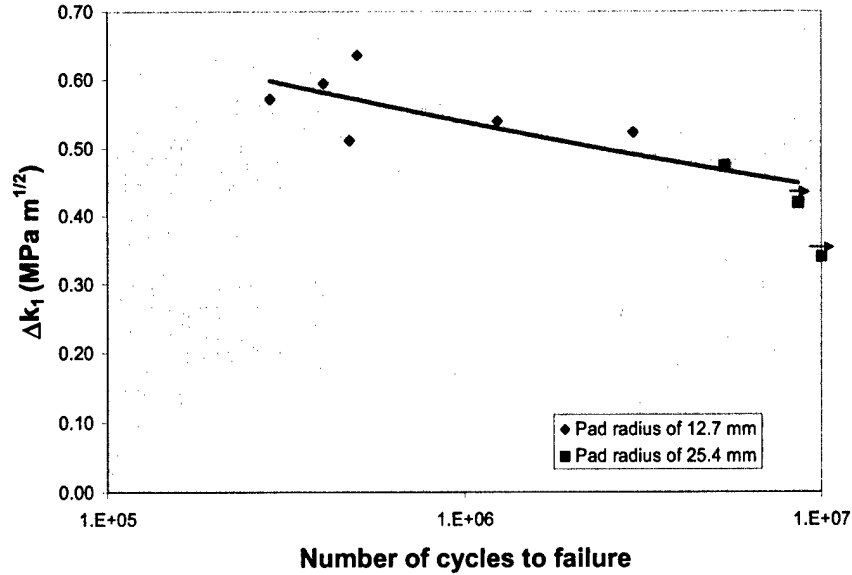


Figure 5-5:  $\Delta k_1$  is plotted versus number of cycles to failure for experiments where  $P$  is varied while  $Q$  is held fixed at 17 N and the maximum bulk stress is 300 MPa.

#### 5.4.1 Controlled sphere-on-flat experiments

Chapter 2 described in detail three series of sphere-on-flat Ti-6Al-4V fretting fatigue tests performed at MIT [37, 56]. These tests involved two pad radii, 12.7 mm (0.5 in) and 25.4 mm (1 in), with a variety of contact and bulk loads. These tests were all performed at  $R=-1$ . Of particular interest were the series of experiments where the contact conditions varied for a maximum bulk stress of 300 MPa.  $m_1, C_1$  were taken to be equal to  $m_2, C_2$  with  $m_1 = 3.17$  and  $C_1 = 1.5 \times 10^{-10}$  (for units of MPa  $\sqrt{m}$ , m). It should be noted that crack growth near the surface is modeled as two dimensions but the physical crack grows in three dimensions.

Recall that pad radius made a significant difference in the number of cycles to failure for a given  $Q/P$ . Figures 5-5 and 2-5 are plots of  $\Delta k_1$  versus number of cycles to failure. Since the bulk stress is the same for all of these controlled experiments, the life due to bulk propagation is approximately the same for all tests. Thus, the figures show the effect of varying the contact conditions including the pad radius on crack initiation and early crack growth.

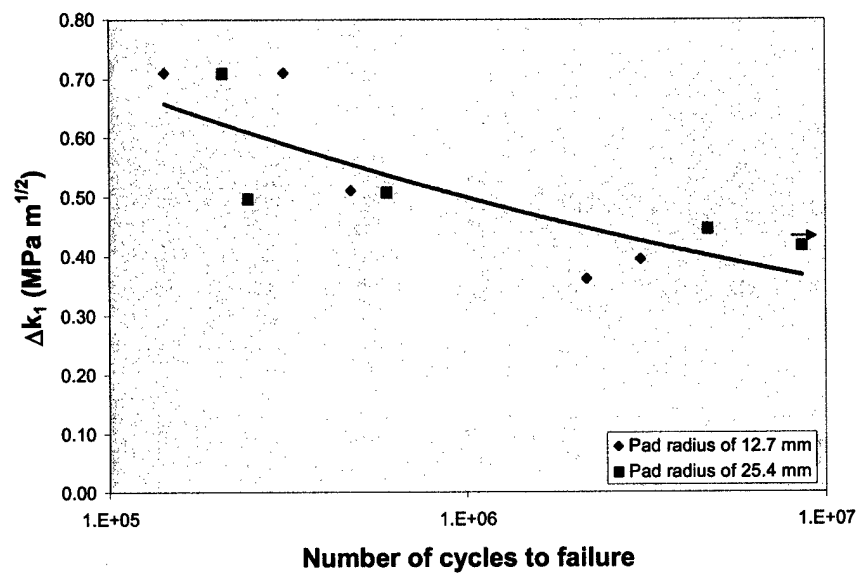


Figure 5-6:  $\Delta k_1$  is plotted versus number of cycles to failure for experiments where  $Q$  is varied while  $P$  is 50 N. Again, the maximum bulk stress is 300 MPa.

Description	R	$F_{\max}$ (kN)	$K_{I, \max}$ (MPa $\sqrt{m}$ )	$K_{II, \max}$ (MPa $\sqrt{m}$ )	$\phi_{in}$ ( $^{\circ}$ )	$l_c$ ( $\mu m$ )
Cylinder	0.1	19	0.21	8.44	71	16.8
Short flat	0.1	18.3	-28.3	14.2	40.3	44.9
Long flat	0.1	20.1	-11.9	6.7	42.6	37.3
Short flat	0.5	21.4	-32.2	26.2	40.6	41.8

Table 5.4: Stress intensity factors and crack orientation angles for the dovetail experiments.

Description	$\Delta K_{th}$ (MPa $\sqrt{m}$ )	$m_1$	$C_1$	$m_2$	$C_2$	$N_{f,act}$	$N_{f,pred}$
Cylinder	2.2	2	$2 \times 10^{-11}$	4.4	$6 \times 10^{-13}$	$10^6$	$9.7 \times 10^5$
Short flat	2.2	2	$2 \times 10^{-11}$	4.4	$6 \times 10^{-13}$	$10^6$	$8.9 \times 10^5$
Long flat	2.2	2	$2 \times 10^{-11}$	4.4	$6 \times 10^{-13}$	$10^6$	$9.7 \times 10^5$
Short flat	2.2	2	$2 \times 10^{-11}$	4.4	$6 \times 10^{-13}$	$10^6$	$8.5 \times 10^5$

Table 5.5: Fatigue life predictions for conditions used in each of the dovetail experiments. ro=runout

#### 5.4.2 Dovetail fretting fatigue tests

The dovetail tests were described in detail in Chapter 3. Values for the crack growth thresholds are available in [57, 87] while the Paris Law values  $m_2$  and  $C_2$  are found in [43].  $m_1$  and  $C_1$  were chosen to best fit experimental results. Stress-intensity factors and early crack parameters are given in Table 5.4 while fatigue information is contained in Table 5.5.

The assumption is made that the crack analogue can be extended to the short flat geometry and the long flat geometry with a taper. These geometries do not produce tractions that are square-root singular. Nonetheless, they are nearly singular or nearly square root singular, and the model will be applied. In the case of the long flat geometry, the notch analogue was also used to determine stresses at the edge of contact. The calculated stresses were well above yield and much larger than the stresses from Hutson. It was determined that  $b - a$  was very small for this long flat geometry and the associated contact loads. Thus, the contact mechanics for the long flat dovetail pads is more analogous to a crack than a notch. As will be shown, the model can still give reasonable results when extended to these geometries.

As for crack orientation, a section taken from one of the short flat tests at  $R=0.1$  revealed multiple cracks near the maximum edge of contact, see Figure 5-8. The predicted crack orientation angle is  $40.3^{\circ}$  with an  $l_c$  of  $44.3 \mu m$ . The measured angle is  $48.7^{\circ}$ , and  $l_c$  is 17.6 microns.



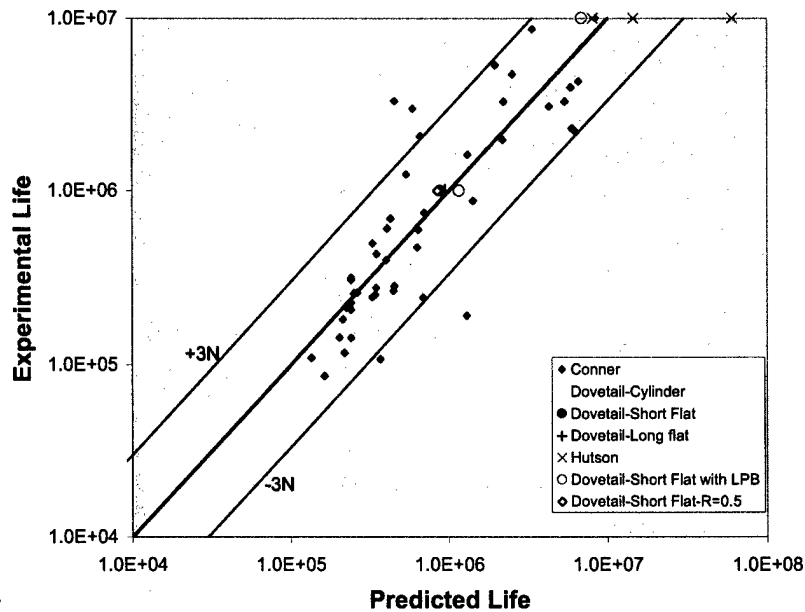


Figure 5-7: A plot comparing the experimental life versus the predicted life using the fracture mechanics methodology. Experiments from several geometries and fixtures are shown.

#### 5.4.3 Controlled flat-on-flat tests

The second set of data came from a series of fretting fatigue tests performed by Hutson, et al. [62], using specimens from the same forgings. The assumption is made that the crack analogue can be applied to these specimens. This is really only valid if  $b - a$  is very small. The contact geometry was flat-on-flat with varying specimen thicknesses and pad lengths. Figure 5-7 is a plot of actual fatigue life versus predicted life for several different sets of fretting fatigue tests. The results from the spherical contact tests by Conner are scattered about the line with slope of 1 where actual life equals predicted life, but the large number of tests will produce some experimental error. There is good agreement for the dovetail tests and all of the tests from Hutson et al.

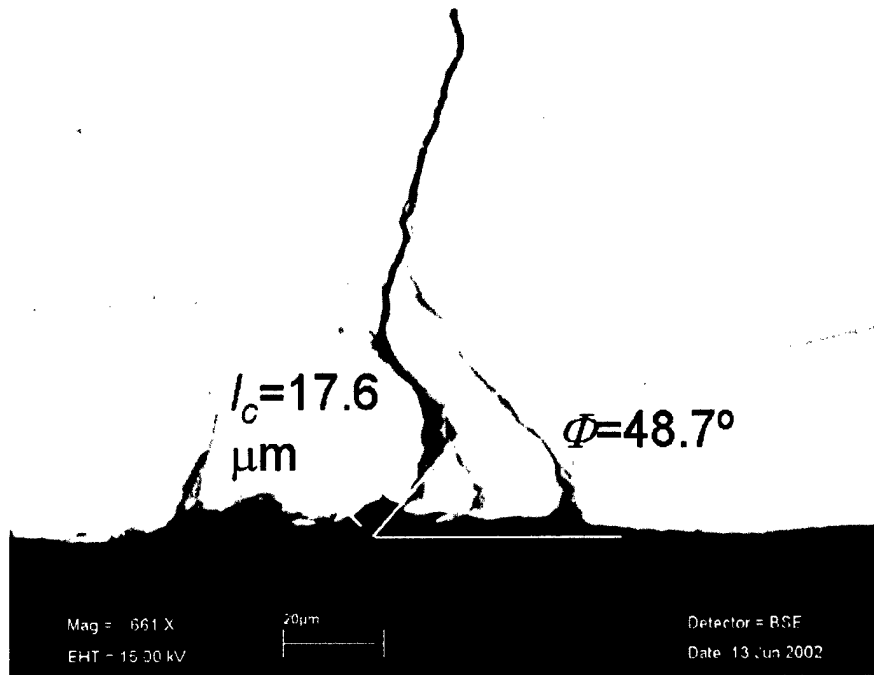


Figure 5-8: Multiple fretting fatigue cracks emerge from the contact surface (at the bottom of the micrograph). The dominant crack is oriented at a 48.7 degree angle to the surface and turns normal to the bulk stress by 17.6 microns.

#### 5.4.4 Cylindrical fretting fatigue of an aluminum alloy

Two sets of data were selected from the literature on fretting fatigue of Al wt%4 Cu alloys [38, 55]. The experiments were all cylinder on flat contact geometries and contained a wide range of contact and bulk loads as well as pad radii. Both sets of tests were performed at  $R=-1$ . The experiments in [55] demonstrated the postulated contact size effect which is an apparent increase in the number of cycles to failure as the contact width decreases.  $m_1, C_1$  were taken to be equal to  $m_2, C_2$  with  $m_1 = 3.387$  and  $C_1 = 6.62 \times 10^{-11}$  (for units of MPa  $\sqrt{\text{m}}$ , m) and are taken directly from [38].

The strength of the contact, as evidenced by the local stress intensity factor, has a direct impact on the fatigue life. Figure 5-9 shows the effect of the local mode I stress intensity factor on fretting fatigue life for a constant bulk stress.

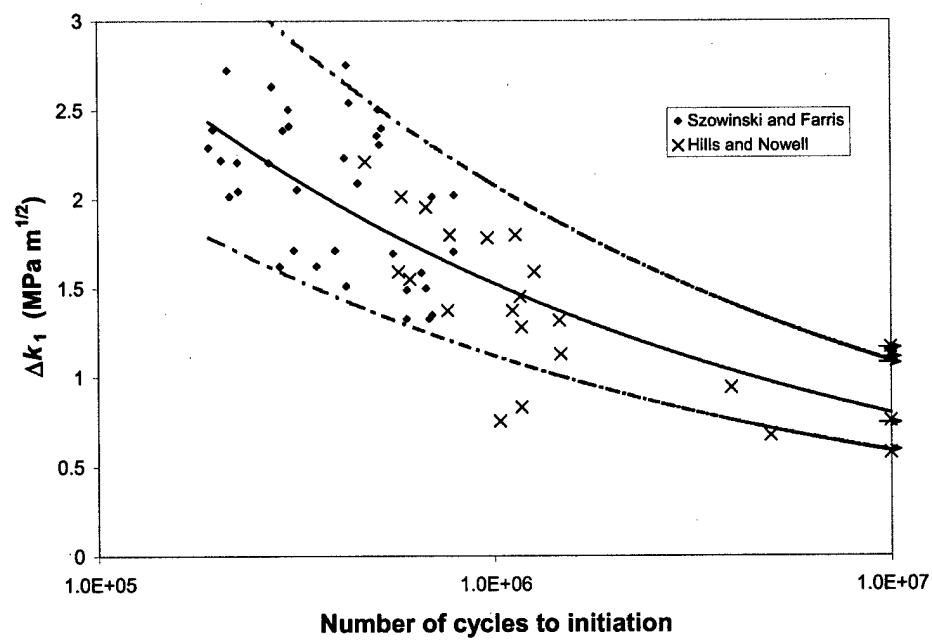


Figure 5-9:  $\Delta k_1$  versus number of cycles to failure for cylindrical contact (Al 4%wt Cu) and  $R=-1$ .

## 5.5 Limitations and assumptions of the model

The model, as presented here, assumes that the life can be estimated solely by accounting for propagation. An initiation regime is not considered. However, one could easily add the number of cycles required for initiation,  $N_o$ , to the total life if required for accurate life prediction. This would likely be based on analysis of experimental data; therefore,  $N_o$  would be empirical.

Another assumption is that linear elastic fracture mechanics is applicable. Employing the linear elastic fracture mechanics model requires conditions of small scale yielding near the region of interest. Any significant yielding will affect model predictions. The elastic limits of the models are discussed in detail in [40],[41] and [42].

The model currently requires knowledge of the point or line contact loads. As demonstrated with the dovetail specimens, it is difficult to determine these loads. However, using a numerical method can provide loads within some error.

## Chapter 6

# Palliatives

### 6.1 Introduction to surface engineering

To minimize contact damage, an engineer must follow certain guidelines. A summary of these guidelines is given by Ruiz and Nowell [60]:

- Reduce fretting damage by:
  - antifretting coatings
  - lower contact pressures
  - reduced slip
- Prevent crack growth by:
  - reducing the bulk tensile stress in the fretting region

There are several ways an engineer can achieve the desired result. An engineer can choose a new material that is more resistant to wear, thus reducing fretting damage. Another approach is to reduce fretting damage by using coating or surface treatment such as ion glazing. Or, the engineer could choose to introduce a compressive residual stress at the surface by peening or burnishing. This would reduce the composite tensile stress near the fretting region.

In engineering components that are likely to experience fretting, it is best to choose a material that is intrinsically resistant to fretting damage. It is also best to avoid the use of the same material for contacting surfaces if possible. Contacting surfaces of the same material are more likely to bond and increase wear damage [88]. It is of interest to note that titanium is the material of choice for fan and compressor blades and disks because of its specific strength

despite its poor fretting resistance. Often the blade and the disk are the same titanium alloy or similar alloys.

When materials replacement is not an option, as is the case for turbine components other methods of fretting resistance must be found. Coatings are one alternative option. There are several factors in the choice of coatings as a fretting palliative. The coating must provide the optimum combination of mechanical and tribological properties. These properties include the coefficient of friction, elastic properties and wear protection. A coating should be able to bond with the titanium, yet have very low solubility to reduce wear damage. Strong interfacial bonding results in a high wear rate. Tribologically compatible materials (i.e. materials that without strong interfacial bonding) have low mutual solid solubility. Ti has low mutual solubility (defined as solid solubility between 0.1 and 1%) with In, Cd, Zn, Cu, Au and Co. Mg will form a single liquid phase with Ti but has solid solubility below 0.1%. Pb, Sn, Al, Ag, W, Co, Cr, Ni, Fe, Pt, Zr, and Nb all have solid solubilities with Ti above 1% [89]. Two common coatings used in Ti compressor lugs are Cu-In-Ni [90] and aluminum bronze. The exact chemical composition varies with manufacturer and is generally proprietary information.

Hardened surfaces in general provide better wear resistance. This is the principle behind one of the earliest graded materials processes: carburization. In this process, the surface of a component is exposed to carbon at elevated temperatures. Diffusion occurs and carbon enters the surface and hardens it. The hardness approaches that of the interior as a function of the depth. The interior retains its ductility to withstand fatigue cracks. One of the difficulties with surface hardening is that it must be harder than any abrasive particles present. In the case of titanium, the oxides produced by fretting may be harder than any hardened variant of the alloy. However, a hardened surface may forestall the production of wear oxides.

Aside from tribological characteristics, the coating should meet certain mechanical parameters. The coefficient of friction should be reduced which would reduce the magnitude of the surface and subsurface stresses. In fact, it may shift the maximum stresses away from the surface and into the material [71]. Chivers and Gordelier have examined the effect of the coefficient of friction for coatings and made predictions on fretting fatigue performance [91].

Deposition of a graded surface can provide mechanical advantages against fretting. It has been shown by Suresh that a graded surface can better withstand normal contact damage than

an ungraded surface [92]. If the elastic modulus at the surface is lower than that of the bulk, the maximum stresses are shifted away from the surface. Development of Hertzian cone cracks did not occur in the graded material until almost twice the load of the monolithic material. It must be noted that this resistance to normal contact is valid for dovetail type fretting where the normal loads vary as well as the tangential loads.

It may be necessary to make a trade-off between wear resistance and mechanical performance in the choice of surface treatments. Often the wear resistance of a coating is related to its plastic properties, but the mechanical benefits may be related to its elastic properties.

Coatings may be combined with other surface treatments. A compressive residual stress could be introduced into the solid by a method of peening or burnishing. Then coatings could be applied. However, the method of application can affect the residual stresses. Thermal processes could relieve the residual stresses [90].

## 6.2 Coatings

### 6.2.1 Experiments

Early turbine engine designers turned to crude coatings as a form of fretting fatigue protection [93]. These coatings would rub away during the lifetime of the component in hopes of preventing crack initiation or unacceptable tolerances as a result of wear. Today, coatings are still widely used at the contact face of blade-disk attachments in the compressor region of gas turbine engines. As mentioned above, two common coatings are Cu-In-Ni and aluminum bronze. Aluminum bronze is now widely used in military applications but Cu-In-Ni coatings are still used in commercial engines [48].

The coating used was a commercial aluminum bronze coating. The powder composition is 89% Cu, 9% Al, 1.5% Fe and 0.5% miscellaneous (the remainder of the constituents are proprietary). The elastic modulus of the coating is 52 GPa and the hardness ranges from 161 to 191 VHN [94]. It should be noted that the coating properties may be significantly different from those of the bulk material because of changes to the microstructure due to the deposition process [95].

Dovetail titanium specimens received an aluminum bronze coating from Praxair Surface

Specimen #	Pad	R	f (Hz)	$L_f$	$L_{pr}$	$L_i$	n	$N_{f,n}$	Result
01-591	short flat	0.1	13	22.8	21.3	22.6	3	882,473	failure
01-469	short flat	0.1	13	22.5	22	22.5	1	980,210	failure
01-476	short flat	0.1	13	18.3	n/a	n/a	0	10,263,025	no failure

Table 6.1: Experimental results for fretting fatigue of Al-bronze coated specimens

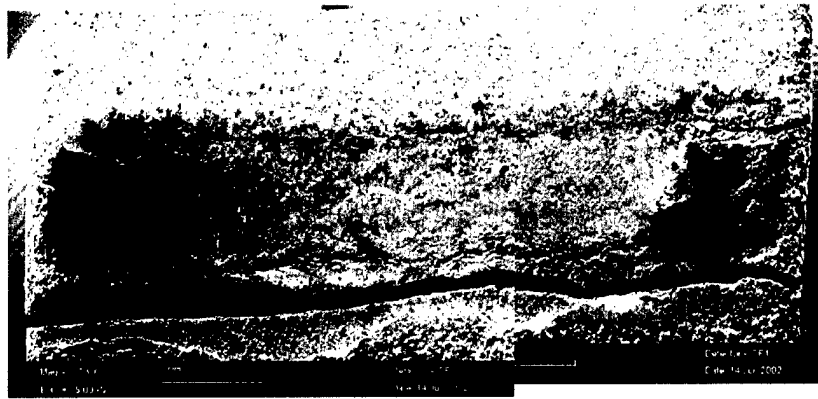


Figure 6-1: A low magnification composite SEM image of the fretting scar of a coated specimen after a crack has developed and propagated.

Coatings. The coating was applied by plasma spray. The coating thickness was 76 to 152 microns (3-6 mil) thick. Care was taken to stop the coating away from any radii (such as fillets) on the specimens to avoid interactions between thermal stress effects and the geometric residual stress concentrations. A Zygo NewView 5000 Surface Texture Analyzer was employed to determine the surface texture of the coating. This instrument uses white light interferometry to develop 2D profiles and 3D images of the surface topography. Some of the results are shown in Figure 6-2. The method determined a surface roughness root mean square (rms) value of 9.070 microns and an amplitude,  $R_a$ , value of 7.0 microns.

Fretting fatigue experiments were performed involving dovetail with an aluminum bronze coating and the results are contained in Table 6.1. The coating thickness was the same as above. The dovetail experiments showed that the load required for failure at  $10^6$  cycles was increased by 25% with the addition of the coating. When the same loads were applied to the coated specimens as those required to fail the uncoated specimens at  $10^6$  cycles then failure will not occur until at least  $10^7$  cycles.



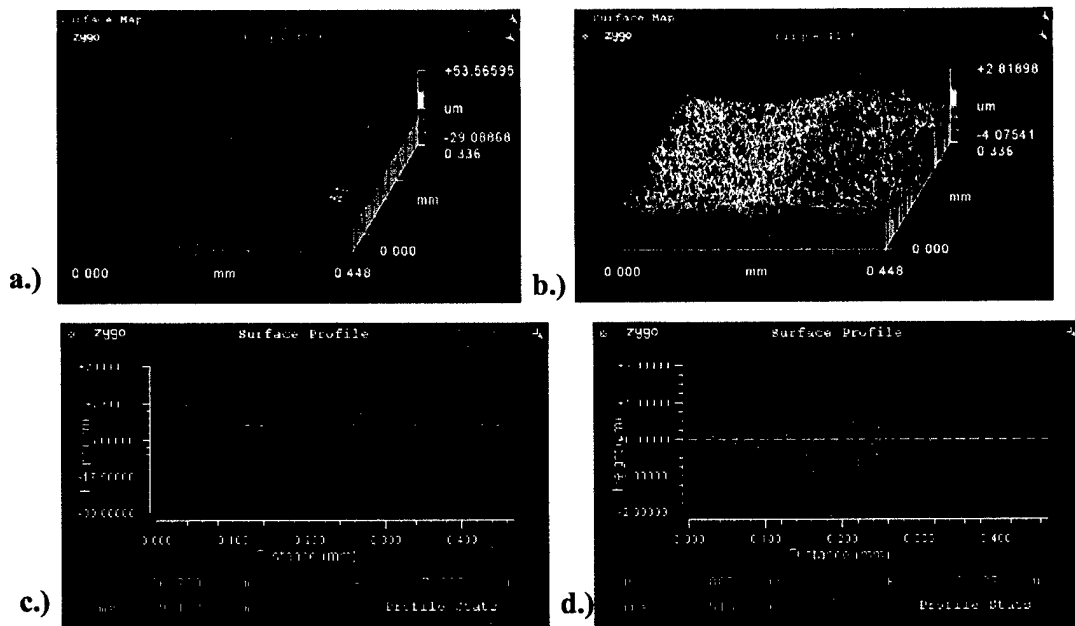


Figure 6-2: a.) A 3-D surface profile showing material removal to a depth of 29 microns in a small section of the slip zone from a coated specimen. b.) An uncoated specimen showing significantly less material removed in the slip region. c.) and d.) show 2-D surface profiles taken in a.) and b.) respectively.

Fretting fatigue cracks were observed to have nucleated near the maximum edge of contact, see Figure 6-1. Some delamination of the coating is seen near the location of the crack, but this damage most likely occurred after the formation and growth of the crack. Crack growth would change the compliance increasing the slip displacement resulting in increased wear damage at maximum load.

The coated dovetail specimens were examined after fretting fatigue using the Zygo and a Tencor P10 stylus profilometer. In general, the height of the region within the contact was less than that outside the contact. This is result of the compressive normal traction. The slip zone region formed a trench around the stick region because of wear in the slip zone. Asperities in the stick region were plastically deformed ("flattened") and the rms was reduced to 1.036 microns while the  $R_a$  was reduced to 1.020 microns. In the slip zone, the roughness was very similar to that of the baseline coating, but this is again a result of the wear due to slip.

### 6.3 Fracture mechanics modeling and coatings

Fracture mechanics can give insight into the ability of soft metallic coatings to improve fatigue life under conditions of fretting fatigue. It can be shown that the aluminum bronze coating provides protection if cracks initiate at the surface of the coating [96, 97]. Since the aluminum bronze coating is softer ( $\sigma_{y,coat} < \sigma_{y,sub}$ ) than the Ti-6Al-4V substrate, a crack that develops in the coating will resist propagation into the substrate assuming a well-bonded coating. The crack would likely arrest or require an increase in the far-field stresses to propagate into the substrate.

Hutchinson and Suo [98] developed a complex stress-intensity factor,  $K$ , for an edge crack located at one edge of a coating of thickness  $h$  with  $E_c$  and  $\nu_c$  sandwiched between two layers with the same properties,  $E_s$  and  $\nu_s$ .

$$K = h^{-i\epsilon} \left( \frac{1-A}{1-\beta^2} \right) (K_I + iK_{II}) e^{i\omega} \quad (6.1)$$

$$\epsilon = \frac{1}{2\pi} \ln \left( \frac{1-\beta}{1+\beta} \right) \quad (6.2)$$

where  $A$  and  $\beta$  are Dundurs parameters,  $\omega$  is the complex phase angle shift resulting from moduli dissimilarity and plotted in [98], and  $K_I$  and  $K_{II}$  are from an edge crack in a monolith with properties  $E_s$  and  $\nu_s$ . One can use the stress-intensity factors, found with the help of FEM, from the crack analogue as inputs for  $K_I$  and  $K_{II}$  to determine  $K$ , see Figure 6-3. Since  $K$  is complex, the strength of  $K$  can be determined by examining the norm of  $K$ , that is  $K$  times its conjugate. As shown in Table 6.2, addition of the coating results in a reduction in the strength of  $K$  at baseline loads and experiments show no failure. A substantial increase in the strength of  $K$  is required for failure. This may be because of plasticity near the surface as evidenced in substantial wear and indentation by the contact pad shown in the Zygo measurements. The plasticity could “shield” the region of the singularity and inhibit the initiation of fretting cracks.

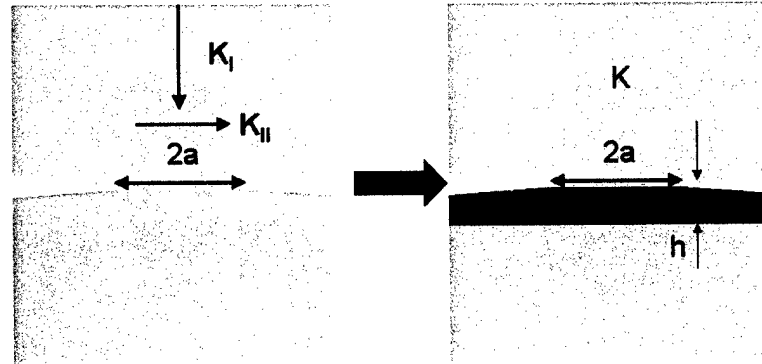


Figure 6-3: Transitioning the crack analogue to a coated body with coating thickness  $h$  via the complex stress intensity factor  $K$ .

Head	$F_{\max}$ (kN)	$N_f$	$E_c$ (GPa)	$E_s$	$h$ ( $\mu\text{m}$ )	$\omega$ (deg)	$K_I$	$K_{II}$	$\ K\ $
Uncoated baseline	18.3	$10^6$	116	116	157	0	-28.29	14.22	1003
Coated at baseline loads	18.3	n/f	50	116	157	-4.9	-28.29	14.22	967
Coated, failure $N_f=10^6$	22.6	$10^6$	50	116	157	-4.9	-43.81	8.69	1553

Table 6.2: Complex  $K$  for the experimental conditions listed above. It is assumed that the Poisson's ratio of the substrate and the coating are equal. n/f means no failure.

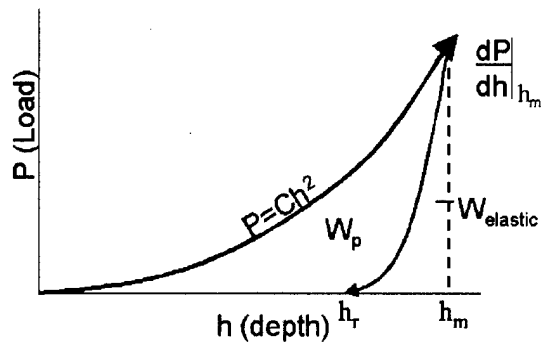


Figure 6-4: A schematic of a P-h curve.

### 6.3.1 Depth sensing indentation of contact fatigue resistant soft-metallic coatings

#### Introduction to property extrapolation from depth sensing indentation

Sharp indentation to depths on the nano or micrometer scale can be useful in determining mechanical properties of thin films. In order to do this, one must be able to measure the applied normal load,  $P$ , and the depth of indentation,  $h$ . This is not a trivial problem. As a result of deposition, the microstructure of the coating (and therefore its properties) may be vastly different than that of the starting material [95].

In contact fatigue, a coating can provide a variety of benefits including wear resistance, reduced coefficient of friction, and beneficial relocation of surface stresses. While wear resistance and coefficient of friction can be measured in sliding tests such as the pin-on-disc test, the mechanical properties of the coating can be difficult to determine. Depth sensing sharp indentation has several advantages including the following. First, it is a non-destructive method. The indentation depth can be only a few microns or nanometers in depth. Second, it evaluates the mechanical properties of the coating in the absence of friction. In other words, the effects of the elastic and plastic properties can be separated from stress effects due to a reduction in the coefficient of friction. Finally, small volume indentation allows examination of the properties of the coating apart from that of the substrate.

While depth sensing indentation is a recent development indentation itself has been used as a tool to determine the hardness of materials for many years. Determining material properties from indentation is computationally intensive. One can determine the  $P-h$  curve if  $E$ ,  $\nu$ ,  $n$  and  $\sigma_y$  are known. This is defined as the forward problem. The reverse problem obtains the elasto-plastic properties from the  $P-h$  curve. It is the solution of the reverse problem that is of interest to this research [99].

There are potential applications for indentation of contact fatigue resistant coatings. Indentation can be used as a quality assurance tool for coatings in production. Coated components can be indented after application of the coating. Assuming satisfactory results from indentation, these components can be returned to service since the indentation is non-destructive. There are limitations that must be resolved before indentation can be used as a quality assurance tool. The accuracy of the indentation results improves if the surface is flat. In general, plasma sprayed coatings are very rough and must be polished before indentation.

Indentation can also quickly determine the elasto-plastic properties of a coating or functionally graded material that is being developed for used as a contact fatigue palliative. Again, indentation would separate the mechanical properties from friction effects.

## Experiments

A Ti-6Al-4V forging was sectioned into two specimens for indentation. One specimen was coated with the aluminum bronze coating. Prior to grinding and polishing, the coating thickness was 157 microns. Both specimens were first prepared by grinding with 600, 800, 2400 and 4000 grit SiC paper then mechanical polishing using 3  $\mu\text{m}$  diamond suspension, 0.5  $\mu\text{m}$  diamond paste and 0.05  $\mu\text{m}$  Mastermet. The resulting finish was highly reflective. Observation using an optical microscope revealed substantial reduction in surface roughness, and the coating thickness after polishing was 94  $\mu\text{m}$ . However, some small pits still remained after polishing and provided a source of experimental error. The coating was also shown to be 0.5 to 1% porous as a result of plasma spray deposition in air leading to splatting. This would provide a source of experimental error.

The depth of indentation must be chosen to be small enough to prevent interference from the substrate. In order to find the limit of indentation depth, an elasto-plastic axisymmetric finite

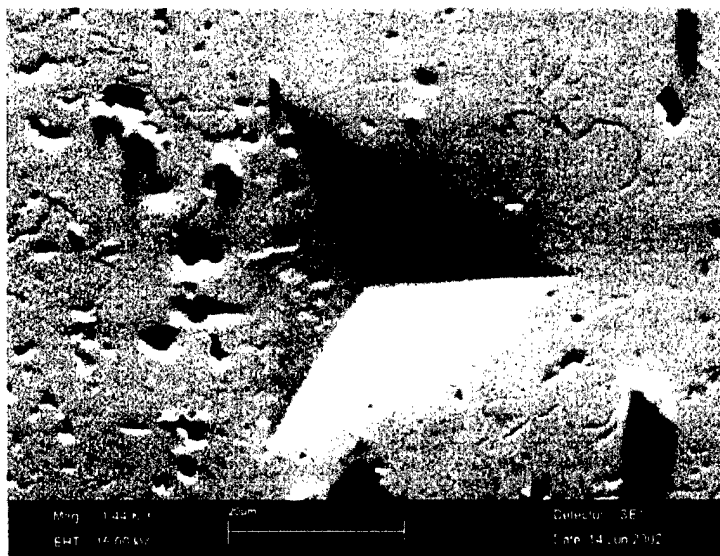


Figure 6-5: A micrograph looking down into a indentation into the coating. Note the small dents and particles on the surface.

element analysis of a sharp rigid indenter was performed based on four variations of the film mechanical properties as supplied by the commercial vendor. The numerical analysis showed that indentation could be performed up to 9 microns into the coating without interference from the substrate.

A diamond Berkovich tip was used in each indentation. For the coated specimen, two indentation depths were chosen: 5-6 microns and 8-9 microns. The uncoated specimen was indented only to 8-9 microns.

The experiments gave values within 20% of the properties of Ti-6Al-4V but gave values  $\pm 150\%$  of the expected coating properties and the known properties of the Al7075 standard. Thus, results could not be obtained for the coating. There are several possible reasons for this. This may have been because of the bluntness of the diamond Berkovich indenter tip possibly as a result of previous testing. Or, plasticity in the coating and the aluminum was so extensive that it changed the compliance as the indenter was pushed into the material. The plastic zone became itself an indenter pushing ahead of the tip. Evidence of such plasticity can be seen in Zygo measurements where material "sink-in" is observed around the edge of the indentation.

## Summary

While the theory for instrumented indentation is extensive, further work must be done before it can be used for practical applications on this scale. If successful, such indentation will yield mechanical properties of fretting fatigue resistant coatings. This would be a boost to fretting fatigue physically based life prediction models which might otherwise not use accurate material properties.

## 6.4 Low plasticity burnishing: compressive residual stress

### 6.4.1 Background

One method to combat the contact fatigue is to introduce a compressive residual stress. Shot peening is a common method of treating components by bouncing shot off the material surface. A compressive residual stress results as the elastic subsurface material is constrained by plastically deformed material at the impact site. However, the depth of compression from the shot peening is only on the order of fractions of millimeters and leaves the maximum residual stress at the surface. The surface is roughened by the shot peening and this may provide a beneficial effect during contact fatigue by reducing adhesive forces.

It is known that the beneficial effects of shot peening on contact fatigue can be completely removed by thermal or mechanical effects. In general, residual stresses can be removed during the process of thermal annealing. This annealing can even occur during the application of coatings. Koul et al. [90] demonstrated that the application of wear coatings by plasma spray may completely relieve the compressive residual stresses at the surface resulting in fretting performance that is even worse than the absence of peening and coating. Shepard et al. showed that residual stresses accompanied by high magnitudes of cold work at the surface (which results from both shot peening and laser shock peening) are relieved at elevated temperatures and serve no benefit during fatigue [100]. Kirkpatrick provided a theoretical framework for determining the depth at which compressive residual stresses are relieved by the high compressive stresses developed during contact [44].

Low plasticity burnishing (LPB) has several advantages. LPB produces a zone of compressive residual stresses that can have approximately the same magnitude and depth as laser shock

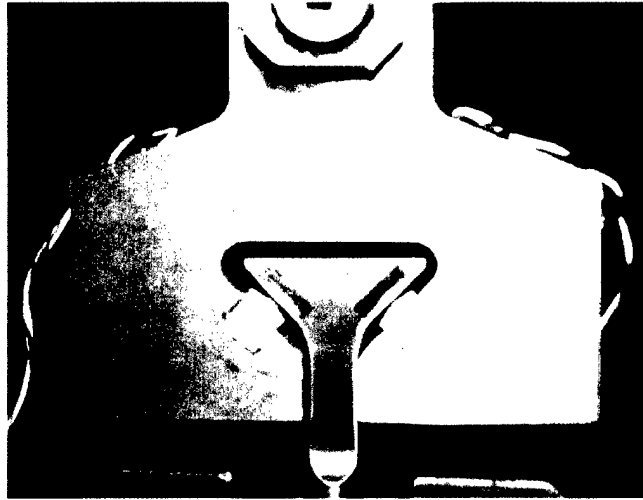


Figure 6-6: A photograph of an LPB treated specimen in the dovetail fixture. Notice the polished appearance of the specimen regions near the contact pad. This is a result of the contact pressure from the rolling sphere.

peening with much less cold work at the surface. There is little roughness associated with LPB. In fact, LPB produces a near-polished surface. While the absence of roughness may increase adhesion, the experimental results below show that it is clearly not detrimental. Indeed, the smooth surface may assist adhesion of wear-resistant coatings.

#### 6.4.2 Experiments

Three Ti-6Al-4V specimens were treated with LPB on the contact region and on the side of the specimen perpendicular to the contact region. The original specimen finish after machining had roughness (RMS) of 8. After LPB, the machining grooves were removed and the finish was very smooth.

Both the fretting pads and specimens were Ti-6Al-4V. The pad geometry was a 1.016 mm (40 mil) flat with an 11 degree taper. Typically, the contact region of the blade-disk attachment can be approximated experimentally with a flat pad with rounded corners or a taper. A photograph of an LPB treated specimen held in the fretting fixture can be seen in Figure 6-6.

For all of the tests involving LPB-treated specimens, the test frequency was 13 Hz. As shown in Table 6.3 without LPB, experiments conducted with a load ratio of 0.1 demonstrate



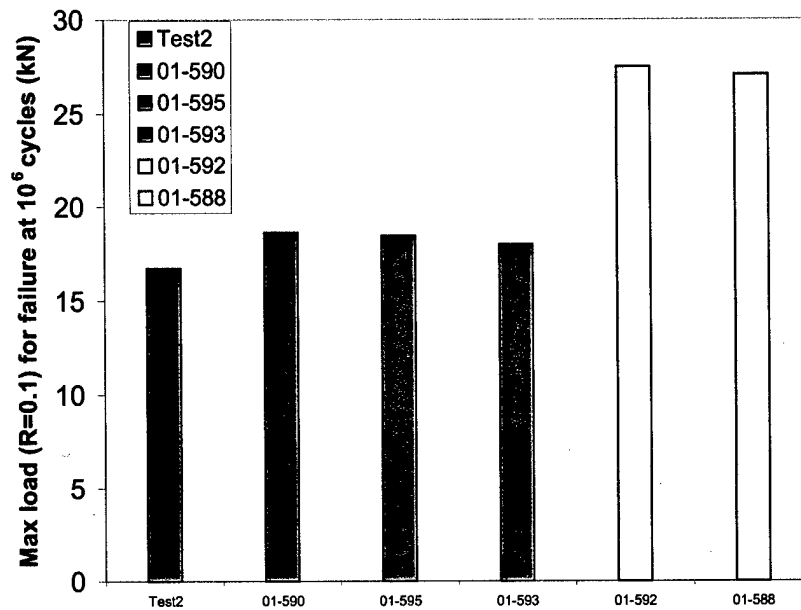


Figure 6-7: The maximum load for failure at  $10^6$  cycles ( $R=0.1$ ) for baseline specimens and LPB treated specimens.

Specimen #	Pad	R	f (Hz)	$L_f$	$L_{pr}$	$L_i$	n	$N_{f,n}$	Result
01-592	short flat	0.1	13	27.5	25	27.5	3	997,487	failure
01-588	short flat	0.1	13	28	27	27.1	2	68,377	failure
01-589	short flat	0.1	13	18.3	n/a	n/a	0	11,682,700	no failure

Table 6.3: Experimental results for fretting fatigue of LPB treated specimens

an average maximum load of 18.3 kN at  $10^6$  cycles for this geometry and this material. Two specimens treated with LPB were also step-tested at a load ratio of 0.1. These specimens failed after  $10^6$  cycles at an average maximum load of 27.3 kN. This was a 49.2% improvement in the maximum load that can be sustained with failure at  $10^6$  cycles (6-7).

A third specimen was tested at a load ratio of 0.1 with a maximum load of 18.3 kN. These loads represent the average baseline loading conditions for failure at  $10^6$  cycles. Thus, this test determines the improvement in the fretting fatigue life at a given load. After 11,682,700 cycles the test was stopped without any visible cracks, an improvement of at least an order of magnitude in fatigue life over the baseline specimens (Figure 6-8).

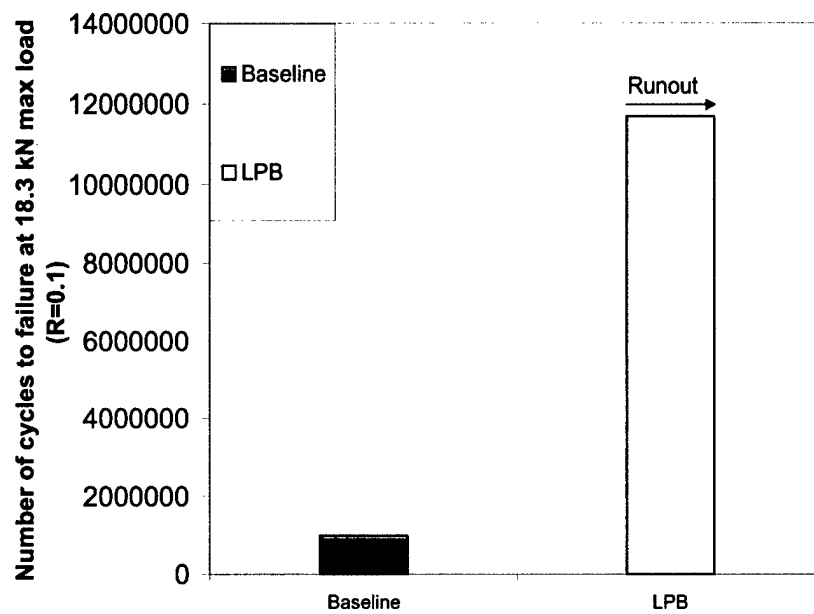


Figure 6-8: The number of cycles to failure for an 18.3 kN maximum load ( $R=0.1$ ). Significant improvement for the LPB treated specimen.

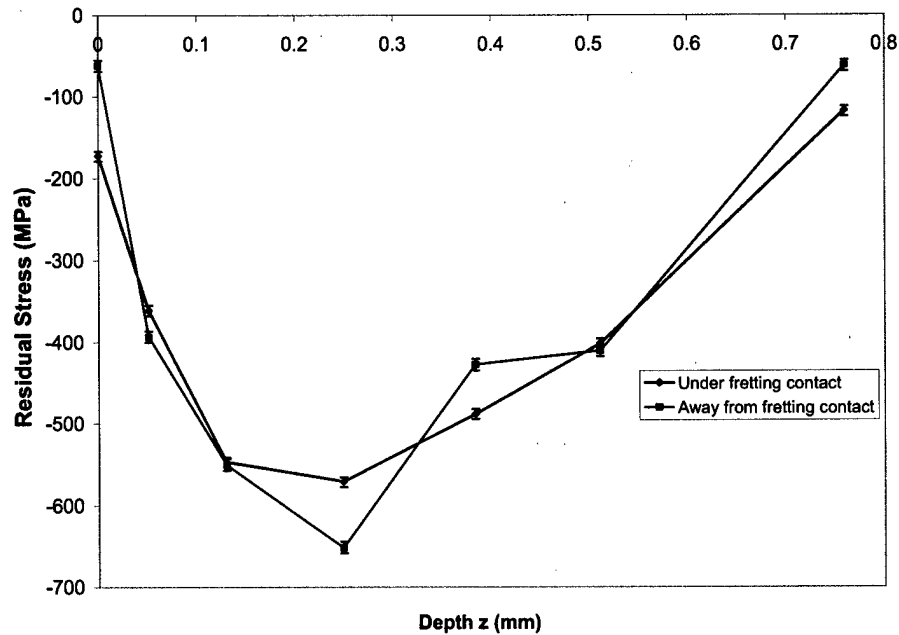


Figure 6-9: X-ray diffraction measurements of the burnishing induced residual stresses under the fretting fatigue scar and away from.

#### 6.4.3 Residual stress and cold work distributions

Lambda Research of Cincinnati, Ohio, performed X-ray diffraction (XRD) on specimen #01-589 at two locations on the specimen. The first was under the fretting region and the second away from the fretting region. Details of the methodology of XRD used to determine residual stresses and cold work are given in [101],[102] and [103]. Unlike shot peening, the most compressive residual stresses are not found at the surface but about 200 microns below the surface. The magnitude of compressive residual stress at the surface actually increases after fretting. The % cold work is relatively low compared to other methods [100], but it is higher in the fretting region. This is because of the cold work from wear damage and localized plasticity.

It should be noted that the thickness of the specimen and the size of the application patch affect the distribution of residual stresses. The stress state in a body must satisfy equilibrium. In the dovetail specimen, the residual stresses near the surface are very compressive. However, some region of the specimen will have a small, but non-zero tensile residual stress in order to

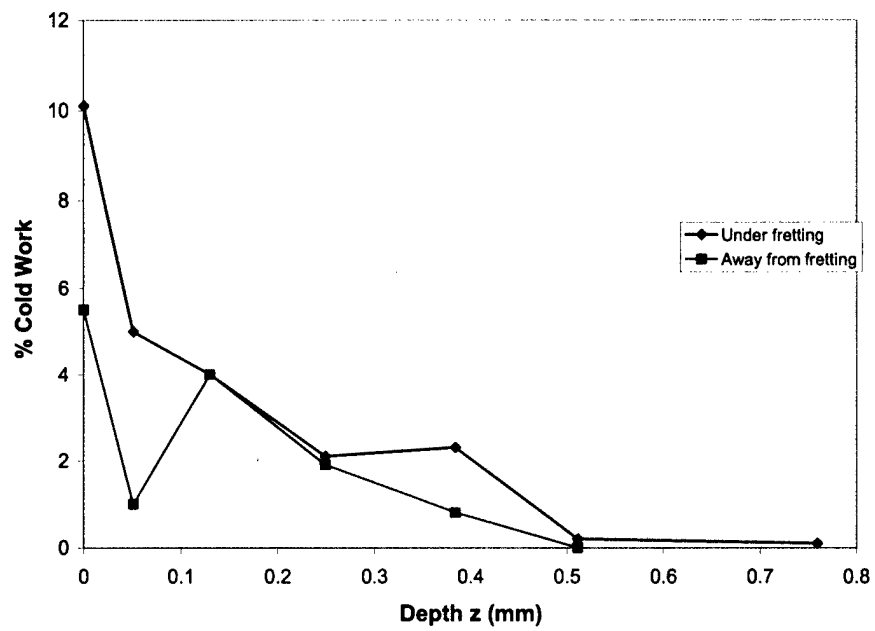


Figure 6-10: X-ray diffraction measurements of the burnishing induced % cold work distribution under the fretting fatigue scar and away from.

satisfy equilibrium. However, if a specimen is too thin, the residual stresses may be partially or completely relieved, as the specimen will deform by bending or stretching. The dovetail specimens are quite thick, but thin bar specimens such as those used in the MIT fretting rig may not be suitable for testing of LPB.

#### 6.4.4 Effect on crack initiation

A review of the literature shows that the peening treatment has little effect on crack initiation. In general, micrographs of regions near the contact edge from specimens that have been surface-treated show the initiation of many cracks, most having arrested [104]. Some treatments such as shot peening result in surface damage such as pits or folding defects that can form initiation sites [105]. Shot peening and laser shock peening can produce large percentages of cold work at the surface which could provide energy for crack initiation [100]. In these cases, the fatigue life is reduced even further than the baseline specimen if the residual stresses are thermally relieved. Such surface damage is not seen with low plasticity burnishing which leaves a highly polished surface.

Surface treatments that introduce compressive residual stresses do reduce the mean stress but they do not change  $\Delta\sigma$ . However, the reduction in residual stress inhibits the nucleation of an initiated crack to propagate. This is especially true in fretting fatigue where there are conditions of steep stress gradients as well as gradients in the mean stress. Since the definition of crack *nucleation* and crack *initiation* are often unclear, effects of residual stress on crack nucleation may be incorrectly said to impact initiation.

#### 6.4.5 Effect on crack propagation

Reduction of the mean stress by LPB reduces the magnitude of the cyclic tensile stresses required for mode I crack opening. Here,  $\Delta K_I$  is calculated for an edge crack in a stress gradient using a program developed by Dr. Reji John at Air Force Research Laboratory and weight-functions by Tada et al. [106]. The program models a crack located at the maximum edge of contact, where the maximum edge of contact refers to the edge of contact when the bulk load is maximum, and is oriented normal to the surface. Finite element modeling provides the contact stress field inputs and the mean stress is superimposed.

Description	R	F <sub>max</sub> (kN)	K <sub>I, max</sub> (MPa√m)	K <sub>II, max</sub> (MPa√m)	φ <sub>in</sub> (°)	l <sub>c</sub> (μm)
Short flat, LPB	0.1	18.3	-28.3	14.2	40.3	798
Short flat, LPB	0.1	27.3	-37.2	26.2	47	1153

Table 6.4: Stress intensity factors and crack orientation angles for the LPB treated dovetail experiments.

Description	ΔK <sub>th</sub> (MPa√m)	m <sub>1</sub>	C <sub>1</sub>	m <sub>2</sub>	C <sub>2</sub>	N <sub>f,act</sub>	N <sub>f,pred</sub>
Short flat, LPB	2.2	2	1×10 <sup>-12</sup>	4.4	6×10 <sup>-13</sup>	ro	6.8×10 <sup>6</sup>
Short flat, LPB	2.2	2	1×10 <sup>-12</sup>	4.4	6×10 <sup>-13</sup>	10 <sup>6</sup>	1.2×10 <sup>6</sup>

Table 6.5: Fatigue life predictions for conditions used in each of the LPB dovetail experiments. ro=runout

A load of 18.3 kN applied at a load ratio of 0.1 is required for failure at 10<sup>6</sup> cycles if a specimen is untreated. A specimen treated with LPB will not fail after 10<sup>7</sup> cycles with the same loading conditions. Subsequently, if the load is increased to 27.3 kN, the specimen will indeed fail. Plots of ΔK<sub>I</sub> for these three conditions agree quite well with observations. The LPB-treated specimen may initiate cracks under baseline loading conditions, but they will most certainly not propagate. However, a significant increase in load is required to cause and maintain crack propagation.

One can use the fracture mechanics-based model described in Chapter 4 to determine the fretting fatigue life of a component treated with LPB. This was done for the conditions of the dovetail test. The assumption is made that all of the effect of the residual stress occurs in the first regime of crack growth, N<sub>1</sub>. The reduction in the rate of crack growth changes m<sub>1</sub> and C<sub>1</sub> used in the Paris Law. The tensile cyclic applied bulk stress, used in the determination of l<sub>c</sub>, is also reduced as

$$\Delta\sigma = \sigma_{app,max} - \sigma_{app,min} + \sigma_{residual} \geq 0 \quad (6.3)$$

with σ<sub>residual</sub> being negative as the residual stresses at the surface are compressive. From XRD measurements, the residual stress at the surface is -176 MPa and from FEA the maximum and minimum bulk stresses are 220 and 3 MPa, respectively. Thus, Δσ is approximately 40 MPa. As shown in Tables 6.4 and 6.5, the fatigue life at baseline loads is significantly improved by the LPB treatment and failure at 27.3 kN and R=0.1 is near 10<sup>6</sup> cycles.

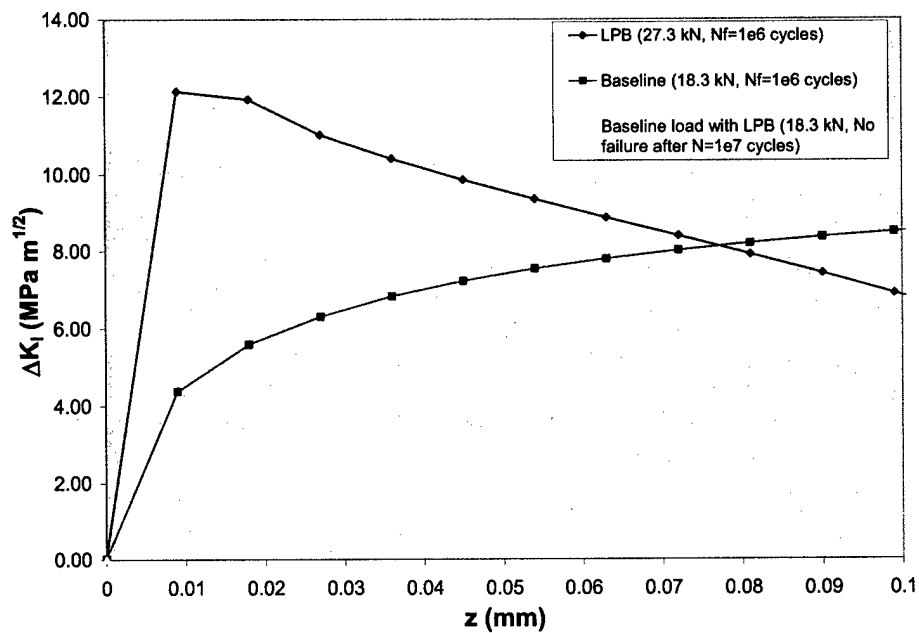


Figure 6-11: A plot showing the stress intensity factor as a function of crack length for a crack at the edge of contact and normal to the surface. 3 different test conditions are considered corresponding to an untreated specimen at baseline loads, a specimen treated with LPB at baseline loads, and specimen treated with LPB with a 50% increase in maximum load resulting in failure at  $10^6$  cycles.

#### 6.4.6 Summary

Low plasticity burnishing is an effective palliative against fretting fatigue. The compressive residual stresses inhibit crack nucleation and slow or arrest the growth of fretting fatigue cracks. An increase of 50% of the baseline  $R=0.1$  loads is required to propagate cracks to failure at  $10^6$  cycles.



## Chapter 7

# Conclusions

### 7.1 Summary of work

#### 7.1.1 Experiments

A fretting fatigue fixture developed at MIT is able to control and measure major fretting fatigue variables. Fretting fatigue experiments using a sphere-on-flat geometry examined a wide range of contact loading conditions and bulk stresses. Fretting fatigue life can be reduced by the following: an increase in bulk stress, a decrease in spherical pad radius for a given contact load, an increase in the tangential load provided that sliding does not occur, or a decrease in the tangential load.

A new fretting fatigue fixture was developed and validated. This dovetail fixture allows the study of more complicated and realistic contact geometries while still being able to examine less complicated ones such as cylinders. The thick specimens enable easy examination of palliatives without deforming the specimen from thermal or mechanical loading, as is often seen in peening or coating thinner specimens. The most damaging geometry was the short flat pad which only required 18.3 kN to cause failure at  $10^6$  cycles.

Micro-damage from fretting fatigue was observed from dovetail specimens and pads as well as specimens from sphere-on-flat tests [43, 56] and flat-on-flat tests by Hutson [62, 66]. In general (i.e. across the various geometries and fixtures), Ti-6Al-4V cracks were observed to be wedge shaped and often filled with wear oxides that flowed in from the slip regions. Multiple

cracks would initiate but only one crack would dominate. A final general observation was that cracks fell into two categories. The Type I crack was a shallow crack oriented at 15-30 degrees with the surface. The Type II crack was oriented at 45-80 degrees.

The higher loads required to cause cracks in shot peened specimens also resulted in near surface plasticity. It was observed that cracks developed in large wear regions where a unique type of damage, one not seen in untreated specimens, was micro-notching. Micro-notches serve as crack initiation sites. This examination led to a greater understanding of what damage results in fretting fatigue of Ti-6Al-4V with some implications on their impact on life prediction methods.

Experiments on two types of palliatives were performed. Experiments were performed on a new palliative for fretting fatigue resistance called low plasticity burnishing (LPB). LPB is a method of introducing a compressive residual stress via a hard roller. The second palliative was a soft metallic coating made of aluminum bronze. The soft coating reduced the coefficient of friction to 0.2 and had half the Young's modulus of the Ti-6Al-4V substrate.

Both palliatives showed life improvement at baseline loads. The coated specimen required a 25% increase in load ( $R=0.1$ ) to cause failure at  $10^6$  cycles while the LPB treated specimens required a 50% increase in load. The compressive residual stresses inhibited the growth of fretting fatigue cracks and required a significant increase in applied load in order for cracks to propagate. The coating reduced the coefficient of friction, thereby reducing stresses. It also served as wear protection.

### 7.1.2 Analysis

An elastic finite element model of the dovetail fretting fatigue apparatus was developed. A method of verifying the accuracy of the FEM was to compare nodal strains to the strains measured by the strain gauge located across from the stress concentrator in the dovetail slot. The loads applied to the contact region could be determined using the finite element model. The model also clarified the evolution of the surface tractions during a loading cycle.

The use of fracture mechanics was explored based on the foundation of the crack analogue [40] and associated models [41, 42]. Reasonable agreement was reached between experiments and predicted life for the new dovetail fixture and several other fixtures including the well

controlled MIT fixture. For each of the controlled sphere-on-flat fretting fatigue test series, modifying a contact load or geometry directly impacted the local stress-intensity factor as determined from the model. It is of interest to note that some of the geometries such as the short flat punch with taper differed from the exact geometries in the model, but reasonable predictions were still achieved.

The predicted life from the fracture mechanics model was compared to the experimental life for the low plasticity burnished specimens. It was assumed that the entire effect of the LPB could be captured in the early crack growth stage,  $N_1$ . The compressive residual stress would slow down the crack growth. Reasonable results were obtained when compared with actual fretting fatigue life.

## **7.2 New directions for contact fatigue research**

### **7.2.1 Contact fatigue**

There is much room for future work in contact fatigue. While this research focused extensively on fretting fatigue, future research could be directed toward rolling and sliding fatigue. It would be of interest to determine to what extent it is possible to extend fracture mechanics to other forms of contact fatigue. Development of new contact fatigue fixtures may be required to control and instrument variables during these tests.

There is still a need for understanding friction and its impact on contact fatigue. There is evidence in the literature that friction is not well understood and influences the near surface damage [66, 107]. While frictional values in metals are often cited to be 0.5 or lower, local values of friction may be more like 0.95 [37] or 1.5 [107]. Greater understanding of the influence of cyclic loading on friction may be gained by sensitive friction measurements made using nano and micro indenters with the capability to perform scratch tests instrumented with tangential load cells. Repetitive measurements of the evolution of friction could be made at previously unavailable cycles and length-scales. Fundamental studies of slip, friction and cyclic loading could be obtained by scratch tests of single crystal materials with various orientations.

### 7.2.2 Palliatives

Besides other forms of contact fatigue, research should also be directed to palliatives. Elastically or plastically graded coatings could improve contact fatigue resistance [108]. Hard coatings may delaminate if applied to a surface that experiences large bulk strains. Graded coatings may resist delamination since there is no abrupt change in the mechanical properties. Elastically graded soft coatings could be designed to transfer peak stresses away from the surface. Cracking in monolithic hard coatings can propagate into the substrate, but graded hard coatings may resist propagation. There has been some theoretical research on cracking of fretted functionally graded coatings, see [109], but little experimentation. For further discussion on the influence of graded coatings and resistance to contact fatigue see [92].

On the topic of monolithic coatings, new approaches could be developed for further application of fracture mechanics to coated materials beyond the work covered here. In particular, the role of plasticity must be considered [110]. Nanostructured coatings may give improved wear and fatigue resistance assuming that they can be processed and can effectively bond to the substrate.

Liquid lubricants were not addressed in this paper. They are a common palliative used on components affected by rolling fatigue. However, such lubricants can easily interact with cracks and influence life prediction.

# Bibliography

- [1] R B. Waterhouse and T C. Lindley. *Fretting Fatigue*, volume 18 of *European Structural Integrity Society*. Mechanical Engineering Publication Limited, London, 1994.
- [2] S Suresh. *Fatigue of Materials*. Cambridge University Press, Cambridge, 1998.
- [3] K Nakazawa, M Sumita, and N Maruyama. Fatigue and fretting fatigue of austenitic and ferritic stainless steels in pseudo-body fluid. *Journal of the Japan Institute of Metals*, 63 (12):1600–1608, 1999.
- [4] M Niinomi. Recent titanium R&D for biomedical applications in Japan. *JOM*, 51(6): 32–34, 1999.
- [5] E M. Eden, W N. Rose, and F L. Cunningham. The endurance of metals. *Proceedings of the Institution of Mechanical Engineers*, 4:834–974, 1911.
- [6] G A. Tomlinson. The rusting of steel surfaces in contact. *Proceedings of the Royal Society, London, Series A*, 115:472–483, 1927.
- [7] E J. Warlow-Davies. Fretting corrosion and fatigue strength: Brief results of preliminary experiments. *Proceedings of the Institution of Mechanical Engineers*, 146:32, 1941.
- [8] J Dundurs and M S. Lee. Stress concentration at a sharp edge in contact problems. *Journal of elasticity*, 2(2):109–112, June 1972.
- [9] H Hertz. On the contact of elastic solids. *J. Reine und Angewandte Mathematik*, 92: 156–171, 1882.

- [10] C Cattaneo. Sul contatto di due corpi elastici: Distribuzion locale degli sforzi. *Reconditi dell Accademia nazionale dei Lincei*, 27:342–348, 434–436, 474–478, 1938.
- [11] R D. Mindlin and H Deresciewicz. Elastic spheres in contact under varying oblique forces. *Journal of Applied Mechanics*, 75:327–344, 1953.
- [12] H Poritsky. Stresses and deflections of cylindrical bodies in contact with application to contact of gears and of locomotive wheels. *Journal of Applied Mechanics*, 72:191–201, 1950.
- [13] K Endo and H Goto. Initiation and propagation of fretting fatigue cracks. *Wear*, 21: 947–956, 1976.
- [14] P R. Edwards. The application of fracture mechanics to predicting fretting fatigue. In R B. Waterhouse, editor, *Fretting Fatigue*, pages 67–99. Elsevier Applied Science Publishers, London, 1981.
- [15] D P. Rooke and D A. Jones. Stress intensity factors in fretting fatigue. *Journal of strain analysis*, 14(1):1–6, 1979.
- [16] D A. Hills and D Nowell. *Mechanics of Fretting Fatigue*. Kluwer Academic Publishers, Dordrecht, The Netherlands, 1994.
- [17] L J. Fellows, D Nowell, and D A. Hills. Analysis of crack initiation and propagation in fretting fatigue: The effective flaw size methodology. *Fatigue and fracture of engineering materials and structures*, 20(1):61–70, 1997.
- [18] D Godfrey. Investigation of fretting corrosion by microscopic observation. Technical note 2039, NACA, 1950.
- [19] B Bethune and R B. Waterhouse. Adhesion of metal surfaces under fretting conditions like metals in contact. *Wear*, pages 289–296, 1968.
- [20] R B. Waterhouse. Influence on the local temperature increases on the fretting corrosion of mild steel. *Journal of the iron and steel institute*, 197:301–305, 1961.

- [21] M H. Attia and N S. D'Silva. Effect of the mode of motion and process parameters on the prediction of temperature rise in fretting wear. *Wear*, 106:206-224, 1985.
- [22] M H. Attia and P L. Ko. On the thermal aspects of fretting wear-temperature measurements in the subsurface layer. *Wear*, 111:363-376, 1986.
- [23] O Vingsbo and D Soderberg. On fretting maps. *Wear*, 126:131-47, 1988.
- [24] D A. Hills, D Nowell, and A Sackfield. In *Interface Dynamics: Proceedings of the 14th Leeds-Lyon Symposium on Tribology Held at the Institut National Des Sciences Appliquees, Lyon, France*. Elsevier, 1987.
- [25] D A. Hills and D Nowell. The development of a fretting fatigue experiment with well-defined characteristics. In *Standardization of Fretting Fatigue: Test Methods and Equipment ASTM STP 1159*, pages 69-84, Philadelphia, PA, 1992. Am Soc for Test and Materials.
- [26] D A. Hills and L J. Fellows. Some observations on contact problems involving fretting in the presence of wear. *Wear*, 231:319-324, 1999.
- [27] C Ruiz, P H B. Boddington, and K C. Chen. An investigation of fatigue and fretting in a dovetail joint. *Experimental mechanics*, pages 208-217, September 1984.
- [28] C. Ruiz and K C. Chen. Life assessment of dovetail joints between blades and discs in aero-engines. In *Proceedings of the International Conference on Fatigue*, Sheffield, UK, 1986.
- [29] M Ciavarella. The generalized Cattaneo partial slip plane contact problem. Part I theory. Part II examples. *International Journal of Solids and Structures*, 35:2349-2378, 1998.
- [30] M Ciavarella, D A. Hills, and G Monno. The influence of rounded edges on indentation by a flat punch. *Proceedings of the Institute of Mechanical Engineers*, 212C:319-328, 1998.
- [31] M Ciavarella, G. Demelio, and D A. Hills. *The Use of Almost Complete Contacts for Fretting Fatigue Tests*, volume 29 of *ASTM STP 1332*, pages 696-709. American Society of Testing and Materials, West Conshohocken, PA, 1999.

- [32] M P. Szolwinski and T N. Farris. Linking riveting process parameters to the fatigue performance of riveting aircraft structures. *Journal of aircraft*, 37:130–137, 2000.
- [33] G Harish, M P. Szolwinski, T N. Farris, and T Sakagami. Evaluation of fretting stresses through full-field temperature measurements. In D W. Hoepfner, V Chandrasekaran, and C B. Elliott III, editors, *Fretting Fatigue: Current Technology and Practices*, ASTM STP 1367, pages 423–435, West Conshohocken, PA, 2000. ASTM.
- [34] P A. McVeigh, G Harish, T N. Farris, and M P. Szolwinski. Modeling contact conditions in nominally-flat contacts for application to fretting fatigue of turbine engine components. *International Journal of Fatigue*, 21:S157–165, 1999.
- [35] P R. Birch. *A Study of Fretting Fatigue in Aircraft Components*. PhD thesis, Massachusetts Institute of Technology, 1998.
- [36] B U. Wittkowsky, P R. Birch, J Dominguez, and S Suresh. An apparatus for quantitative fretting fatigue testing. *Fatigue and Fracture of Engineering Materials and Structures*, 22(4):307, 1999.
- [37] T A. Venkatesh, B P. Conner, C S. Lee, A E. Giannakopoulos, and T C. Lindley. An experimental investigation of fretting fatigue in Ti-6Al-4V: The role of contact conditions and microstructure. *Metallurgical Transactions*, 32A:1131–1146, 2001.
- [38] M P. Szolwinski and T N. Farris. Observation, analysis and prediction of fretting fatigue in 2024-t351 aluminum alloy. *Wear*, 221:24–36, 1998.
- [39] D W. Hoepfner. Review of fretting fatigue component life estimation/prediction: Past, present and future. In *Proceedings of the International Symposium on Fretting Fatigue*, Nagaoka, Japan, 2001.
- [40] A E. Giannakopoulos, T C. Lindley, and S Suresh. Aspects of equivalence between contact mechanics and fracture mechanics: Theoretical connections and a life-prediction methodology for fretting-fatigue. *Acta materialia*, 46(9):2955–2968, 1998.
- [41] A E. Giannakopoulos, T A. Venkatesh, T C. Lindley, and S Suresh. The role of adhesion in contact fatigue. *Acta materialia*, 47(18):4653–4664, 1999.



- [42] A E. Giannakopoulos, T C. Lindley, S Suresh, and C Chenut. Similiarities of stress concentrations in contact at round punches and fatigue in notches: Implications to fretting fatigue crack initiation. *Fracture and fatigue of engineering materials and structures*, 23: 562–571, 2000.
- [43] L Chambon. A unified fracture mechanics approach to fretting fatigue crack growth. Master's thesis, Massachusetts Institute of Technology, 2000.
- [44] G W. Kirkpatrick. Fretting fatigue analysis and palliatives. Master's thesis, Massachusetts Institute of Technology, 1999.
- [45] K Iyer, M Xue, P C Bastias, C A Rubin, and G T Hahn. Analysis of fretting and fretting corrosion in airframe riveted connections. In *Tribology for Aerospace Systems*, pages 6–12. AGARD, 1996.
- [46] D Thomson. The national turbine high cycle fatigue program. In CD ROM Proceedings, editor, *Proceedings of the 3rd National Turbine High Cycle Fatigue Conference*, San Antonio, TX, 1998. Universal Technology Corp.
- [47] N S. Xi, P D. Zhong, H Q. Huang, H Yan, and C H. Tao. Failure investigation of blade and disk in first stage compressor. *Engineering failure analysis*, 7:385–392, 2000.
- [48] Stanley W. Kandebo. Rolls-royce resolvesTrent 800 cracks. *Aviation Week Space Technology*, 154(23):54, June 2001.
- [49] Magellan Aerospace Corporation. Developing of surface modification to reduce fretting and fretting fatigue in a space environment. Technical report, Canadian Space Agency, 2001.
- [50] Y N. Drozdov. Tribological safety of technical systems in space. *Vestnik Mashinostroeniya*, 7:11–13, July 1999.
- [51] K Miyoshi. *Solid Lubrication Fundamentals and Applications*. Marcel Dekker, Inc., New York, 2001.
- [52] J Dundurs. Discussion of edge bonded dissimilar orthogonal elastic wedges under normal and shear loading. *Journal of applied mechanics*, 36:650–652, 1969.

- [53] N I. Muskhelishvili. *Some Basic Problems of the Mathematical Theory of Elasticity*. Noordhoff, Groningen, 1953.
- [54] W D. Collins. On the solution of some axisymmetric boundary value problems by means of integral equations, II: Further problems for a circular disc and a spherical cap. *Mathematika*, 6:120–133, 1959.
- [55] D A. Hills and D Nowell. Crack initiation criteria in fretting fatigue. *Wear*, 136(1): 329–343, 1989.
- [56] B P. Conner. Mechanical and microstructural effects on fretting fatigue of Ti-6Al-4V. Master’s thesis, Massachusetts Institute of Technology, 2000.
- [57] J O. Peters, O Roder, B L. Boyce, A W. Thompson, and R O. Ritchie. Role of foreign-object damage on thresholds for high cycle fatigue in Ti-6Al-4V. *Metallurgical and Materials Transactions A*, 31A:1571–1583, 2000.
- [58] Richard S. Bellows, Ken R. Bain, and Jerry W. Sheldon. Effect of step testing and notches on the endurance limit of Ti-6Al-4V. *Mechanical behavior of advanced materials ASME*, 84:27–32, 1998.
- [59] W D. Milestone. Fretting and fretting fatigue in metal to metal contacts. In *Proceedings AIAA Structural Dynamics and Materials Conference*, page 96, Denver, 1970.
- [60] C Ruiz and D Nowell. Designing against fretting fatigue in aeroengines. In A Martin-Meizoso Adn J M. Martinez-Esanola M Fuentes, M Elices, editor, *Fracture Mechanics: Applications and Challenges. ECF 13.ESIS Publication 26*, pages 73–95, New York, 2000. ESIS, Elsevier.
- [61] D C. Maxwell and T Nicholas. A rapid method for generation of a Haigh diagram for high cycle fatigue. In T L. Panontin and S D. Sheppard, editors, *Fatigue and Fracture Mechanics, ASTM STP 1332*, volume 29, pages 626–641. American Society for Testing and Materials, West Conshohocken, Pennsylvania, 1999.
- [62] A L. Hutson and T Nicholas. Fretting fatigue behavior of Ti-6Al-4V against Ti-6Al-4V under flat-on-flat contact with blending radii. In D W. Hoepfner, V Chandrasekaran,

- and C B. Elliot, editors, *Fretting Fatigue: Current Technology and Practices, ASTM STP 1367*, pages 308–321. American Society for Testing and Materials, West Conshohocken, Pennsylvania, 2000.
- [63] D A. Johnson. Automated deformation mapping in fatigue and fracture. In A A. Braun, P C. McKeighan, A M. Nicolson, and R D. Lohr, editors, *Applications of Automation Technology in Fatigue and Fracture Testing and Analysis: Fourth Volume ASTM STP 1411*, West Conshohocken, PA, 2002. American Society for Testing and Materials.
  - [64] Hibbitt, Karlsson Sorensen, Inc. *ABAQUS/Standard User's Manual*, volume iii edition, 2001.
  - [65] S Fouvry, P Kapsa, and L Vincent. Fretting-wear and fretting-fatigue: Relation through a mapping concept. In D W Hoepfner, V Chandrasekaran, and III C B Elliot, editors, *Fretting Fatigue: Current Technology and Practices, ASTM STP 1367*, pages 49–64, West Conshohocken, PA, 2000. Am. Soc. for Testing and Materials.
  - [66] A L. Hutson, T Nicholas, S E. Olson, and N E. Ashbaugh. Effect of sample thickness on local contact behavior in a flat-on-flat fretting fatigue apparatus. *International Journal of Fatigue*, 23(S1):445–453, 2001.
  - [67] R A. Antoniou and T C. Radtke. Mechanisms of fretting fatigue in titanium alloys. *Materials Science Engineering A*, pages 229–240, 1997.
  - [68] R W. Neu, D L. McDowell, C H. Goh, and J M. Wallace. Crystallographic cyclic plasticity approaches applied to attachment fatigue problems. Technical Report Final Technical Report, Air Force Contract F49620-99-C-0007, Georgia Institute of Technology, 2000.
  - [69] J A. Pape and R W. Neu. Fretting fatigue damage accumulation in PH-13-8Mo stainless steel. *International Journal of Fatigue*, 23:S437–S444, 2001.
  - [70] E Sauger, S Fouvry, L Ponsonnet, Ph Kapsa, J M Martin, and L Vincent. Tribologically transformed structure in fretting. *Wear*, 245:39–52, 2000.
  - [71] G M. Hamilton. Explicit equations for the stresses underneath a sliding spherical contact. *Proceedings of the Institute of Mechanical Engineers*, 197C:53–59, 1983.

- [72] A R S Pointer, A D Hearle, and K L Johnson. Application of the kinematical shakedown theorem to rolling and sliding point contacts. *Journal of the Mechanics and Physics of Solids*, 33:339–362.
- [73] T C. Lindley. Fretting fatigue in engineering alloys. *International Journal of Fatigue*, 19: S39–S49, 1997.
- [74] F S Sproles and D J Duquette. The mechanism of material removal in fretting. *Wear*, 49:339–52, 1978.
- [75] M C. Dubourg and B Villechaise. Analysis of multiple fatigue cracks-part i theory. *Journal of Tribology*, 114(3):455–461, 1992.
- [76] M Godet M C. Dubourg and B Villechaise. Analysis of multiple fatigue cracks-part 2 results. *Journal of Tribology*, 114(3):462–468, 1992.
- [77] D A. Hills, D. Nowell, and A. Sackfield. *Mechanics of Elastic Contact*. Butterworth-Heinemann, Oxford, 1993.
- [78] A I. Nadai. *Theory of Flow and Fracture of Solids*. McGraw-Hill, New York, 1963.
- [79] M Sadowski. *Z Angew Math Mech*, 8:107, 1928.
- [80] M L. Williams. On the stress distribution at the base of a stationary crack. *Journal of Applied Mechanics*, 24:109–114, 1957.
- [81] J S. McFarlane and D Tabor. *Proc R Soc Lond*, A202:244, 1950.
- [82] B Cottrell and J R. Rice. Slightly curved or kinked cracks. *International journal of fracture*, 16:155–169, 1980.
- [83] M. Isida. *Transactions of the Japan Society of Mechanical Engineers A*, 45:306, 1979.
- [84] P C. Paris, M P. Gomez, and W P. Anderson. A rational analytic theory of fatigue. *The Trend in Engineering*, 13:9–14, 1961.
- [85] M Creager and P C Paris. Elastic field equations for blunt cracks with reference to stress corrosion cracking. *International journal of fracture mechanics*, 3:247–252, 1967.

- [86] J M. Barsom and R C. McNichol. Effect of stress concentration on fatigue crack initiation in HY-130 steel. In *Fracture Toughness and Slow-Stable Cracking ASTM STP 559*, pages 183–204. American Society for Testing and Materials, 1974.
- [87] J P. Campbell and R O. Ritchie. Mixed-mode fatigue-crack growth thresholds in Ti-6Al-4V at high frequency. *Scripta materialia*, 41(10):1067–1071, 1999.
- [88] I M. Hutchings. *Tribology: Friction and Wear of Engineering Materials*. CRC Press, Boca Raton, Florida, 1992.
- [89] E Rabinowicz. In M B. Peterson and W O. Winer, editors, *Wear Control Handbook*, pages 475–506. ASME, 1980.
- [90] A K. Koul, L Xue, W Wallace, M Bibby, S Chakravarty, R G. Andrews, and P C Patnaik. An investigation on surface treatments for improving the fretting fatigue resistance of titanium alloys. In *82nd Meeting of the AGARD Structures and Materials Panel*, Sesimbra, Portugal, 1996.
- [91] T C. Chivers and S C. Gordelier. Fretting fatigue and contact conditions: A rational explanation of palliative behaviour. *Proceedings of the Institute of Mechanical Engineers*, 198-199C:325–337, 1984-85.
- [92] S Suresh. Graded materials for resistance to contact deformation and damage. *Science*, 292:2447–2451, 2001.
- [93] A Stodola. *Steam and Gas Turbines*. McGraw-Hill, New York, 1927.
- [94] Praxair Surface Technologies. Documentation on the mechanical properties of aluminum bronze coating, 1999.
- [95] K J. Van Vliet and A Gouldstone. Mechanical properties of thin films quantified via instrumented indentation. *Surface Engineering*, 17:140–145, 2001.
- [96] Y. Sugimura, P G. Lim, C. F. Shih, and S. Suresh. Fracture normal to a bimaterial interface: Effects of plasticity on crack-tip shielding and amplification. *Acta Metallurgica et Materialia*, 43:1157–1169, 1995.

- [97] A S. Kim, S. Suresh, and C F. Shih. Fracture normal to interfaces with homogeneous and graded compositions. *International Journal of Solids and Structures*, 34:3415–3432, 1997.
- [98] J W. Hutchinson and Z Suo. Mixed mode cracking in layered materials. *Advances in Applied Mechanics*, 29:63–191, 1992.
- [99] M Dao, N Chollacoop, K J. Van Vliet, T A. Venkatesh, and S Suresh. Computational modeling of the forward and reverse problems in instrumented sharp indentation. *Acta materialia*, 49:3899–3918, 2001.
- [100] M J. Shepard, P R. Smith, P S. Prevéy, and A H. Clauer. Thermal stability of LSP induced residual stresses in Ti-6Al-2Sn-4Zr-2Mo and IN100 simulated airfoils. In *Proceedings of the 6th National Turbine High Cycle Fatigue Conference*, Jacksonville, Florida, 2001.
- [101] P S. Prevéy. *Advances in X-Ray Analysis*, 29:103–111, 1986.
- [102] P S. Prevéy. Method of determining the elastic properties of alloys in selected crystallographic directions for x-ray diffraction residual stress measurement. *Advances in X-Ray Analysis*, 20:345–354, 1977.
- [103] D P. Koistinen and R E. Marburger. *Trans ASM*, 51:537–550, 1959.
- [104] T C. Lindley and K J. Nix. Fretting fatigue in the power generation industry. In H A. Attia and R B. Waterhouse, editors, *Standardization of Fretting Fatigue Test Methods and Equipment*, pages 153–169. American Society for Testing and Materials, Philadelphia, 1992.
- [105] R B. Waterhouse. Residual stresses and fretting-crack initiation and propagation. In *Advances in Surface Treatment - Technology, Applications, Effects*, chapter Vol 4 Residual Stresses, page 517. Pergamon, Oxford, 1987.
- [106] H Tada, P C. Paris, and G R. Irwin. *Stress Analysis of Cracks Handbook*. Del Research Corporation, Hellertown, PA, 1973.
- [107] C H. Goh, J M. Wallace, R W. Neu, and D L. McDowell. Polycrystal plasticity simulations of fretting fatigue. *International Journal of Fatigue*, 23:S423–S435, 2001.

- [108] S Suresh and A Mortensen. *Fundamentals of Functionally Graded Materials : Processing and Thermomechanical Behaviour of Graded Metals and Metal-Ceramic Composites*. IOM Communications Ltd, London, 1998.
- [109] Serkan Dag and Fazil Erdogan. A surface crack in a graded medium loaded by a sliding rigid stamp. *Engineering Fracture Mechanics*, 69:1729–1751, 2002.
- [110] M R. Begley and J W. Hutchinson. Plasticity in fretting of coated substrates. *Engineering fracture mechanics*, 62:145–164, 1999.